

Effect of 475°C Embrittlement on the Fatigue Behaviour of a Duplex Stainless Steel

Dissertation

zur Erlangung des akademischen Grades

Doktor-Ingenieur

vorgelegt von

Jitendra Kumar Sahu, B.E., M.Tech.

eingereicht dem Fachbereich

Maschinenbau

der Universität Siegen

Referent: Prof. Dr.-Ing. habil. Hans-Jürgen Christ

Korreferent: Prof. Dr.-Ing. habil. Ulrich Krupp

October 2008

Kurzdarstellung

Die Kurzzeitfestigkeit von Duplexstahl wurde im lösungsgeglühten Wärmebehandlungszustand und unter Versprödungsbedingungen (100 Stunden Glühen bei 475°C) durch mechanische Untersuchungen, Raster- und Transmissionselektronenmikroskopie untersucht. Dabei ist das Rissinitiierungsverhalten im versprödeten Zustand durch kraftgeregelte Ermüdungstests charakterisiert worden, wobei die Rissinitiierungsorte identifiziert und mit aus EBSD-OIM-Scans erhaltenen Kristallparametern in Bezug gesetzt wurden. Das Glühen bei 475°C führt zur Ausscheidung von α' in der ferritischen Phase. Die Kerbschlagenergie fiel von 260 Joule im Ausgangszustand auf 8 Joule im versprödeten Zustand ab. Dieser Rückgang im versprödeten Zustand wird dadurch verursacht, dass die verformungsinduzierte Zwillingbildung der ferritischen Phase unterbunden wird, was durch entsprechende TEM-Untersuchungen belegt wurde. Die Experimente zur Kurzzeitfestigkeit, die bei $\Delta\varepsilon/2 = 4,0 \times 10^{-3}$, $6,0 \times 10^{-3}$, $8,0 \times 10^{-3}$ und $1,0 \times 10^{-2}$ durchgeführt wurden, zeigen, dass die zyklischen Verformungskurven im lösungsgeglühten Zustand drei klar voneinander abgegrenzte Bereiche aufweisen: (i) zyklische Verfestigung, (ii) zyklische Entfestigung, und (iii) zyklische Sättigung; im versprödeten Zustand lassen sich zwei voneinander abgrenzbare Bereiche identifizieren: (i) zyklische Verfestigung und (ii) zyklische Entfestigung bis zum Versagen für alle verwendeten Belastungsamplituden. Im Vergleich zum lösungsgeglühten Zustand kann eine Änderung der Steigung bei der zyklischen Spannungs-Dehnungs-Kurve im versprödeten Zustand festgestellt werden. Im Bereich der verwendeten Dehnungsamplituden ist die Ermüdungsfestigkeit im versprödeten Zustand bei einer geringen plastischen Dehnungsamplitude höher, bei einer mittleren plastischen Dehnungsamplitude ähnlich und bei einer höheren plastischen Dehnungsamplitude niedriger im Vergleich mit dem lösungsgeglühten Zustand. Die allmähliche Abnahme der Ermüdungsfestigkeit mit Zunahme der plastischen Dehnungsamplitude im versprödeten Zustand wird auf die schnelle zyklische Entfestigung zurückgeführt, die durch das Auflösen der α' -Ausscheidungen verursacht wird. Aus den Rissinitiierungsuntersuchungen, die bei $\Delta\sigma/2 = 400$ MPa und 500 MPa durchgeführt wurden, kann geschlossen werden, dass die Risse an Gleitspuren initiieren, die auf Ebenen vom Typ $\{111\}$ im Austenit entstehen. Bei $\Delta\sigma/2 = 500$ MPa initiierten mehr Risse an $\Sigma 3$ CSL-Korngrenzen im versprödeten Zustand. Der Hauptwiderstand gegenüber der Rissausbreitung kann den $\alpha\gamma$ Phasengrenzen zugeschrieben werden.

Acknowledgement

I express my deep sense of gratitude to my thesis supervisor Prof. H. -J. Christ for his support and guidance. It was a rare honour and educative experience working with him. I also express my gratefulness to Prof. U. Krupp for readily agreeing to be a co-referee for my thesis. I extend my sincere gratitude to Prof. X. Jiang and Prof. R. Lohe for readily accepting to be my thesis examiners.

I am grateful to Prof. S. P. Mehrotra, Director NML for allowing me to submit the thesis. His support during the progress of the work is gratefully acknowledged. Special thanks are due to my HOD at NML Dr. R. N. Ghosh. In fact it is for his encouragement and moral support when personal situations in life had made me crippled, I am able to submit the thesis today.

The help extended by all of my colleagues at LMW, IFWT Siegen is greatly appreciated. My special thanks are due to Dr.-Ing. O. Düber and Dipl.-Ing. H. Knobbe for innumerable discussions during the progress of the work. Apart from these discussions, since I conducted experiments both at LMW Siegen and at NML Jamshedpur it involved a lot of logistics such as transferring the specimen, heat treatment etc. and these two friends have always extended their hands of co-operation without any hesitation. The friendly advice rendered by Dr.-Ing. G. Lohse and Dr.-Ing. W. Floer has always been helpful. The congenial atmosphere provided by Dipl.-Ing. P. Schmidt and Dipl.-Ing. T. K. Heckel during the thesis writing will be cherished forever. Thanks are also due to Dipl.-Ing. C. Stöcker for his friendly assistance during the final experiments that I conducted at IFWT Siegen. The help rendered by Dr.-Ing. V. Srikanth during the last part of my stay at Siegen is gratefully acknowledged. I also thank Frau Mockenhaupt for her help in the administrative work.

The help extended by all my colleagues at NML is gratefully acknowledged. The discussion with Dr. S. R. Singh, Dr. S. Tarfader, Dr. S. Sivaprasad, Dr. B. Ravikumar and Dr. N. Parida were very fruitful and appreciated. A special word of thanks is due Dr. A. K. Ray and Dr. J. Swaminathan for their continuous encouragement during the work. Friendly assistance provided by Dr. S. Das, Dr. N. Narasaiah is gratefully acknowledged. Thanks are also due to Dr. N. G. Goswami Head Library for his kind gesture in accepting some translation work. My

special thanks to Dr. B. Nayak a personal friend who has never said no to me when I resort to him during time of crisis. In this regard I also wish to thank Ms. Emila Panda for her encouragement during the progress of the work. I also take this opportunity to thank Dr. K. Bhanu Sankara Rao, Dr. M. Valsan and Mr. A. Nagesha of IGCAR Kalpakkam for their support and encouragement during the progress of this work.

I acknowledge the financial support provided by DAAD for my initial stay at Siegen. In this regard I also wish to thank Prof. Christ for providing financial support during my final part of stay at Siegen.

This work would not have been possible without the continuous support and encouragement of my parents, sister Julie, wife Archana in all aspects. I express my profound gratitude to them. The innocence of our kids, son Abhishek and niece Nikita has always been a source of immense strength.

Finally, I would like to dedicate this work all together to my father Shri Ganeswar Sahu and mother late Smt. Urmila Sahu.

October 2008

Jitendra Kumar Sahu

Contents

Abstract	i
List of symbols and abbreviations	ii
Symbols.....	ii
Abbreviations.....	iv
Chapter 1 Introduction.....	1
Chapter 2 Literature review	5
2.1 Fatigue behaviour of metallic materials and alloys	5
2.1.1 Cyclic deformation mechanisms.....	6
2.1.2 Crack initiation and growth	18
2.1.3 Total life approach	24
2.1.4 Defect tolerant approach	32
2.2 Duplex stainless steel and 475°C embrittlement.....	35
2.2.1 Duplex stainless steel.....	35
2.2.2 475°C embrittlement	36
Chapter 3 Experimental techniques.....	40
3.1 Material characterization	40
3.1.1 Heat treatment.....	40
3.1.2 Electron microscopy	42
3.2 Mechanical characterization	44
3.2.1 Low cycle fatigue.....	44
3.2.2 Fatigue crack initiation	45
Chapter 4 Results and discussion	48
4.1 Microstructural characterization	48
4.1.1 Optical microscopy	48
4.1.2 Scanning electron microscopy	50
4.1.3 Transmission electron microscopy	54
4.2 Effect of aging treatment on tensile and impact behaviour	56
4.2.1 Tensile behaviour.....	56
4.2.2 Impact behaviour	61
4.3 Effect of aging treatment on the low cycle fatigue behaviour	65

4.3.1	Cyclic hardening/softening behaviour	65
4.3.2	Cyclic stress-strain curve	68
4.3.3	Cyclic life.....	72
4.3.4	Electron microscopic examination.....	74
4.4	Fatigue crack initiation in DSS embrittled at 475°C.....	81
Chapter 5 Discussion.....		93
5.1	475°C embrittlement of DSS	93
5.2	Low cycle fatigue behaviour of DSS	97
5.2.1	Cyclic hardening/softening behaviour	98
5.2.2	Cyclic stress-strain curve	102
5.2.3	Cyclic life.....	103
5.3	Fatigue crack initiation behaviour in DSS embrittled at 475°C.....	104
Chapter 6 Conclusions and future aspects		107
References		111

Abstract

The low cycle fatigue behaviour of a duplex stainless steel was studied in standard heat treated and embrittled (by aging at 475°C for 100 hours) condition by mechanical testing, scanning and transmission electron microscopy. The fatigue crack initiation behaviour was studied in the embrittled condition by interrupting stress-controlled fatigue tests, identifying the crack initiation sites and relating them to the crystallographic parameters obtained from EBSD-OIM scans. The aging treatment at 475°C resulted in the precipitation of α' in the ferritic phase. Impact energy drops from 260 Joules in the annealed condition to 8 Joules in the aged condition. The drop in impact energy was caused by the inability of the ferritic phase to form deformation twins in the embrittled condition, which was confirmed by TEM examination. From the low cycle fatigue experiments conducted at $\Delta\varepsilon/2 = 4.0 \times 10^{-3}$, 6.0×10^{-3} , 8.0×10^{-3} and 1.0×10^{-2} , it was established that the deformation curves in the annealed condition has three discernible stages: (i) cyclic hardening, (ii) cyclic softening and (iii) cyclic saturation and in the aged condition has two discernible stages: (i) cyclic hardening, and (ii) cyclic softening till final failure for all values of strain amplitude. A change in slope is observed in the cyclic stress-strain curve in the aged condition as compared to the standard heat treated condition. In the range of strain amplitude employed, in the aged condition, fatigue life is longer at lower plastic strain amplitude, decreases and becomes similar at intermediate plastic strain amplitude and becomes shorter at higher plastic strain amplitude in comparison to the standard heat treated condition. The gradual decrease in fatigue life with increase in plastic strain amplitude in the aged condition was attributed to the rapid cyclic softening caused by disappearance of the α' precipitates. From the fatigue crack initiation studies conducted at $\Delta\sigma/2 = 400$ MPa and 500 MPa, it was established that the crack initiation sites are the slip markings corresponding to $\{111\}$ plane traces in the austenitic grains at $\Delta\sigma/2 = 400$ MPa and more cracks were observed to initiate at $\Sigma 3$ CSL boundaries in the austenitic grain at $\Delta\sigma/2 = 500$ MPa in the aged condition. The major resistance to crack growth came from the $\alpha\gamma$ phase boundary.

List of symbols and abbreviations

Symbols

Latin symbols

A	[m ²]	Area
a	[nm]	Crack length
b	[Å]	Burgers vector
b	[-]	Fatigue strength exponent
C	[mm/cycle]	Paris constant
c	[-]	Fatigue ductility exponent
D	[mm]	Maximum diameter at the notch
d	[mm]	Minimum diameter at the notch
E	[GPa]	Young's modulus
F	[N]	Force
G	[GPa]	Shear modulus
K'	[MPa]	Cyclic strength coefficient
ΔK	[N/m ^{3/2}]	Stress intensity factor range
ΔK_{th}	[N/m ^{3/2}]	Long fatigue crack threshold value of stress intensity factor range
L_d	[μ m]	Length of the dipole loop
m	[-]	Schmid factor
m	[-]	Paris constant
N	[-]	Number of cycles
N_f	[-]	Number of cycles to failure
n	[-]	Strain hardening exponent
n'	[-]	Cyclic strain hardening exponent
R	[-]	Load ratio
R	[μ m]	Separation distance between dislocations
S	[MPa]	Stress amplitude
S_d	[μ m]	Slip plane spacing
T	[°C]	Temperature
U_f	[Joule]	Energy of formation of atomic defects
Y	[-]	Dimensionless constant
y_s	[μ m]	Annihilation distance between screw dislocation
y_e	[μ m]	Annihilation distance between edge dislocation
y_m	[μ m]	Annihilation distance between mixed dislocation
da/dN	[mm/cycle]	Crack growth rate

Greek symbols

ε	[-]	Strain
ε_f	[-]	Fracture strain
ε_f'	[-]	Fatigue ductility coefficient

$\Delta\varepsilon/2$	[-]	Total strain amplitude
$\Delta\varepsilon_{el}/2$	[-]	Elastic strain amplitude
$\Delta\varepsilon_{pl}/2$	[-]	Plastic strain amplitude
ϕ	[°]	Angle between slip plane normal and tensile axis
$\phi_1 \ \phi \ \phi_2$	[°]	Bunge's Euler angles
κ	[Å]	Sense vector of the dislocation
λ	[μm]	Inter obstacle spacing
λ	[°]	Angle between slip direction and tensile axis
λ_d	[μm]	Interdislocation separation distance
ν	[-]	Poisson's ratio
ρ	[/ mm^2]	Dislocation density
σ	[MPa]	Stress
σ_e	[MPa]	Endurance limit
σ_f	[MPa]	True fracture strength
σ_f'	[MPa]	Fatigue strength coefficient
σ_o	[MPa]	Orowan stress
σ_p	[MPa]	Pinning stress for dislocation
σ_s	[MPa]	Saturation stress amplitude
$\sigma_{ys} (0.2\%)$	[MPa]	0.2% offset yield strength
σ_{uts}	[MPa]	Ultimate tensile strength
$\Delta\sigma$	[MPa]	Stress range
σ_{mean}	[MPa]	Mean stress
$\Delta\sigma/2$	[MPa]	Stress amplitude
$(\Delta\sigma/2)_{max}$	[MPa]	Maximum stress amplitude
$(\Delta\sigma/2)_{1st \text{ cycle}}$	[MPa]	Maximum stress amplitude during 1 st cycle
τ_{bow}	[MPa]	Dislocation bowing stress
τ_g	[MPa]	Shear stress required for dislocation glide
τ_p	[MPa]	Passing shear stress for a dipole
v_g	[mm/sec]	Dislocation glide velocity
ψ	[°]	Angle between the Burgers vector and sense vector of the dislocation

Abbreviations

ACOM	Automated crystal orientation mapping
AFM	Atomic force microscope
BCC	Body center cubic
BF	Bright field
CRSS	Critical resolved shear stress
CSL	Coincident site lattice
CSS	Cyclic stress-strain
CSSC	Cyclic stress-strain curve
DSS	Duplex stainless steel
EBSD	Electron back scattered diffraction
EGM	Essmann Gösele Mughrabi
FCC	Face center cubic
FEG	Field-emission gun
GB	Grain boundary
GBCD	Grain boundary character distribution
HAB	High angle boundary
HAZ	Heat affected zone
HCF	High cycle fatigue
HCP	Hexagonal close packed
IST	Incremental step test
KS	Kurdjumov-Sachs
LAB	Low angle boundary
LCF	Low cycle fatigue
MAB	Medium angle boundary
MST	Multiple step test
OIM	Orientation imaging microscope
PSB	Persistent slip band
SE	Secondary electron
SEM	Scanning electron microscope
SST	Single step test
TEM	Transmission electron microscope

Chapter 1 Introduction

The fatigue characterization of metallic materials and alloys is historically noted to have started way back in 1829. Albert, a German mining engineer conducted repeated load proof tests on mine hoist chain made of iron [1]. However, the most noted fatigue characterization, which still has a very wide acceptance in the modern fatigue design, is the systematic investigation of fatigue failures in railroad axles of the German railway industry conducted by Wöhler in 1860 [2]. He observed lower strength of the steel axles during cyclic loading as compared to monotonic loading. His work led to the concept of fatigue characterization using stress amplitude-life ($S-N$) curves and endurance limit. Since then different design aspects have emerged for characterizing fatigue behaviour of load bearing metallic materials and alloys. The fracture mechanics concept was introduced to fatigue characterization in 1960 [3]. Paris and Erdogan are the first to suggest that fatigue crack propagation per stress cycle (da / dN) can be related to the range of stress intensity factor (ΔK) [4]. This approach to fatigue design can tolerate an existing defect in a component as it is equipped to calculate the time for the growth of such existing defect to the critical size prior to the onset of catastrophic failure under the prevailing cyclic loading conditions. This is being known as the defect tolerant approach to fatigue design.

Parallel to the evolution of concepts relating to mechanics of fatigue behaviour there was continuous effort by material scientists to understand fatigue mechanisms. The first reported work on relating the fatigue behaviour to the microstructure came from Ewing and Rosenhein in 1900 who reported cracking along the plane traces of active slip planes on the surface in fatigued iron [5]. With the invention of electron microscopes the most fundamental mechanisms specific to cyclic loading were established. Owing to the microstructural complexities in polycrystals, single crystals of pure copper [6-8], silver [9], nickel [9-10] were used for identifying the basic fatigue mechanisms and establishing quantitative relationship with cyclic deformation behaviour. Nevertheless, studies on fatigue mechanisms assumed significance in polycrystalline materials, as these materials are continuously evolving to newer grades to realize improved properties in engineering applications. Minor adjustments in alloy composition are observed to significantly change the fatigue behaviour

of these materials. Alloying [11-12] and varying microstructural parameters such as grain size [13-14], precipitation condition [15-17] etc modify the fatigue mechanisms of polycrystalline materials.

In recent years, two-phase structural materials are finding increasing engineering applications. The advantage of both the phases is realized in improving the properties. Duplex stainless steel (DSS) is one such attractive two-phase material being increasingly used in structural applications in nuclear, oil, power and petrochemical industries [18-21]. The complexities in the cyclic deformation mechanisms increase for two-phase materials [22-25]. There are several factors such as orientation relationship between the phases, partitioning of alloying elements to different phases, texture, and topography that can affect the fatigue behaviour in two-phase materials. The complexities deepen further when one of the phases undergoes aging embrittlement affecting the fatigue behaviour of the material. The change in the fatigue behaviour is a symptom. However, a proper diagnosis of the problem is done only when the root cause is identified. Investigation of cyclic deformation mechanism facilitates in identifying the role of the embrittling phase in altering the fatigue behaviour at the level of microstructure and substructure. DSS undergoes such kind of embrittlement in the temperature range of 280-500°C limiting its application to temperatures below 280°C. The iron-chromium binary system has a miscibility gap in this temperature range and the ferritic phase decomposes into an iron-rich bcc phase (α) and a chromium-rich bcc phase (α') [26-30]. The rate of embrittlement is highest at 475°C and is referred to as 475°C embrittlement. The 475°C embrittlement was at first observed in iron-chromium binary alloy system [26-29]. DSS also gets embrittled as it contains the ferritic phase.

The concept of alloy design stems from adjusting the existing composition to improve properties and eliminate undesirable phase transformations during applications [31-32]. In order to eliminate such undesirable phase transformations it is essential to establish their effect on properties at the level of microstructure and substructure [33]. The continuous evolution of DSS to better grades combined with increasing demand for obtaining better fatigue properties has provided fresh impetus for fatigue research on this material [34-37]. The factors those are known to affect the fatigue behaviour of DSS are: (a) alloy composition [38-42], (b) volume fraction of ferrite [43-44], and (c) processing route (cast and wrought)

[44-45]. Interestingly some of these factors also have pronounced influence on the change in fatigue behaviour resulting from aging treatment at 475°C. Therefore, the change in cyclic deformation mechanisms as a result of 475°C embrittlement has always to be discussed in conjunction with the above-mentioned factors. This is the genesis behind identifying fatigue characterization with an emphasis on cyclic deformation mechanisms of DSS in a severe and deleterious heat treatment condition as the area of present research work. The broad objectives of the research programme are outlined below:

- The initial investigations started with the study on the effect of 475°C embrittlement of a commercial grade DSS on tensile and impact behaviour. The significant changes observed in the aforementioned behaviour resulting from 475°C embrittlement were investigated through scanning and transmission electron microscopy (SEM+TEM).
- The effect of 475°C embrittlement on the cyclic stress-strain behaviour, cyclic hardening/softening behaviour, and cyclic life was studied by systematically increasing the total strain amplitude values through strain-controlled fatigue testing. The cyclic deformation mechanisms were recorded from transmission electron microscopy. A plausible correlation between cyclic deformation behaviour and cyclic strain localization features is proposed.
- The electrolytically polished surface of the stress-controlled fatigue tested DSS specimen in the aged condition was examined under scanning electron microscope (SEM) by interrupting the fatigue test at regular intervals. The fatigue crack initiation event is correlated to the crystallographic features obtained from electron backscattered diffraction (EBSD) pattern in SEM and analysed through orientation imaging microscopy (OIM) software. The cyclic strain localization in stress-controlled fatigue test is recorded through transmission electron microscopic examination.
- The aging characteristics at 475°C and the resulting embrittlement are discussed extensively combining the present findings and findings of other research groups and at the end some suggestions and scopes for future research are made based on these discussions.

The thesis is divided into six chapters including the introduction chapter. The second chapter summarizes the outline of the theoretical background based on which the scope of the present investigation was defined. The experimental techniques employed to achieve the

objectives of the present investigation are described in the third chapter. The results obtained during the present investigation are presented and discussed with the results obtained by other international research groups in the fourth chapter. Some of the significant findings of this investigation are summarised and critically discussed with the findings of other research groups in the fifth chapter. The concluding remarks and scope for further research in this area of investigation are discussed in the sixth chapter.

Chapter 2 Literature review

This chapter summarizes the outline of the theoretical background based on which the scope of the present investigation was defined. A brief outline of the fatigue behaviour of metallic materials and alloys is described in section 2.1. The emphasis is given on the characterization techniques used to study the fatigue behaviour of duplex stainless steel (DSS), i.e. cyclic deformation mechanisms, low-cycle fatigue and fatigue crack initiation. The importance of DSS as a structural material and the 475°C embrittlement, which changes the fatigue behaviour of DSS is described in section 2.2.

Fatigue behaviour of metallic materials and alloys

The degradation of material resulting from cyclic stress/strain is called fatigue damage. The cyclic stress/strain in the material may arise from fluctuating loads/displacements and/or temperature gradients. The metallic materials and alloys fail even when the peak tensile stress is below their yield strength. The fatigue behaviour is categorized depending on the causes that produce cyclic stress/strain in the material. Mechanical fatigue deals with fluctuation in externally applied loads/displacements at standard temperature and pressure [46]. Fracture resulting from the presence of temperature gradients that vary with time in such a manner as to produce cyclic stresses in a structure is termed as thermal fatigue [47]. Creep-fatigue results from load/displacement cycles associated with hold time at constant high temperature [48]. Thermo-mechanical fatigue refers to strain cycling associated with fluctuation in temperature [49]. Corrosion fatigue is a term used to describe the phenomena of cracking in materials under the combined action of cyclic stress and corrosive environment [50]. Rolling/sliding contact fatigue refers to fluctuation of load in conjunction with sliding and rolling contact between materials [51]. Fretting fatigue results from fluctuating stresses along with oscillatory relative motion and frictional sliding between surfaces [52]. The present section describes few aspects of mechanical fatigue behaviour.

The cyclic deformation mechanisms are described in subsection 2.1.1. The fatigue failure is initiated either at the sites of localized, permanent microstructural changes or from a

pre-existing defect. The design concept that characterizes the earlier situation is called total life approach to fatigue design and is described in the subsection 2.1.2. The design concept that characterizes the later situation is called defect tolerant approach to fatigue design and is described in the subsection 2.1.3.

2.1.1 Cyclic deformation mechanisms

The fatigue damage in metallic materials and alloys progresses through different stages. These stages are:

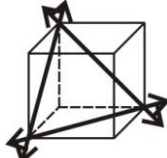
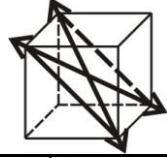
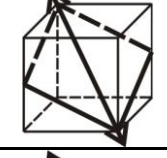
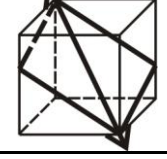
- Substructural changes leading to cyclic strain localization
- Crack initiation
- Growth and coalescence of initiated micro-cracks to form a dominant macro-crack
- Stable growth of the dominant macro-crack
- Unstable growth of the dominant macro-crack causing structural instability and final failure

However, before describing on different stages of fatigue damage, some fundamental aspects of slip, the predominant mode of plastic deformation in metallic materials and alloys are mentioned in the following paragraphs.

Dislocations produce atomic displacements on specific crystallographic planes called slip planes and along specific crystallographic directions in the slip planes called slip directions. The slip planes are usually the most densely packed planes and lower shear stress is required for atomic displacement. Slip direction is the closed packed direction within the slip plane. Slip system is the combination of preferred slip planes and slip directions on those specific planes along which dislocation motion occurs. Slip takes place on the $\{111\}$ octahedral planes and $\langle 1\bar{1}0 \rangle$ closed packed directions in metals with FCC crystal structure. There are four different types of $\{111\}$ slip planes and each plane contains three $\langle 1\bar{1}0 \rangle$ directions. The FCC lattice has (4 slip planes x 3 slip directions) 12 slip systems. BCC structure is not close-packed and does not contain a predominant plane of highest atomic packing. The $\{110\}$ planes has highest atomic density and slip commonly occurs in these

planes. However, slip also occurs in $\{211\}$ and $\{311\}$ planes. The slip direction in BCC metal is always $\langle\bar{1}11\rangle$. Table 2.1 shows the slip systems in FCC and BCC lattice.

Table 2.1: Slip systems in FCC and BCC lattice.

Crystal structure	Slip plane	Slip direction	Slip systems	Unit cell geometry
FCC (γ -Fe, Ni, Cu, Al, Ag)	$\{111\}$	$\langle\bar{1}\bar{1}0\rangle$	$4 \times 3 = 12$	
BCC (α -Fe, Mo)	$\{110\}$	$\langle\bar{1}11\rangle$	$6 \times 2 = 12$	
BCC (α -Fe, Mo)	$\{211\}$	$\langle\bar{1}11\rangle$	$12 \times 1 = 12$	
BCC (α -Fe, Mo)	$\{311\}$	$\langle\bar{1}11\rangle$	$24 \times 1 = 24$	

The process of slip begins in a pure metal single crystal when the shear stress on the slip plane in the slip direction reaches a required level called as critical resolved shear stress (CRSS). The slip process is considered in terms of the shear stress resolved on the slip plane in the slip direction. Figure 2.1 shows a cylinder of pure metal single crystal with cross-sectional area A under the action of a tensile force F . ϕ is the angle between the slip plane normal and the tensile axis, and λ is the angle between the slip direction and the tensile axis. The component of the applied force, acting in the slip direction is $F \cos \lambda$, and the area of the slip plane is $A/\cos \phi$. The shear stress (τ) resolved in the slip direction and the Schmid factor (m) are given in Eq. 2.1 and Eq. 2.2 respectively.

$$\tau = \frac{F \cos \lambda}{A / \cos \phi} = \sigma \cos \phi \cos \lambda \quad (2.1)$$

$$m = \cos \phi \cos \lambda \quad (2.2)$$

This is known as Schmid's law and has been experimentally proved for a large number of single crystals. The critical stress required to cause yielding is a function of the Schmid factor, m .

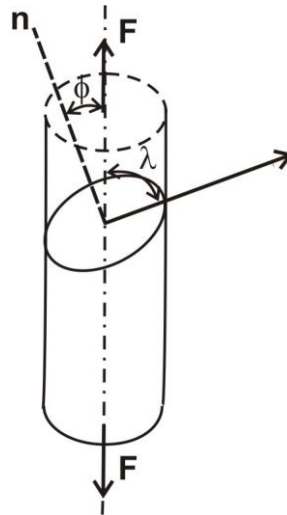


Fig. 2.1: Schematic diagram of a cylindrical single crystal showing orientation of slip plane and slip direction with respect to an external load.

Cyclic deformation leads to the generation of primary dislocations and formation of low energy dislocation structures [53-57]. The motion of dislocations in metallic materials and alloys are dealt with either a long-range stress models or short-range interaction approaches [56-57]. When $R > 5b$, where R is the separation distance between two dislocations and b , is the Burgers vector, the force exerted by a dislocation on another dislocation is inversely proportional to the separation distance [56]. This formulation of long-range force of a dislocation is valid as the local distortion of the lattice is negligible in comparison to the elastic straining of the material at large distances from the dislocation core. With this assumption the property of linear elasticity holds and the total force on a given dislocation can be computed by summing the individual long-range forces resulting from all other dislocations. However, for $R < 5b$, the large strains close to the dislocation core invalidate the assumption of linear elasticity [56]. These nonlinear interactions between dislocations are phenomenologically described and also been experimentally observed as rate

processes rather than force displacement relationships [53]. During cyclic loading of a metallic material and alloy, such close interactions between dislocations frequently occur [54]. Some of these important dislocation interaction events are annihilation of dislocation, dipole formation, junction formation, dislocation generation and immobilization of dislocations. The simplified physical definitions of these short-range interactions are given in the following paragraphs.

The event of cancellation of two dislocations of opposite Burgers vectors, which approach each other within a certain critical distance of separation, is called annihilation [56]. The critical distance of separation is a material parameter. Annihilation also occurs when dislocations leave the grain at the free surface, leaving behind a step of the height equal to Burgers vector, b . When more dislocations move out at the free surface, the step produced by them increases and surface roughness is produced [58-59]. Essmann and Mughrabi estimated the critical annihilation distance value of two screw dislocations (y_s) of opposite Burgers vectors given by Eq. 2.3 [58].

$$y_s \approx \frac{Gb}{2\pi\tau_g} \quad (2.3)$$

G is the shear modulus and τ_g is the shear stress required for dislocation glide. For copper, $y_s \approx 1.8 \mu\text{m}$ [58]. For mixed or edge dislocations, annihilation will occur when the attractive elastic force between two dislocations exceeds the force required for dislocation climb. The critical distance for annihilation of mixed dislocations (y_m) is given by Eq. 2.4.

$$y_m \approx \frac{Gb^4}{2\pi\kappa U_f \sin \psi} \quad (2.4)$$

U_f is the energy of formation of atomic defects, ψ is the angle between the Burgers vector and the sense vector of the dislocation, κ is $1-\nu < \kappa < \nu$ and ν is the Poisson's ratio. The critical distance for edge dislocation annihilation has been found to be of the order of $y_e \approx 1.6$

nm, which is much smaller than the y_s value for screw dislocations [56]. Figure 2.2 shows a schematic diagram of the annihilation distance for screw (y_s) and edge (y_e) dislocations.

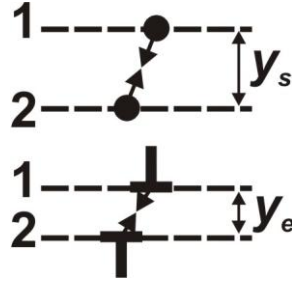


Fig. 2.2: A schematic diagram showing critical annihilation distance for screw and edge dislocations [46].

When two edge dislocations of opposite Burgers vectors approach each other, they can achieve a stable configuration if they remain at a distance greater than the critical distance for annihilation (y_e). This configuration is known as a dipole and it can exist as a vacancy or interstitial type configuration. Typical dipole lengths are of the order of tenth of micron [60]. Dipoles are composed only of edge dislocations since screw dislocations can easily annihilate by the cross-slip mechanism. Once formed, a dipole does not move as a whole if the external or internal stresses are changed, but it changes its configuration slightly. Application of an applied stress causes a slight change in the relative angle between the dislocations, which constitute the dipole.

Two dislocations separated by a sufficient distance to form a dipole will not necessarily form a dipole configuration. It is found that in order to form a stable configuration, the stress on a dislocation must be less than the passing shear stress for a dipole (τ_p) given in Eq. 2.5.

$$\tau_p \approx \frac{Gb}{8\pi(1-\nu)S_d} \quad (2.5)$$

S_d is the slip plane spacing. Figure 2.3 shows a schematic diagram of dislocation dipole loop and L_d is the length of the dipole loop. The dislocation bowing stress is given by Eq. 2.6.

$$\tau_{\text{bow}} \approx \frac{Gb}{L_d} \quad (2.6)$$

The criterion for the stability of the dipole is obtained by equating τ_p and τ_{bow} values and is given in Eq. 2.7.

$$\frac{L_d}{S_d} \approx 15 \quad (2.7)$$

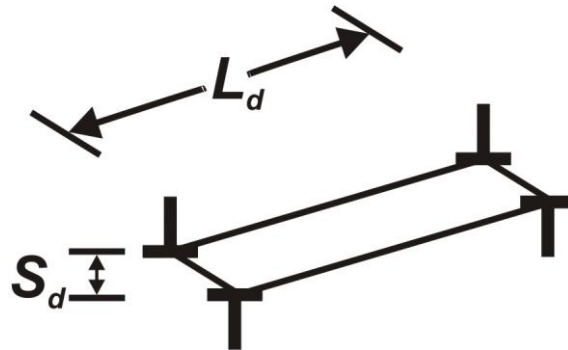


Fig. 2.3: A schematic diagram of dislocation dipole [46].

A dipole does not necessarily represent the perfect alignment of two dislocations of opposite Burgers vectors. In fact, the relative angle between two dislocations in a dipole varies from 25° to 65° , with an average around 45° [61]. The latter angle represents the position of minimum interaction energy of dislocations within dipole.

Those dislocations, which experience a net attractive force with respect to each other are called attractive dislocations. When two attractive dislocations approach each other, they eventually intersect. The intersection is an annihilation event if the two dislocations are of opposite Burgers vectors. If they are not of opposite Burgers vectors, then one of three events can occur: (a) they lock together, forming a Lomer-Cottrell barrier; (b) they draw each other out, forming a jog intersection; or (c) they intersect and then pass each other [56]. The two dislocations will pass each other if the net stress on one of the dislocations is approximately greater than the pinning stress for dislocations (σ_p), which is given by Eq. 2.8.

$$\sigma_p = \frac{Gb}{2\pi\lambda_d} \quad (2.8)$$

λ_d is the inter dislocation separation distance.

Dislocation multiplication is primarily attributed to the Frank-Read mechanism for glide processes [62-63]. During dislocation creep, the Frank-Read source is dominant and multiplication occurs by pinning of the dislocation, bowing out, and wrapping around the pinning points. Prinz and Argon [62] have identified anchoring points as dislocation dipoles and multiple bundles in the evolution of cell-wall-type structures. The bowing out of free segments from these bundles is considered a major generation source [63]. Multiplication occurs if the total force on a dislocation exceeds the Orowan stress (σ_o) for dislocation reproduction [56]. The Orowan stress criterion is given by Eq. 2.9.

$$\sigma_o = \frac{2Gb}{\lambda} \quad (2.9)$$

λ is the inter obstacle spacing. If this criterion is satisfied, dislocations are capable of multiplying at a rate given in Eq. 2.10.

$$\dot{\rho} = \rho \frac{v_g}{\lambda} \quad (2.10)$$

ρ is the total dislocation density and v_g is the dislocation glide velocity.

Cyclic loading leads to short-range dislocation interactions and subsequent strain localization [56-57]. The free surface is the preferential site for the onset of strain localization in cyclically stressed metal [64]. The plastic deformation predominantly proceeds through slip mechanisms. Low-cycle (high-stress) fatigue results in relatively homogenous macro plastic deformation in all grains. The activities of slip and twinning are observed in a large number of grains. High-cycle (low-strain) fatigue results in plastic deformation only in a

fraction of favourably oriented grains. The peak tensile stress in high cycle fatigue falls below the yield strength of the material. The strain localization and eventual failure even at this stress level indicates the irreversible nature of cyclic slip. The physical and mathematical aspects of cyclic slip irreversibility are extensively researched [65-69]. Some of the reasons of cyclic slip irreversibilities are [46]:

- The slip displacement during unloading cycle is less than loading cycle due to the absorption of an embrittling species or due to the oxidation of slip steps
- Random distribution of slip with the progressive preferential deepening of valleys at surface
- Cross slip of screw dislocation and different paths for their forward and reverse glide during complete fatigue cycle
- Dislocation-dislocation interactions leading to the formation of nodes, jogs or dislocation locks which impede motion during the part of a fatigue cycle
- Production of point defects during saturation due to the dynamic equilibrium between dislocation generation and annihilation
- Irreversibility due to sharp changes as well as differences in dislocation back stress due to slip on different glide planes during the tension and compression portion of fatigue

Sometimes there is spatial organization of dislocations into some specific features in the bulk of the cyclically stressed material depending on crystal structure (FCC, BCC, HCP), plastic strain amplitude ($\Delta\varepsilon_p/2$) and temperature [6-10,64,70-71]. The formation of these structures determines the cyclic hardening/softening response of the material. The common features observed in the bulk under TEM are channel-vein structure, bundles, loop patches, persistent slip bands (PSB), planar arrays, and dislocation-cell structures. A simplified description on some of these dislocation spatial arrangements is given in the following paragraphs.

As already discussed, continued cycling results in the accumulation of dislocations in the form of mutually trapped primary edge dislocation dipoles. This network of dipoles is referred to as dislocation veins or bundles. Their development and the increase of dislocation density are the reasons for the rapid hardening in the early stage of fatigue [72]. The dislocations in the channel-vein structure travel back and forth across the channels during the

cycles. The veins have a dislocation density of $3 \times 10^{15} / \text{m}^2$ and a volume fraction of 50%. The dislocation density in the channels is $10^{11} / \text{m}^2$ [46]. During fatigue, the channel-vein structure transforms into a ladder-like structure known as PSB. The schematic diagram of the channel-vein structure and PSB is shown in Fig. 2.4.

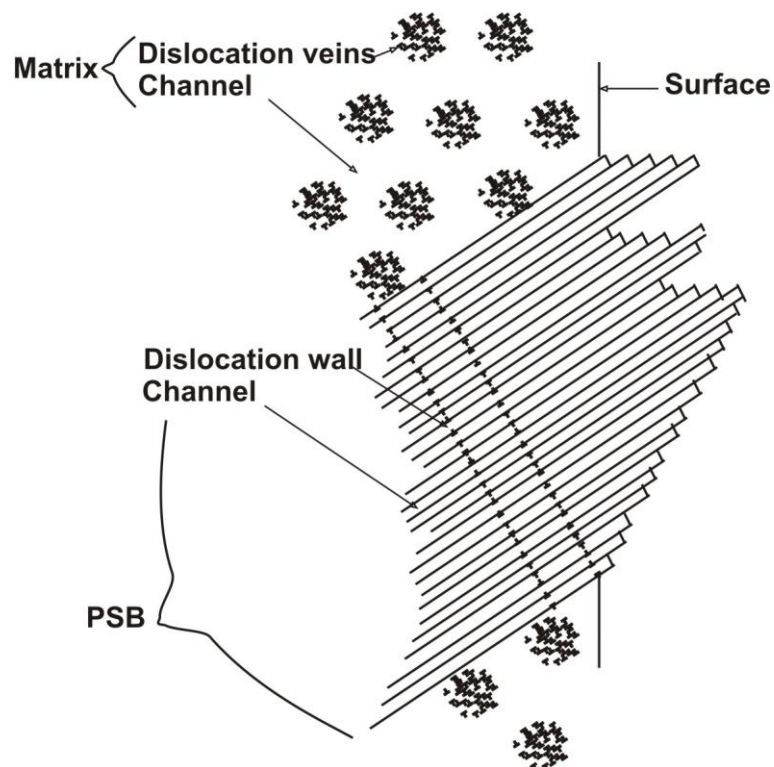


Fig. 2.4: A schematic diagram of channel-veins and PSB.

The PSBs follow the primary slip direction, i.e. the direction of the Burgers vector of those dislocations, which experience the maximum resolved shear stress, and they grow in length and in width until they span the entire crystal. The PSBs give rise to more plasticity than the channel-vein structure that surrounds them. As in the channel-vein structure, dislocations travel from the dislocation dense walls through the channel to the next wall. The walls of a PSB are regularly spaced and have a dislocation density of around $6 \times 10^{15} / \text{m}^2$ [46]. The TEM micrograph of the ladder like PSB and channel-vein structure is shown in Fig. 2.5.

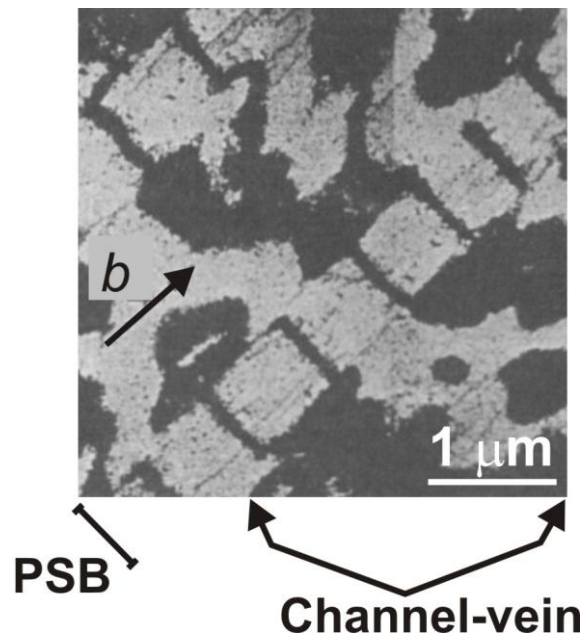


Fig. 2.5: PSB and channel-vein structure [9].

With increase in strain amplitude the secondary slip is activated and results in the formation of labyrinth and cell structure [46]. The loop patches are observed at low plastic strains, vein and PSB at intermediate plastic strains, and dipolar walls at high strains in fatigued polycrystalline copper. At very high strain the dipolar walls become more cellular. Figure 2.6 shows a map of typical dislocation structures of FCC materials as a function of number of cycles to failure (N_f) as well as the plastic strain range ($\Delta\varepsilon_p$) and the slip character of the material. For a material with wavy slip character, the dislocation structure could reach from those typical of single slip, namely dipole, dipolar bundles and PSB, to those characteristics of multiple slip, e.g. labyrinth and cell structure, depending on the plastic strain range.

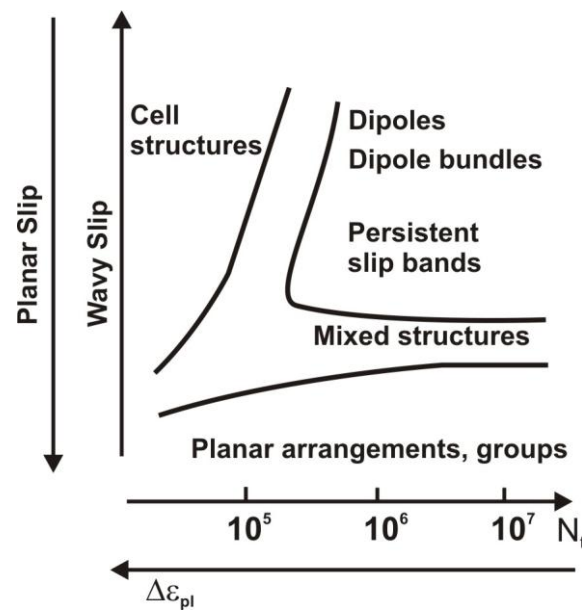


Fig. 2.6: Different spatial dislocation arrangement as a function of slip mode, plastic strain range and cyclic life [73].

The evolution of surface roughness is a very important structural feature of fatigue damage in metallic materials and alloys [65-69]. The grains having a free surface have less constraint to plastic deformation compared to a grain in the body of the metal that is surrounded by other grains [74]. A simple verification that the surface layer is the critical volume for the crack initiation has been performed by the periodic removal of thin surface layer with the relief produced by cycling and subsequent fatigue loading. This procedure increases the fatigue life many times. Similarly, surface treatments such as case-hardening, obtaining a scratch free and strain free surface are observed to enhance the fatigue life [66]. The fractographic examination of fatigue-tested samples also reveals the surface as sites for crack initiation. In certain circumstances, however, cracks may form in the interior of a specimen at inclusions or flaws or below hardened surface layers [66]. As shown in Fig. 2.7 monotonic loading leads to the formation of coarse staircase like surface steps whereas cyclic loading produces fine sharp peaks and valleys.

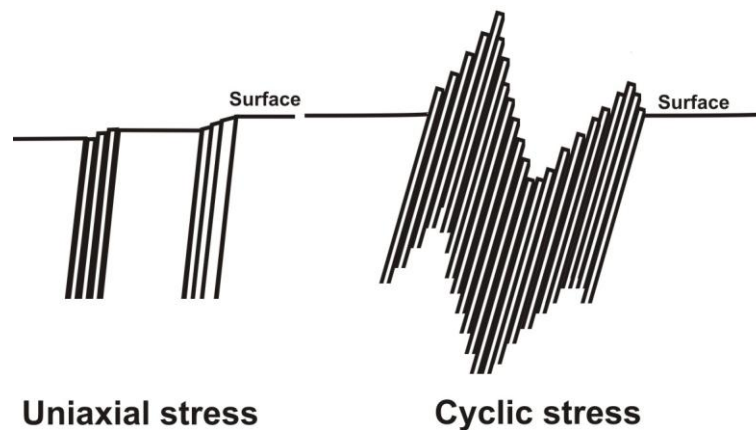


Fig. 2.7: Slip geometry at the material surface [66].

The most common features observed on an electrolytically polished free surface of a specimen subjected to cyclic loading are the slip markings and surface reliefs [67]. These features are commonly observed under SEM. The use of EBSD technique has made it possible to relate crystallographic parameters to the surface strain localisation features [68]. The slip markings are intersections of the active slip planes with the surface. At the beginning of the cycling, fine slip markings are observed on the primary slip system. The number of slip traces increases with progress of cyclic deformation. The increase in visible sliplines soon reaches a saturation value, which is observed as distorted regions of heavy slip [69]. Slip markings are sometimes reported being observed at stresses below the fatigue limit of ferrous materials [66]. Therefore, the occurrence of slip and appearance of slip markings during fatigue does not necessarily mean that a crack will initiate.

Recently atomic force microscopy (AFM) is used to map the surface reliefs more precisely [75]. The PSB exhibit typical surface relief and are related to the coarse slip bands consisting of extrusions and intrusions. This has also been experimentally proved by examination of foils prepared from electrodeposited specimens in such a way that the surface relief covered by electrodeposit and the dislocation structure below the surface were visible simultaneously under TEM [67]. Figure 2.8 shows a schematic diagram of extrusions and intrusions on the surface.

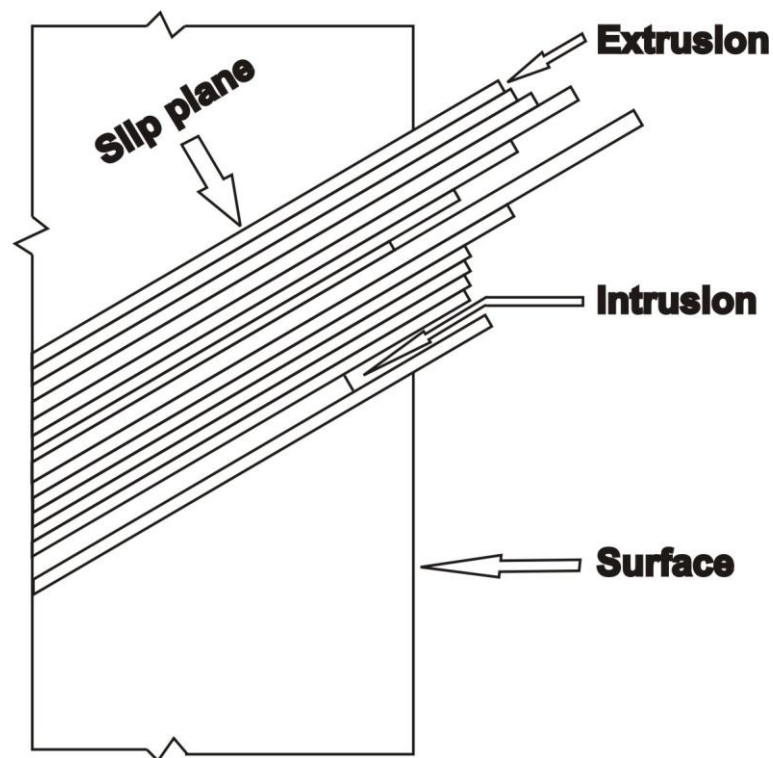


Fig. 2.8: Schematic diagram showing extrusions and intrusions.

2.1.2 Crack initiation and growth

The development of surface roughness during cyclic loading is associated with dislocation interactions and their spatial arrangements. The fatigue crack initiation is explained through these dislocation events [76]. The models for fatigue crack initiation explained through dislocation interactions are either based on continuum mechanics or based on discrete dislocation events, which explains experimental observation of crack nucleation by a sequence of physical mechanisms. Some experimental observations of fatigue crack nucleation and few of the physical mechanism-based models are explained in the next paragraphs.

In some metallic materials and alloys the topography resulting from surface roughness is very expressive; marked peaks and valleys are created on the surface. In other materials a rather homogeneous slip is observed with less expressive topography. In all cases, however, the surface roughness results in a stress concentration. The sites of crack initiation are influenced both by external parameters, such as temperature, environment and imposed

stress/strain amplitude, and internal parameters, such as grain size and grain orientation [77-79]. For example, increase in test temperature changes the crack initiation sites from slip bands to grain boundaries and increase in stress amplitude also promotes grain boundary crack initiation [72]. The environment significantly influences the crack nucleation. The formation of surface oxide or corrosion product layers in the slip steps can influence the development of surface topography. The surface slip bands, grain boundaries, intrusions/extrusions, and twin boundaries are observed to be the sites for the nucleation of fatigue cracks.

The localized plastic shear and the accumulation of irreversible plastic strain in the slip bands on the surface of a metal result in the formation of residual vertical displacements. As a result crystallographically oriented cracks known as stage I cracks form with the minimum depth from 1 to 10 μm [68]. The fatigue microcracks continue to grow within the slip bands in the direction of the maximum shear stresses. With increase of crack length the shear crack is gradually reoriented into the plane of action of the maximum tensile stress and is called stage II crack. The schematic diagram of stage I crack initiation and reorienting to stage II crack is shown in Fig. 2.9.

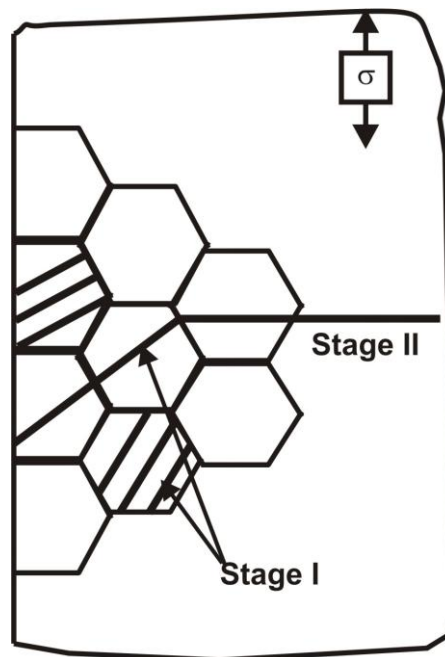


Fig. 2.9: A schematic diagram of stage I and stage II cracking.

The grain-boundary cracking is commonly observed in brittle solids due to the residual stresses induced by thermal contraction mismatch between adjacent grains. The fatigue crack nucleation at grain boundaries in ductile solids is less common and depends on the external variables such as temperature, grain boundary embrittlement, imposed plastic strain amplitude or crystallographic parameters. At high temperature, crack may initiate at grain boundary, when cavities form or grain boundary sliding occurs, e.g. hot deformation of steel containing high sulphur. Sensitization of stainless steel is another example of grain boundary embrittlement. The plastic strain amplitude also influence the fatigue crack initiation behaviour: (a) at low to intermediate plastic strain amplitude, the impingement of PSB at grain boundaries causes cracking [80] and (b) at high plastic strain amplitudes grain boundary cracking occurs as a consequence of surface steps formed at the boundary [81]. Kim and Laird noted that fatigue cracks nucleate at grain boundaries if: (a) these boundaries separate highly misoriented grains; (b) the active slip system of at least one of the grains is directed at the intersection of the boundary with the specimen surface; and (c) the traces of the high angle grain boundaries in the free surface make a large angle ($30\text{-}90^\circ$) with tensile stress axis [81].

Mott proposed the first fatigue crack initiation model based on the fatigue mechanism [82]. He suggested that vacancies are generated below the specimen surface resulting in extrusions, as he experimentally observed more extrusion than intrusion on the surface. From this observation he concluded that vacancies accumulate inside and these clusters of vacancies grow and form crack underneath the surface. Antonopoulos *et al.* [83] proposed a model extending the idea of vacancy dipole. According to this model vacancy dipoles are more likely to form than interstitial dipoles due to lower energy of formation and they outnumber the interstitial dipole by a factor of two.

The Essmann-Gösele-Mughrabi (EGM) [64] model also proposed the same observation, i.e. pre-dominance of vacancy over interstitial dipoles, and schematically clarified the mechanism. This model proposed the sequence of events as shown in Fig. 2.10. A pair of dislocations (X–Y) nucleates and dislocation X glides to the surface of the grain and produces a step. The dislocation Y is still inside the bulk. Another dislocation pair is generated on adjacent glide plane. Dislocation Z of the newly generated dislocation pair is

forming a vacancy dipole with dislocation Y. Similar interactions, i.e. gliding and formation of vacancy dipoles continue to occur in the neighboring planes resulting in the formation of a band of dislocation dipoles as shown in the Fig. 2.10 by the dark dislocations. The endpoints of this band are dislocations with the half-plane inside the PSB. A similar band develops from the lower left-hand to the upper right-hand edge depicted by the grey dislocation dipoles. The slope of the bands is a material property.

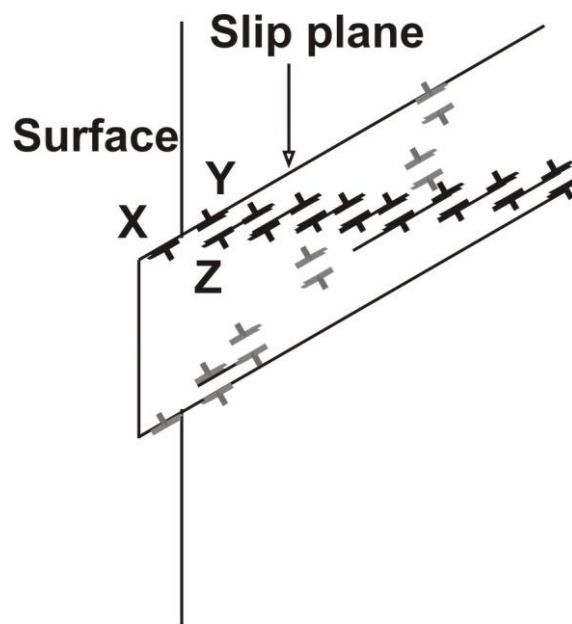


Fig. 2.10: The EGM model for fatigue crack nucleation.

Neumann developed a model for the fatigue striations based on the activation of two slip systems, as illustrated in Fig. 2.11 [54]. In the first tensile stroke, slip planes 1 and 2 get activated after each other and the material opens up. In the compression phase the dislocations glide back. However, they cannot totally heal the material because both side of the evolving crack touch macroscopically like ordinary pieces of metal. Therefore, a crack has initiated along slip plane 1 to the intersection with slip plane 2. Consequently, the crack propagates in a zig-zag fashion, as shown by the dashed line in Fig. 2.11.

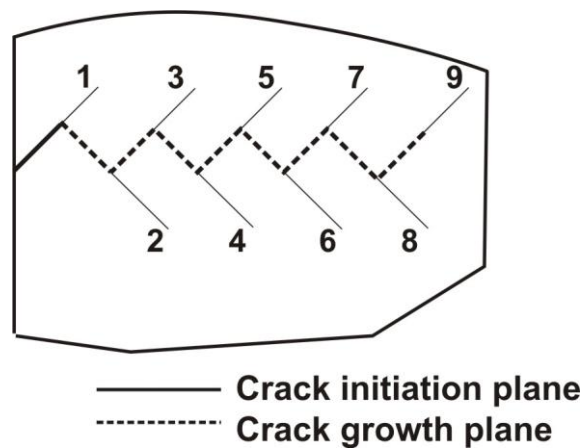


Fig. 2.11: Neumann model for fatigue crack nucleation.

The relative proportion of the total cycles to failure that are involved with each stage depends on the test conditions and the material. In general, larger proportions of the total cycles to failure are involved with the propagation of stage II cracks in high-strain, low-cycle fatigue, while stage I crack growth comprises the largest segment for low-stress, high-cycle fatigue. If the tensile stress is high, as in the fatigue of sharply notched specimens, stage I crack growth may not be observed at all.

The stage I crack propagates initially along the slip bands. In a polycrystalline metal the crack may extend for only a few grain diameters before the crack propagation changes to stage II. The rate of crack propagation in stage I is generally very low as compared to the crack propagation rates for stage II [46]. The fracture surface appearance of failure resulting from the growth of stage I crack is practically featureless. Failure to observe striations on a fatigue surface may be due to a very small spacing that cannot be resolved with the observation method used. Figure 2.12 shows schematically the growth of stage I crack along the slip markings.

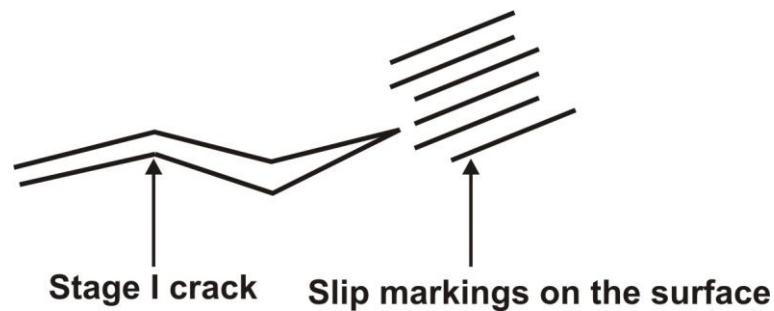


Fig. 2.12: Growth of stage I crack along slip markings.

The stage-II crack growth in most of the engineering alloys results in the formation of fatigue striations. Laird [84] has proposed the most popular model for the formation of fatigue striation. The increment of crack extension in this model is visualized as successive plastic blunting and re-sharpening of the crack under repeated load reversals. The blunting and opening of a crack occur in the tensile half-cycle whereas the re-sharpening and closure occur in compression half-cycle. The closure or re-sharpening of a crack cannot fully negate the blunting and its associated extension, and the net crack growth occurs during a fatigue cycle leading to the formation of striations. The model for formation of fatigue striations is schematically shown in Fig. 2.13.

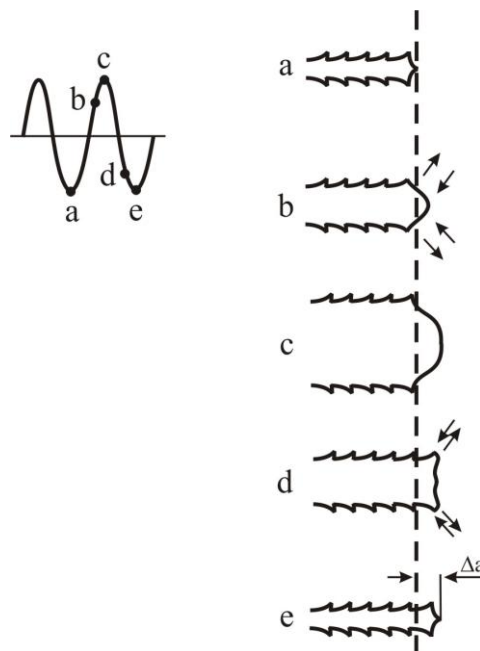


Fig. 2.13: Plastic blunting and resharpenering, stage II crack propagation.

2.1.3 Total life approach

This is the classical approach to fatigue design. In this approach an unnotched, smooth and electrolytically polished specimen is subjected to a constant amplitude stress/strain cycling until failure occurs. The measured fatigue life includes the number of the cycles both to initiate and grow a fatigue short crack to a dominant crack and propagate of the dominant crack to final failure. The total life is the sum of initiation life and propagation life. The fatigue failures at higher number of cycles ($>10^5$) and lower stress amplitudes are characterized under stress-based approach alternatively called high cycle fatigue (HCF). The fatigue failures at lower number of cycles ($<10^5$) and high strain amplitudes are characterized under strain-based approach, alternatively called low cycle fatigue (LCF). The material response to the cyclic deformation differs depending on the controlling variable. The essential characteristics include cyclic hardening, cyclic softening, cyclic mean stress relaxation, and cyclic creep.

In the stress-based approach the total life to failure is characterized in terms of cyclic stress amplitude and is often termed as stress life or $S\sim N$ approach [3]. The imposed tension-tension and tension-compression stress cycle and different parameters for fatigue characterization are shown in Fig. 2.14.

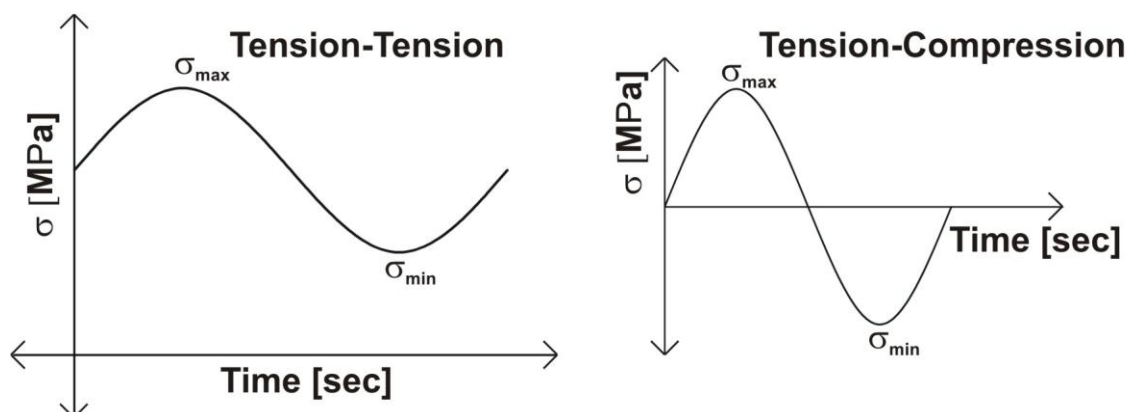


Fig. 2.14: A schematic diagram of the imposed stress cycle.

Equations 2.11 to 2.14 describe the expressions for stress range ($\Delta\sigma$), stress amplitude ($\Delta\sigma/2$), mean stress (σ_{mean}), and load ratio (R).

$$\Delta\sigma = \sigma_{\max} - \sigma_{\min} \quad (2.11)$$

$$\frac{\Delta\sigma}{2} = \frac{1}{2}(\sigma_{\max} - \sigma_{\min}) \quad (2.12)$$

$$\sigma_{\text{mean}} = \frac{1}{2}(\sigma_{\max} + \sigma_{\min}) \quad (2.13)$$

$$R = \frac{\sigma_{\min}}{\sigma_{\max}} \quad (2.14)$$

The two parameters frequency and waveform (square, triangular, sinusoidal) in general influence fatigue only in case of extreme environments such as elevated temperature, high humidity etc. The tests are normally performed on cylindrical smooth specimen at different stress amplitudes till failure. The tests are valid only when failure occurs by the growth of a microstructurally short crack initiated during the course of cycling. If an already existing defect leads to the failure of the specimen then the test is considered invalid. For this reason number of tests are performed at particular stress amplitude to obtain the authentic life. Figure 2.15 shows a plot between applied stress amplitude and number of cycles to failure (N_f) known as the $S\sim N$ curve.

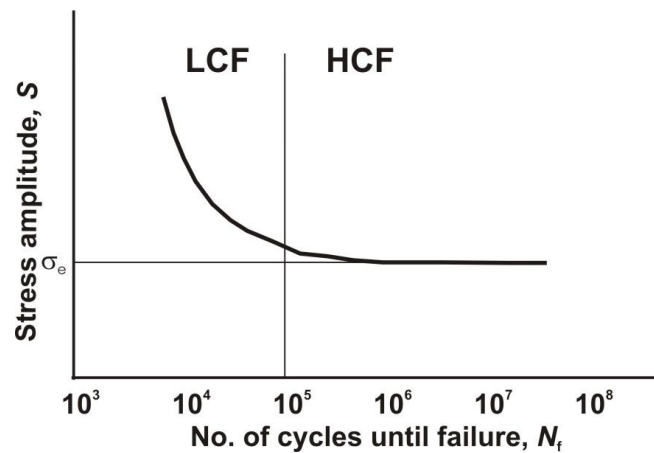


Fig. 2.15: A schematic illustration of $S\sim N$ curve.

σ_e is known as the endurance limit of the material. If the stress is below σ_e the component has effectively infinite life. $\sigma_e \approx 0.35\sigma_{\text{uts}}-0.50\sigma_{\text{uts}}$ for most steel and copper alloys [3]. If the material does not have a well defined σ_e , then it is arbitrarily defined as the stress that gives fatigue life (N_f) of 10^7 cycles. A log-log plot between $\Delta\sigma/2$ and $2N_f$ ($2N_f$ represents the number of reversals to failure, one cycle equals two reversals) results in a linear relationship for small plastic strain amplitudes. The relationship, (Basquin law) between stress amplitude and fatigue life is given in Eq. 2.15 [3].

$$\frac{\Delta\sigma}{2} = \sigma_f' (2N_f)^b \quad (2.15)$$

σ_f' is the fatigue strength coefficient (for most metals $\sigma_f' \approx \sigma_f$, where σ_f is the true fracture strength), b is the fatigue strength exponent (~ -0.05 to -0.12).

The philosophy of the strain based approach to fatigue design has come from the power plants, nuclear pressure vessels, steam turbines, and heat exchangers where certain components are subjected to repeated thermal stresses as a result of temperature gradients [85]. The temperature gradient occurs as a result of thermal transients that can arise from operations such as start-up and shut-down. In order to represent the component behaviour in a laboratory test, the thermal strains are replaced by mechanical strains and controlled under isothermal conditions [85]. The slow start-up and shut-down cycle is replaced by a symmetrical and continuous cycle of equal strain rates in tension and compression and is known as strain based design to fatigue design. Figure 2.16 shows schematic representation of variation of strain (controlled) and stress (uncontrolled) with number of cycles in a strain-controlled fatigue test. The material is said to be cyclically hardening, when the uncontrolled stress values increases as shown in Fig. 2.16b, and the material is said to be cyclically softening, when the uncontrolled stress values decrease as shown in Fig. 2.16c.

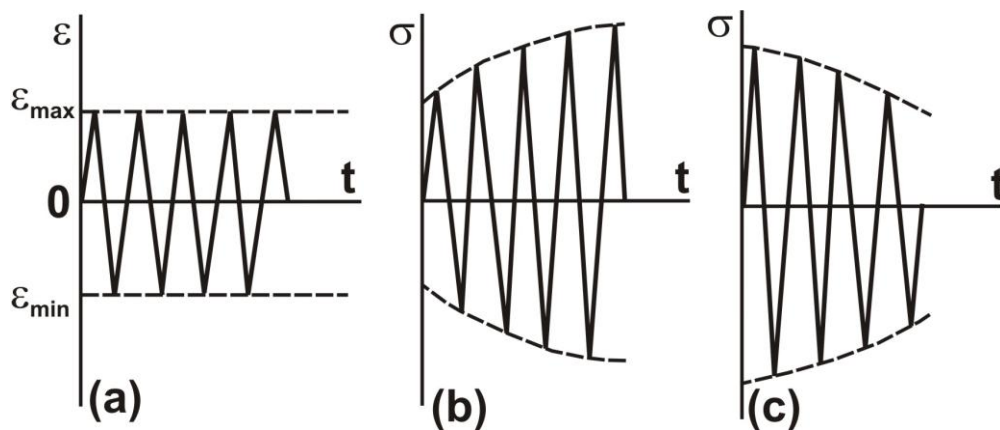


Fig. 2.16: (a) Constant amplitude strain cycling; (b) cyclic hardening; (c) cyclic softening.

In constant amplitude strain or plastic strain controlled fatigue, the resulting stress values are registered as a function of number of cycles, N to characterize the material behaviour. Fig. 2.17 shows a schematic representation of variation of uncontrolled stress with increase in number of cycles. These curves are called as cyclic hardening/softening or cyclic deformation curves. In simple cases the cyclic deformation curve can be divided into three parts. The cyclic hardening/softening (depending on the pretreatment of the material, deformed, annealed) is followed by a pronounced plateau of cyclic saturation. In the end there is inhomogeneous deformation of the dominant macrocrack, which finally leads to the failure of the specimen.

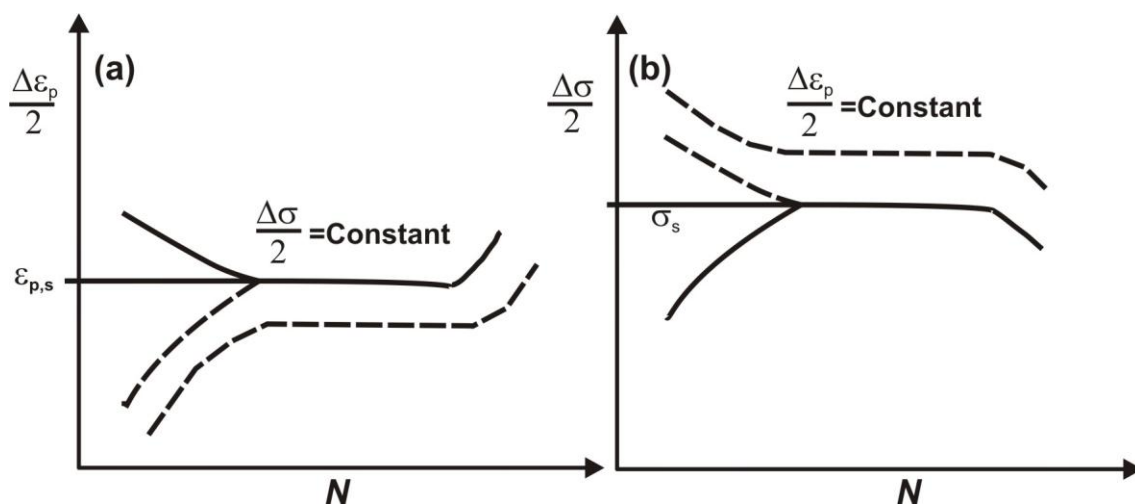

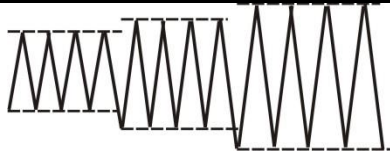
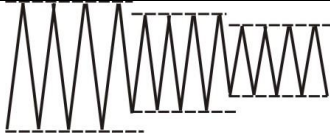
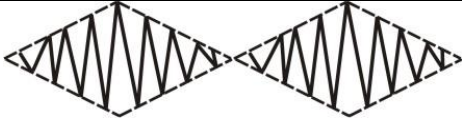


Fig. 2.17: Cyclic deformation curves [73].

An appropriate determination of the cyclic stress-strain (CSS) relationship is also of key importance in the description of basic cyclic deformation behaviour [86]. While obtaining the monotonic stress-strain curve is quite straightforward by tensile tests, the experimental determination of the CSS Curve (CSSC) is largely dependent on experiences as well as assumptions. The most frequently adopted methods are the single-step method (SST), the multiple-step method (MST) and the incremental step method (IST) [85]. Common to these methods is that the tips of the stable hysteresis loops are connected to form the CSSC. The various methods used to determine CSSC and corresponding schematic diagrams of strain cycles are mentioned in Table 2.2. Figure 2.18 shows stable hysteresis loops corresponding to tests conducted at different values of constant strain amplitudes for the DSS studied.

Table 2.2: Methods for determining CSSC.

Test method	Abbreviation	Schematic strain cycles
Single step test	SST	
Multiple step test (I)	MST (I)	
Multiple step test (D)	MST (D)	
Incremental step test	IST	

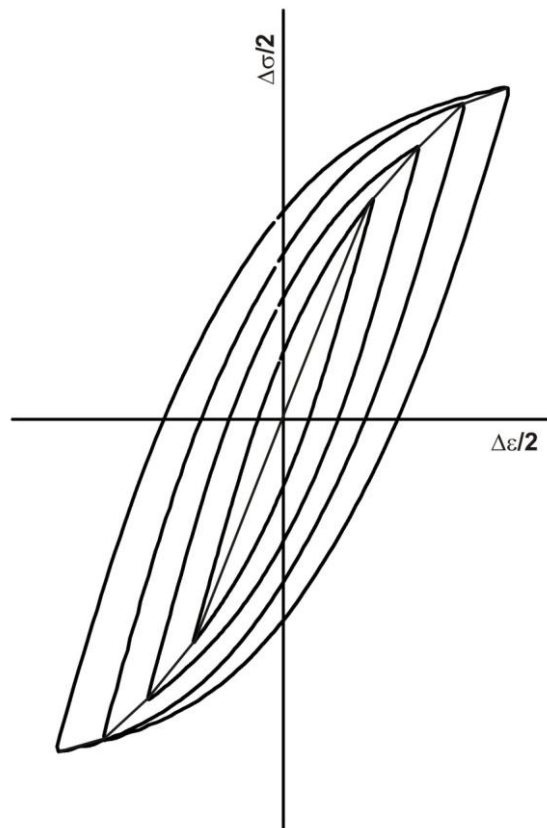


Fig. 2.18: Stable hysteresis loops at different values of total strain amplitudes for the DSS studied in this work.

The criterion for the stable hysteresis loop becomes a crucial issue because there is not a unified definition for the stable state. For instance, with the single-step method, a half-life criterion is conventionally adopted in which the hysteresis loop at 50% life is assumed as the stable one. For a material that does not reach a saturation state before specimen failure, however, this criterion becomes arbitrary and hence, has little physical implication. Moreover, different methods usually result in divergent CSSC for a definite material.

The mathematical expression for the cyclic stress-strain curve, which is satisfactory for most engineering metals is obtained if the total strain amplitude ($\Delta\varepsilon/2$) is separated into its elastic component ($\Delta\varepsilon_e/2$) and inelastic component ($\Delta\varepsilon_{pl}/2$) as given in Eq. 2.16.

$$\frac{\Delta\varepsilon}{2} = \frac{\Delta\varepsilon_e}{2} + \frac{\Delta\varepsilon_{pl}}{2} = \frac{\Delta\sigma}{2E} + \left(\frac{\Delta\sigma}{2K'}\right)^{1/n'} \quad (2.16)$$

K' is the cyclic strength coefficient and n' is the cyclic strain hardening exponent. The constitutive relationship between the stress amplitude and plastic strain amplitude is strain rate and temperature dependent and is given in Eq. 2.17.

$$\frac{\Delta\sigma}{2} = f\left(\frac{\Delta\varepsilon_{pl}}{2}, \dot{\varepsilon}, T\right) \quad (2.17)$$

$\dot{\varepsilon}$ is the strain rate, T is the temperature. At constant strain rate and temperature, the above equation reduces to Eq. 2.18.

$$\frac{\Delta\sigma}{2} = K' \left(\frac{\Delta\varepsilon_{pl}}{2}\right)^{n'} \quad (2.18)$$

The value of n' lies between 0.05 and 0.25 for metals and alloys. A comparison between monotonic and cyclic behaviour of a number of materials leads to some quantitative conclusion regarding cyclic hardening and softening. Materials with high monotonic exponent (n) will cyclically harden while those with a low n value may cyclically soften. A mixed or stable cyclic behaviour can be expected at intermediate values of n . The cyclic strain hardening exponent n' is about 0.15 for materials with a wavy slip mode and lies between 0.075-0.1 for materials with planar slip mode. In general fully annealed metals cyclically harden and heavily cold worked metals cyclically soften [85].

In case of single parameter damage representation the life to initiate a macrocrack is generally termed as fatigue failure criteria and is written as given in Eq. 2.19.

$$\psi = q(t) \quad (2.19)$$

ψ is any damage parameter and t is the total life in terms of cycles N_f or reversals to failure $2N_f$. For low-cycle fatigue life, Coffin and Manson independently established that the damage parameter is plastic strain amplitude ($\Delta\varepsilon_{pl}/2$) and can be linearized on a log-log coordinate with $2N_f$. The Coffin-Manson relation can be written in the form:

$$\frac{\Delta\varepsilon_{pl}}{2} = \varepsilon'_f (2N_f)^c \quad (2.20)$$

ε'_f is the fatigue ductility coefficient and c is the fatigue ductility exponent.

A number of phenomena in cyclic behaviour can be deduced from the shape of the hysteresis loop. While the CSSC describes the relationship between the stable stress and the strain amplitudes, it does not in general describe the hysteresis loop branches. Masing originally suggested that either branch of the hysteresis loop is geometrically similar and they can be obtained from the monotonic curve when scaled by a factor of two. This assumption is modified by replacing the monotonic curve by CSSC. Then a material is said to exhibit Masing type behaviour when the hysteresis loop branches (ascending or descending one) can be described by CSSC magnified by a factor of two. For this type of material, when stable hysteresis loops of various strain amplitudes are transferred to a common origin, the bottom tip of the hysteresis loops, the upper branch forms a unique curve. Figure 2.19 shows the schematic diagram of a Masing-type material. Materials whose behaviour differ from the above description are termed non-Masing type [85]. Thus the ascending hysteresis loop branch can be described by Eq. 2.21.

$$\Delta\varepsilon = \frac{\Delta\sigma}{E} + 2\left(\frac{\Delta\sigma}{2K'}\right)^{1/n'} \quad (2.21)$$

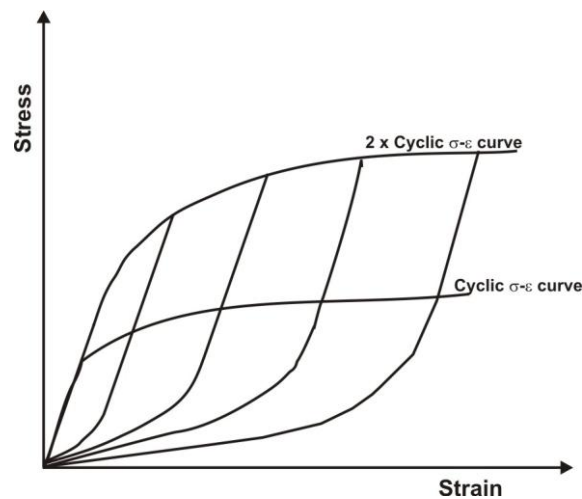


Fig. 2.19: A schematic illustration of Masing behaviour.

2.1.4 Defect tolerant approach

The metallic materials or alloys that are used for load bearing structures are either as-cast or wrought (rolled, forged or extruded). These materials generally have some defects. The pre-existing defect (a) grows to a critical size (a_c) before the final catastrophic failure. The total life approaches discussed so far cannot deal with defects already existing in the structure. The life may be considered solely as the number of cycles to propagate one such defect to a critical size before the onset of final catastrophic failure. The applied load and geometry of the defect determines fatigue life. This is called defect tolerant approach. The defect tolerant approach to fatigue design employs a fracture mechanics concept utilising the stress intensity factor to determine the crack growth rate. Fracture mechanics considers the stress field (and not just an average stress) and its relation with material discontinuity (crack). The approach relies on defects within the structure being monitored and the component retired when these reach a critical length.

Paris and Erdogan [4] were the first to suggest that the fatigue crack propagation per cycle (da/dN) can be related to the range of stress intensity factor (ΔK) [4]. They examined a number of alloys and realized that plots of crack growth rate against range of stress intensity factor gave straight lines on log-log scales. The expression is given in Eq. 2.22.

$$\frac{da}{dN} = C\Delta K^m \quad (2.22)$$

m and C are Paris constants. For the first time, it became possible to make a quantitative prediction of residual life for a crack of a certain size. This simply required finding limits on the integration in terms of crack size, which could be done by finding the final size which caused fast fracture from the relationship between fracture toughness and crack size given in Eq. 2.23.

$$K = Y\sigma\sqrt{\pi a} \quad (2.23)$$

Y is a dimensionless parameter that depends on geometry and mode of loading. Substitution of ΔK value in Eq. 2.22 results in Eq. 2.24.

$$\frac{da}{dN} = C\Delta K^m = C(Y\Delta\sigma\sqrt{\pi a})^m \quad (2.24)$$

Separation of the variables a and N and substitution for the range of stress intensity by the equivalent equation in terms of stress and crack size results in Eq. 2.25.

$$\int_{N_i}^{N_f} dN = \int_{a_i}^{a_f} \frac{da}{CY^m\Delta\sigma^m(\pi a)^{\frac{m}{2}}} \quad (2.25)$$

It was later realised that this law applies to growth rates in the range of 10^{-3} mm/cycle to 10^{-6} mm/cycle, and that the fatigue crack growth rate curve was sigmoidal in shape when growth lower and higher than this range were included. Figure 2.20 is a schematic diagram of the $da/dN \sim \Delta K$ curve.

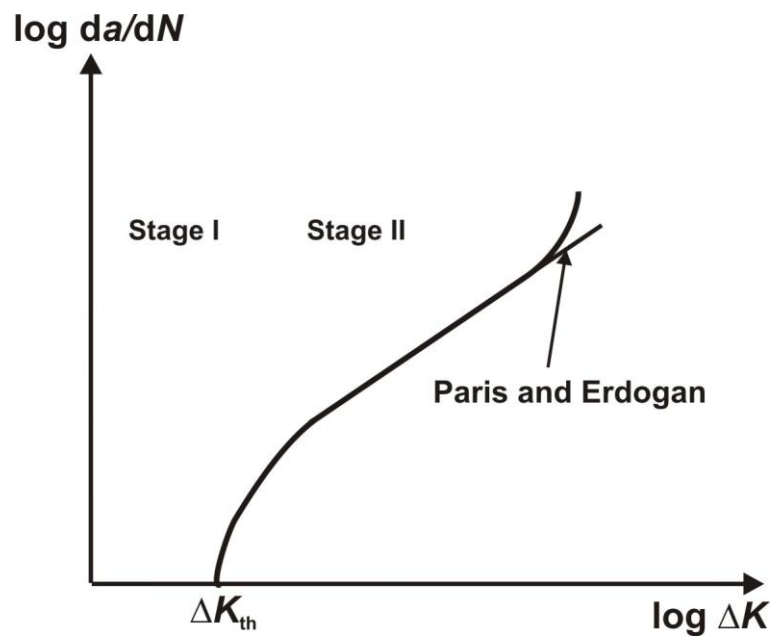


Fig. 2.20: A schematic illustration of fatigue crack growth behaviour.

The Paris law remains a very useful relationship because it covers the range of growth rates most useful to engineering structures and an extrapolation into the threshold regime gives a conservative estimate for the remaining life. This development was crucial to the adoption of defect-tolerance concepts and the implementation of a retirement-for-cause philosophy.

The lower growth rate region is termed the threshold regime, because growth rates drop off steeply and the crack becomes essentially non-propagating. This represents a change in mechanism from double shear continuum growth to single shear non-continuum growth. The fatigue threshold, ΔK_{th} , is an asymptotic value of ΔK at which da/dN approaches zero. In practice, most experimental data do not show a clear asymptote even at the lowest growth rates that can be examined. A more practical definition of ΔK_{th} is the value of the stress intensity factor range corresponding to a specific growth rate, chosen to be low enough so that crack growth will be negligible for all practical situations. For most materials an operational, though arbitrary, definition of ΔK_{th} is given as the value of ΔK , which corresponds to a fatigue crack growth rate of 10^{-8} mm/cycle [3]. According to ASTM E647, ΔK_{th} should be determined from a linear regression of $\log (da/dN) \sim \log \Delta K$ curve using a minimum of five data points of approximately equal spacing between growth rates of 10^{-7} and

10^{-8} mm/cycle. Mechanical parameters (load ratio, frequency) and material microstructure (grain size, precipitation, microstructure and stacking fault energy) strongly influence near threshold crack propagation. The spacing of the blocking microstructural features in front of the advancing crack governs the resistance to crack growth. Composite effects are observed when the spacing of one obstacle type differs from another. For instance, the precipitation effects on crack advance can override the grain size effect if the precipitates are not easily penetrable by the cracks. Similarly, reducing the stacking fault energy can accentuate the planarity of slip in a grain and hence restrict the cracks to grow along slip facets inducing significant crack deflection or crack path tortuosity.

2.2 Duplex stainless steel and 475°C embrittlement

2.2.1 Duplex stainless steel

Duplex stainless steels (DSS) are finding increased applications as structural materials in critical components of nuclear power plants, in chemical industries, oil and gas sectors, in paper and pulp industries, as pollution control equipment, transportation and other general engineering applications because of higher strength, superior resistance to stress corrosion cracking and better weldability [22-25,34-44]. This excellent combination of mechanical properties and corrosion resistance of DSS is the result of the presence of a balanced amount of ferrite and austenite in the microstructure [87]. Recent development of DSS occurs mainly in the area of alloying molybdenum, copper, nitrogen, etc. for further improving mechanical and corrosion properties [38-41]. As a result, this grade has a wide range of compositional variation. Cast DSS grades such as CF3, CF8, CF8M, predominantly used in nuclear power industries have ferrite content in the range of 9-15% (volume), whereas the ferrite content of wrought DSS such as SAF 2205, used in chemical tankers and line pipes is as high as 50% (volume). Table 2.3 gives a comparison of the compositions of cast and wrought DSS.

Table 2.3: Chemical composition of cast and wrought DSS grades, wt.%.

	Grades	C	Mn	P	S	Ni	Cr	Mo	N	Cu
Cast	CF3	0.030	0.60	0.003	0.002	8-12	17-21	<0.5	--	--
	CF8	0.057	0.62	0.003	0.002	8.23	19.94	0.21	--	--
	CF8M	0.074	1.21	0.032	1.140	9.59	18.67	2.73	--	--
Wrought	2205	0.030	2.00	0.030	0.020	4.5-6.5	22-23	3.0-3.5	0.15	--
	2507	0.030	1.20	0.035	0.020	6.0-8.0	24-26	3.0-5.0	0.24	0.5
	255	0.040	1.50	0.040	0.030	4.5-6.5	24-27	2.9-3.9	0.25	2.0

These compositions are approximate only and are intended for a comparison of cast and wrought DSS.

2.2.2 475°C embrittlement

DSS undergo embrittlement during heating in the temperature range of 280-500°C due to the decomposition of the highly alloyed ferritic phase to chromium rich phase α' and iron rich phase α [38,43-45,88-89]. This phenomenon is termed as 475°C embrittlement after the temperature at which the embrittlement rate is highest. The embrittlement significantly affects impact toughness, tensile ductility, fracture toughness and fatigue behaviour limiting the use of this steel to temperatures below 280°C [37-50].

Reidrich and Loib [90] reported embrittlement, caused by elevated temperature exposure of iron-chromium alloy system already in 1941. They conducted bend tests and observed that steels containing 19 to 23 at.% chromium had poor ductility after 1000 hours exposure at 500°C, but the ductility was not impaired when the samples were aged at 550°C. This indicated that the embrittlement is sensitive to temperature in a very narrow range. Fisher *et al.* [91] were the first to suggest the decomposition of the ferritic phase in a binary iron-chromium alloy to a chromium-rich phase (α') and an iron-rich phase (α), in the temperature range of 280-500°C. They observed fine spherical precipitates of diameter 200 Å in steel samples containing 28.5 at.% chromium and aged at 475°C for 1 to 3 years. The precipitates observed had a BCC structure containing about 80 at.% chromium and were nonmagnetic in nature. The lattice parameter of these precipitates was reported to be between that of iron and chromium. After the detection of precipitates caused by aging treatment and the resulting embrittlement, the focus of research shifted to identify the phase in iron-chromium binary alloy system in the temperature range of 280-500°C that cause the embrittlement. William *et al.* [92] are the first to propose explicitly, the existence of a

miscibility gap as the cause of precipitation of α' in the temperature range of 280-500°C in iron-chromium phase diagram. Figure 2.21 shows the phase diagram proposed by William *et al.* [92]. According to this phase diagram, 475°C embrittlement may be expected at temperatures below 516°C in the range of 12 to 92 at.% chromium in the iron-chromium binary alloy system. So this study was a confirmation of the earlier study by Reidrich and Loib on the redissolution of α' precipitates and also substantiated the maximum temperature for the $\alpha+\alpha'/\alpha$ phase boundary. Blackburn and Nutting [93] completely redissolved the α' after 24 hours of aging at 550°C. The neutron diffraction studies conducted by Vintaikin *et al.* [94] confirmed the clustering and decomposition of ferritic phase in the temperature range of 280-500°C.

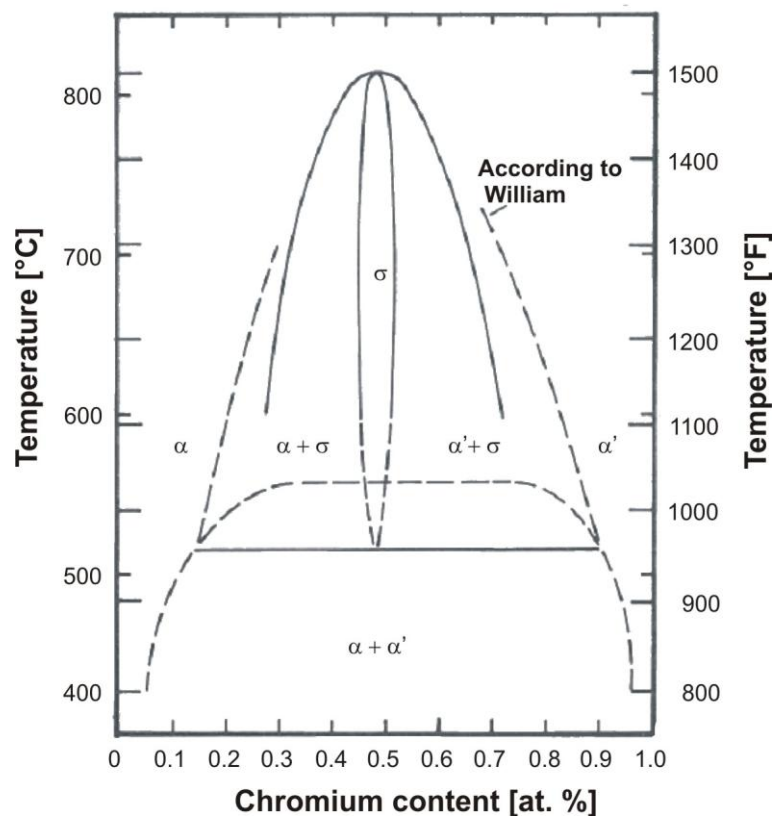


Fig. 2.21: Phase diagram of the iron-chromium system according to William *et al.* [92].

Some of the critical reviews on the theory of decomposition in metastable ferritic alloys were done by Cahn [95] and Hilliard [96]. These reviews discussed the thermodynamical distinction within the miscibility gap (a) for spinodal decomposition or (b)

nucleation and growth of α' . Spinodal decomposition refers to a reaction where two phases of the same crystal lattice type, but different compositions and properties, form due to the existence of a miscibility gap in the alloy system by means of uphill diffusion without nucleation [95]. Thermodynamically this is possible at concentration between the points where the second derivative of free energy with composition equals zero. This phase separation process occurs at a very fine scale (of the order of only a few nanometers) and the presence of the α' phase can only be detected through an atom probe field ion microscope [26]. Chandra *et al.* [27] tried to calculate the solubility of chromium in iron in the temperature range of 280-500°C and predicted the boundaries within the miscibility gap for spinodal decomposition, nucleation and growth. They studied the Mössbauer effect of 475°C embrittlement of a series of iron-chromium binary alloys by varying the chromium content and estimated the solubility of chromium in iron to be 12 at.% at 475°C. They predicted that only alloys with chromium content in excess of 13 at.% exhibit 475°C embrittlement. Another important observation was that alloys with chromium content 12 to 30 at.% decomposed via a nucleation and growth mechanism. Figure 2.22 shows the miscibility gap as proposed by William *et al.* [92] and the calculated chemical spinodal by the dashed line. The coherent spinodal line in the diagram is the corrected chemical spinodal taking into account the elastic strain energy due to 0.6% difference in the atomic size of iron and chromium.

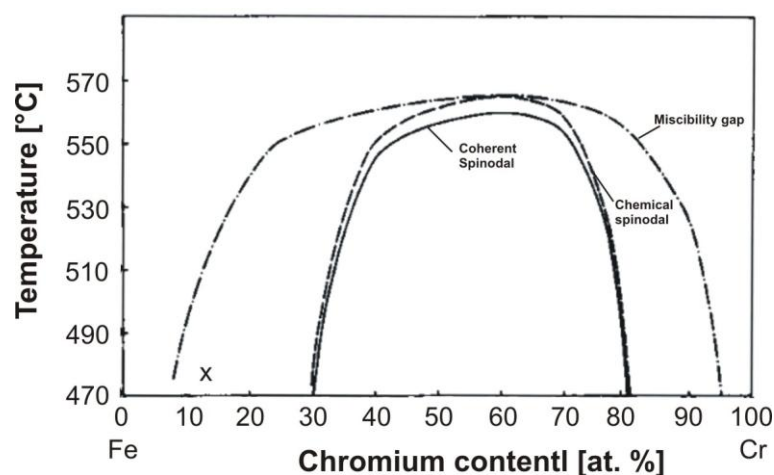


Fig. 2.22: Miscibility gap as proposed by William *et al.* [92] showing calculated chemical spinodal and calculated coherent spinodal, x, indicates the solubility limit at 475°C.

Grobner [26] conducted experiments on iron-chromium alloys with 14 and 18 at.% chromium content to establish the critical temperature range for 475°C embrittlement. Steel with 18 at.% chromium embrittled in the temperature range of 371-482°C in times as short as 2 hours, whereas steel with 14 at.% chromium showed embrittlement after much longer exposure times in the same temperature range. He calculated kinetics of α' precipitation assuming nucleation and growth mechanism, and the results confirmed the finding by Chandra *et al.* [27] that alloys with 12-30 at.% chromium decompose through nucleation and growth of α' . All the work cited above on the thermodynamics of decomposition concentrated on:

- the calculation of the miscibility gap in the iron-chromium phase diagram to establish the critical composition range (chromium content) and critical temperature range for the precipitation of α' ,
- determining the mechanism of formation of α' precipitate (spinodal decomposition or nucleation and growth or both) and relating the findings to composition and exposure temperature.

These studies were carried out mostly on the single-phase ferritic systems and it is evident that composition (mainly chromium content) of the ferrite and the exposure temperature are the key parameters that decides which mechanisms are involved in the formation of the α' phase. DSS have two major deviations from the conventional iron-chromium alloys:

- It has both ferrite and austenite in the microstructure and the ferrite content vary from 9 to 15 wt.% for cast DSS to 30 to 50 wt.% in wrought DSS.
- The ferrite in DSS contains additional alloying elements such as titanium, nickel, molybdenum, copper and nitrogen.

Chapter 3 Experimental techniques

This chapter describes the experimental techniques used in the present investigation. The material characterization techniques are described in section 3.1 and mechanical characterization techniques are described in section 3.2.

3.1 Material characterization

The material for this investigation is commercially pure DSS, DIN W Nr. 1.4462. The chemical composition is given in Table 3.1. The material was supplied in the form of a rod of 25 mm diameter. The as-received material condition was hot rolled solution annealed and water quenched. The grain sizes were distributed over a wide range with an average grain size of 10 μm and the volume fraction of austenite was 0.5.

Table 3.1: Chemical composition (wt.%) of the investigated steel.

C	Si	Mn	P	S	Cr	Mo	Ni	N
0.020	0.53	1.83	0.023	0.002	21.91	3.08	5.58	0.1871

3.1.1 Heat treatment

The grain size of the as received material was very small for obtaining discernable crystallographic data from the electropolished surface of the specimen from interrupted fatigue tests. For this purpose the grains were coarsened by a heat treatment cycle, which was carefully chosen to preclude precipitation of any undesirable phases. The specimens were heated very fast to 1250°C and kept at this temperature for 4 hours. Then the furnace temperature was reduced to 1050°C in 3 hours. Subsequently the specimens were quenched in water. This heat treatment condition is mentioned as annealed condition in the subsequent text. The TTT diagram for the start of 475°C embrittlement obtained from the supplier of the material is shown in Fig 3.1. The specimen were then heated very fast to 475°C and kept at this temperature for different intervals from 10 min, 20 min, 40 min, 1 hour, 2 hours, 3 hours, 5 hours, 10 hours, 50 hours, 100 hours, 200 hours and 300 hours followed by water

quenching. There was no further appreciable change observed in the tensile, impact and low cycle fatigue behaviour for 100, 200 and 300 hours of aging treatment. So it was considered that the decomposition in the ferritic phase is complete after 100 hours of aging treatment. As already mentioned above, in agreement with the present investigation it has been reported by Weng *et al.* [30] that for DSS with similar composition (SAF 2205) the precipitation of α' reaches saturation after about 64 hours of aging at 475°C. Aging at 475°C for 100 hours is referred to as aged condition in the subsequent chapters unless the time of aging is particularly mentioned.

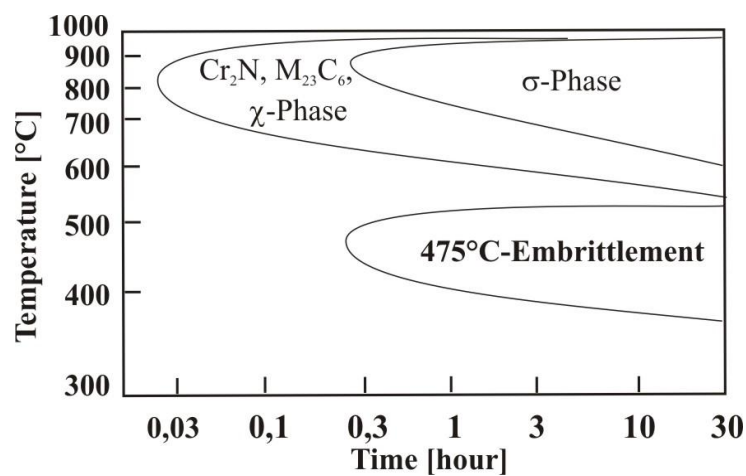


Fig. 3.1: TTT diagram of 1.4462 DSS according to supplier.

The composition of the solutions used for electropolishing and etching during the investigation are given in Table 3.2.

Table 3.2: Solutions used for electropolishing and etching in the investigation.

Type of microscopy	Type of treatment	Composition
Optical	Electrolytic etching	10 vol% oxalic acid 90 vol% distilled water
Optical	Colour metallography	100 ml stock solution B II 1 gm potassium bisulphite
SEM	Electropolishing	8 vol% perchloric acid (70%) 70 vol% ethanol 10 vol% diethylene glycol monobutyl ether 12 vol% distilled water
TEM	Twin jet polishing	10 vol% perchloric acid 90 vol% acetic acid

3.1.2 Electron microscopy

The scanning electron microscope in the present investigation was used for two purposes:

- Examination of fracture surfaces resulting from different mechanical tests. This imaging is conventionally done with a secondary electron detector.
- Obtaining crystallographic information from the sample surface and relating them to evolution of surface damage during fatigue testing by using electron back scattered diffraction (EBSD) technique and orientation imaging microscopy (OIM).

The following paragraph gives an overview of EBSD technique used for obtaining crystallographic information.

EBSD can give information about the crystal structure and orientation of the grains in a crystalline material. An electron beam irradiating a crystal is schematically shown in Fig. 3.2. The primary electrons are scattered in all directions, and part of them impinges on a given set of lattice planes $\{hkl\}$ at Bragg angle. The Bragg angle depends on the wavelength of the electrons. The relative change in wavelength due to inelastic scattering in an electron microscope is relatively small and therefore both elastically and inelastically scattered electrons may contribute to Bragg diffraction at approximately the same angle. The Bragg diffraction condition is given in Eq. 3.1.

$$n\lambda = 2d \sin \theta \quad (3.1)$$

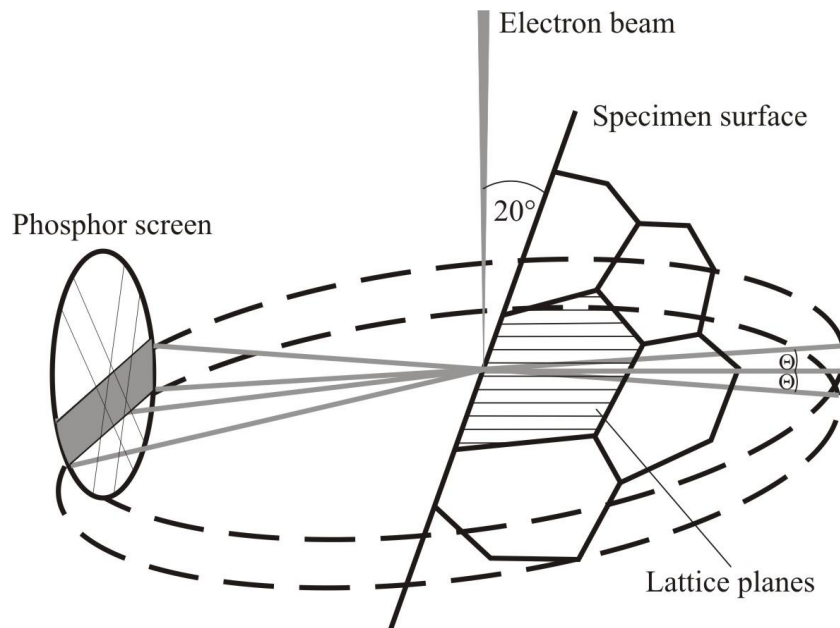


Fig. 3.2: Schematic diagram of the set up in SEM with phosphor screen to detect Kikuchi lines for determination of crystal orientation.

The specimen surface is tilted about 70° with respect to the electron beam in order to promote backscatter diffraction. The electron beam subsequently scans across the area of interest on the surface, and at each position the backscatter diffracted beam is recorded and analyzed. This allows for a fast mapping of the texture of polycrystalline materials, together with the phase identification from a limited number of pre-selected phases. Figure 3.3 shows a typical EBSD pattern generated inside the SEM on the phosphor screen. The distance between a pair of Kikuchi lines is related to the inter planar distance of the corresponding lattice planes and the angles between different pairs of Kikuchi lines represent the angular relationships in the crystal. The pattern therefore contains many important characteristics of the crystal and the orientation of the crystal can be determined from the position of the lines.

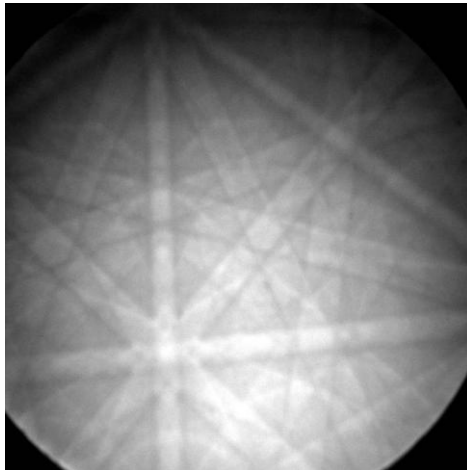


Fig. 3.3: A typical EBSD pattern generated inside the SEM.

The principle of EBSD has been implemented in the SEM for phase determination and orientation mapping. The most popular commercial names for the automation are orientation imaging microscopy (OIM) and automated crystal orientation mapping (ACOM). These software programmes have in-built libraries containing crystallographic information of different metals and alloys, and are equipped to perform mathematical calculations relating to crystallography. With the use of these packages crystallographic information such as misorientation between grains, grain boundary characters (random or CSL boundaries), information about grain shape, Schmid factors etc can be obtained.

3.2 Mechanical characterization

The tensile tests were performed with dog bone type cylindrical round specimens in accordance with ASTM E8M and the impact tests were performed with standard charpy V-notch type specimens.

3.2.1 Low cycle fatigue

Low cycle fatigue testing was carried out in an Instron 8862 servoelectric test system in laboratory air at room temperature. The shape, dimension and surface finish of the specimen for LCF test adhere to the specification ASTM E 606-92. A tolerance of ± 0.1 mm was

allowed in linear dimension and a surface roughness below $0.2 \mu\text{m}$ was maintained. The drawing of the specimen used for this test is given in Fig. 3.4.

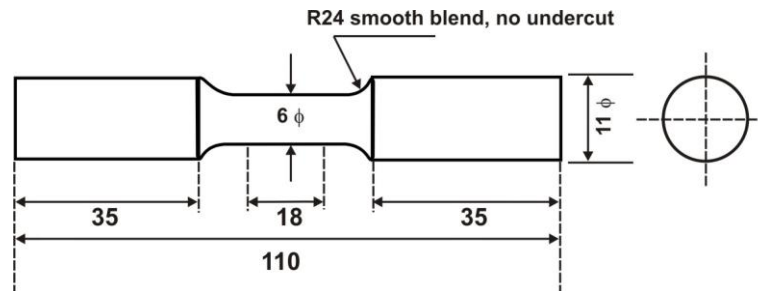


Fig. 3.4: Drawing of LCF specimen (Dimensions are in mm).

The tests were performed under fully reversible total strain control with continuous triangular waveforms at a constant frequency of 0.5 Hz. Knife-edge extensometer with a gauge length of 12.5 mm was used for strain measurement. The center of the gauge portion of the specimen was marked and the knife-edges of the extensometer were placed at equidistance from the center. A specimen in the aged condition cycled at $\Delta\varepsilon/2 = 3.0 \times 10^{-3}$ did not fail even after 9.5×10^4 cycles. So the values of $\Delta\varepsilon/2$ employed in the present investigation were 4.0×10^{-3} , 6.0×10^{-3} , 8.0×10^{-3} and 1.0×10^{-2} in annealed and aged conditions. The fatigue life (N_f) corresponds to the cycle number with 20% reduction in peak tensile stress.

3.2.2 Fatigue crack initiation

The fatigue crack initiation was conducted with fully reversed stress-controlled fatigue tests at a constant frequency of 1.0 Hz. The different stress amplitudes employed were $\Delta\sigma/2 = 400$ MPa, 500 MPa and 600 MPa. The drawing of the specimen used for this test is given in Fig. 3.5.

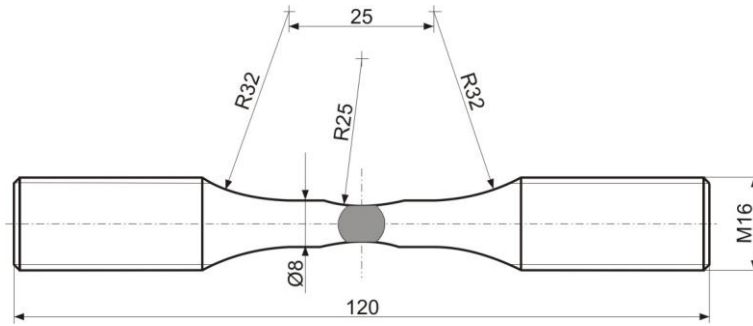


Fig. 3.5: Drawing of specimen used for fatigue crack initiation study (Dimensions are in mm).

The specimen geometry has shallow notches at opposite sides of the center of the gauge length to focus the crack initiation studies in this region. The cross sectional area of the gauge length region is calculated using Eq. 3.1.

$$A = \frac{D^2}{4} \left[\pi - 2 \cdot \arccos \frac{d}{D} + \sin \left(2 \cdot \arccos \frac{d}{D} \right) \right] \quad (3.1)$$

d and D are the minimum and maximum diameter at the notch respectively.

The specimen was electropolished. The fatigue tests are interrupted and the crack initiation sites are observed in the SEM. EBSD scans were also intermittently performed in the areas of crack initiation to extract the crystallographic information on the grains containing the cracks. A microindentation is made in the center of the shallow notch to identify the position of a grain containing crack, which is observed on the interruption of the fatigue test. Figure 3.6 shows the microindentation at the center of the shallow notch.

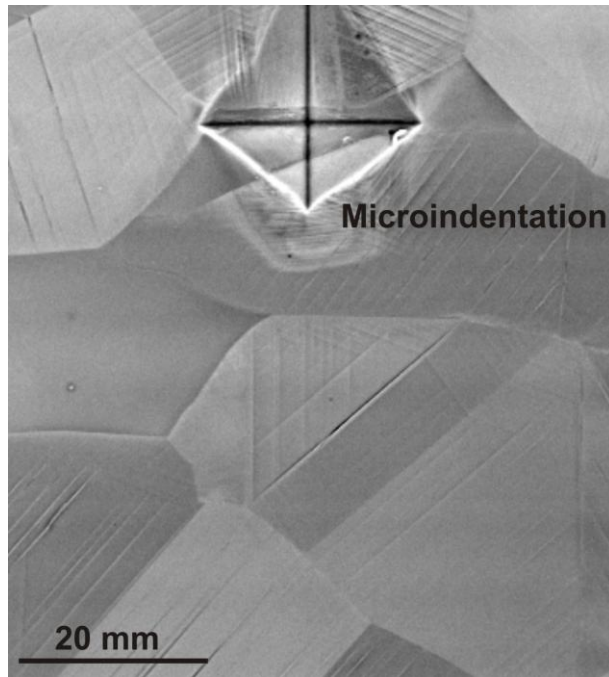


Fig. 3.6: Microindentation at the center of the shallow notch.

Chapter 4 Results and discussion

In this chapter the results obtained in the present investigation are introduced, discussed and compared with the results obtained by other researchers who investigated similar aspects of the fatigue behaviour of DSS. The chapter is divided into four sections. The results and discussion on the microstructural characterization of the investigated grade of DSS in different heat treatment conditions using light and electron microscopy are presented in section 4.1. The effect of 475°C aging treatment on tensile and impact behaviour is described in section 4.2. The results of the investigations on the effect of 475°C aging treatment on low-cycle fatigue behaviour are shown in section 4.3. The results of the studies related to fatigue crack initiation and growth of short cracks are presented in section 4.4.

4.1 Microstructural characterization

This section has three subsections. Subsection 4.1.1 introduces the results of optical microscopic examinations. The scanning electron microscopic examinations are discussed in subsection 4.1.2. Subsection 4.1.3 shows the results obtained from transmission electron microscopic examination.

4.1.1 Optical microscopy

The microstructure consists of island-like austenitic grains in a more or less continuous matrix of ferrite. Figure 4.1 shows the microstructure of DSS in the annealed condition in rolling and transverse direction. The bright-etched grains in the micrograph are austenite and the dark etched matrix is ferrite. The average grain sizes are 35 μm and 50 μm for austenite and ferrite, respectively. The austenitic grains are elongated in the rolling direction and a large number of annealing twins are observed in the micrograph.

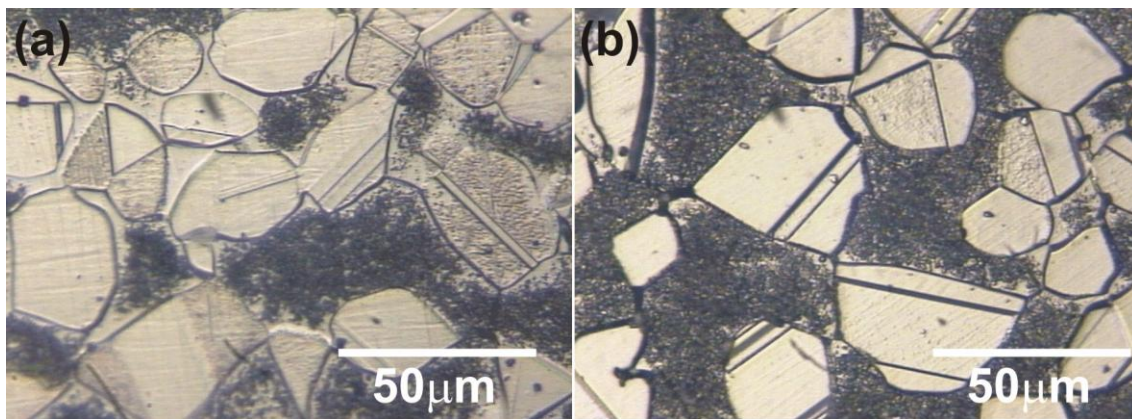


Fig. 4.1: Microstructure of the DSS studied: (a) rolling and (b) transverse direction.

There was no visible change observed in the microstructure under optical microscope after aging treatment at 475°C for 100 hours with electrolytic etching and colour etching. Nelson *et al.* [97] used a three-step etching technique ((i) glyceric acid solution consisting of 30 parts hydrochloric acid, 20 parts glycerin and 10 parts nitric acid; (ii) 10 % oxalic acid; (iii) boiling Murakami's reagent (10 gm permanganate and 10 gm potassium hydroxide in 100 ml water)) to reveal the microstructure of weld in a DSS and to deposit an interference film on various phases for colour metallography. They observed different colours for chromium-segregated regions in the weld and heat affected zone (HAZ) in ferritic grains. However, such a treatment in case of the DSS grade used in the present investigation did not reveal any interference film. The temperature in the weld and HAZ regions are usually higher than 475°C and can cause several other precipitation reactions. That can be a possible reason for not observing an interference film for chromium segregation in the present grade of DSS with the above-mentioned three-step etching treatment. There was no change observed in the average grain size of ferrite and austenite after 475°C aging treatment. The constancy in microstructural parameters was observed under optical microscope even after 200 and 300 hours of aging treatment at 475°C.

4.1.2 Scanning electron microscopy

The microstructure of the electrolytically polished DSS observed in the rolling direction under SEM in secondary electron (SE) mode is shown in Fig. 4.2. The austenitic grains are elongated in the rolling direction and there appears to be surface topography.

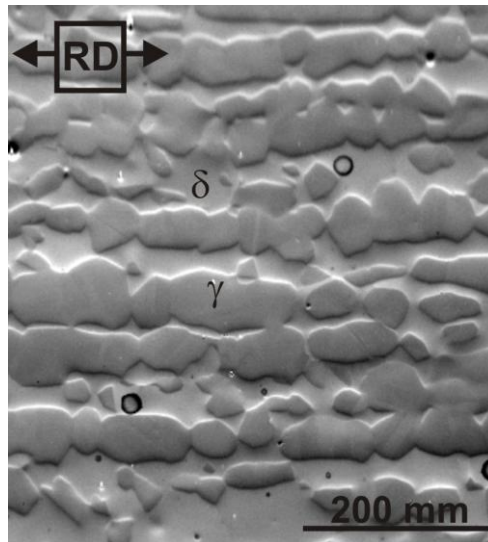


Fig. 4.2: Microstructure of the DSS studied observed under SEM.

From a crystallographic point of view the sample has two directions, the rolling direction and the transverse direction. The rolling direction of the sample is identical with the longitudinal axis of the reference co-ordinate system as shown in Fig. 4.3.

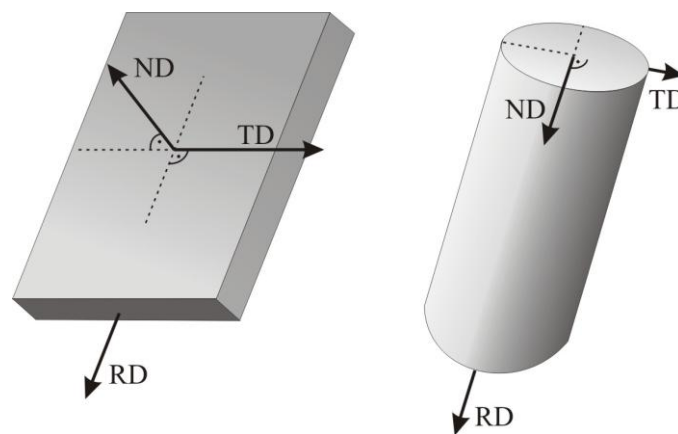


Fig. 4.3: The EBSD-OIM reference co-ordinate system and sample co-ordinate system.

The fatigue crack initiation on the surface and the growth of short cracks in DSS is strongly dependent on microstructural parameters such as grain size, grain shape and orientation relationship between phases [39-40]. In order to obtain the local orientation relationship between grains, texture was assessed from the EBSD scans with the help of OIM software.

The characteristic nature of the texture development in FCC and BCC metals is well understood. The predominant rolling texture in BCC metals is $\{001\}\langle 110\rangle$ along with other texture component such as $\{112\}\langle 110\rangle$ and $\{111\}\langle 112\rangle$. The main ideal orientations observed in FCC metals are Cube $\{100\}\langle 001\rangle$, Goss (G) $\{011\}\langle 100\rangle$, Brass (B) $\{011\}\langle 211\rangle$, S $\{123\}\langle 634\rangle$, and Copper (C) $\{112\}\langle 111\rangle$.

Three pole figures for the (111), (110) and (100) reflection for austenite and ferrite phases were determined using EBSD-OIM and are shown in Fig. 4.4.

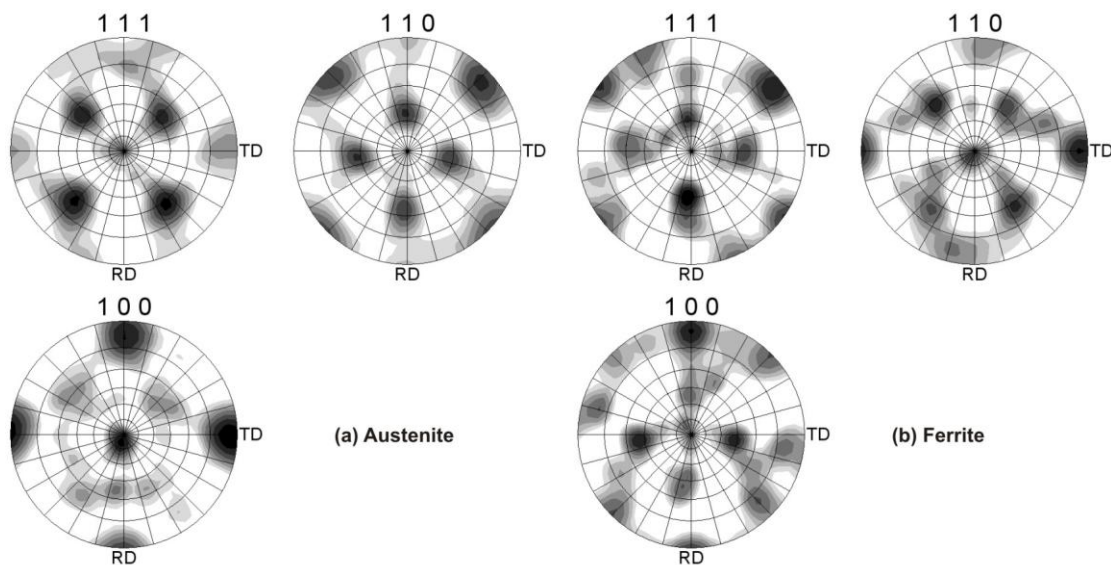


Fig. 4.4: Pole figure for the austenite and ferrite phase showing presence of strong texture in both the phases.

Experimental pole figure data collected were used to calculate orientation distribution function (ODF) plots and are presented as plots of constant ϕ_2 -section for austenite phase and ϕ_1 -section for ferrite phase with iso-intensity contours in the Euler-space defined by three

Bunge's Euler angles ϕ_1 , Φ and ϕ_2 . ODFs for the two phases are shown in Fig. 4.5 and Fig. 4.6.

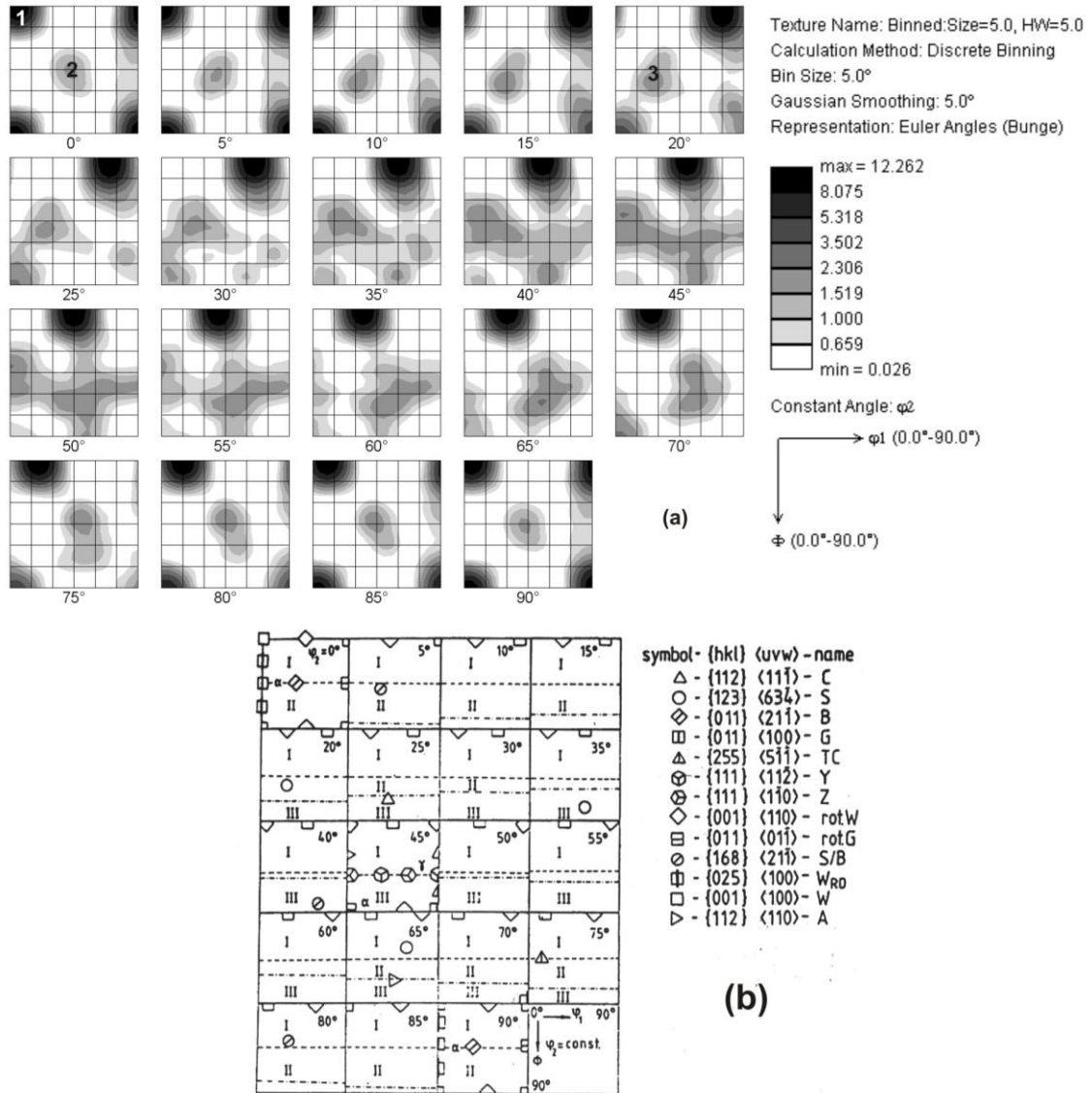


Fig. 4.5: (a) Constant ϕ_2 ODF sections showing texture in the austenite phase, the texture components are indicated by numbers: 1: $\{001\}\langle 100\rangle$ and 2: $\{011\}\langle 211\rangle$ in section $\phi_2 = 0^\circ$, 3: $\{123\}\langle 634\rangle$ in section $\phi_2 = 20^\circ$ in the figure; (b) schematic representation of texture components.

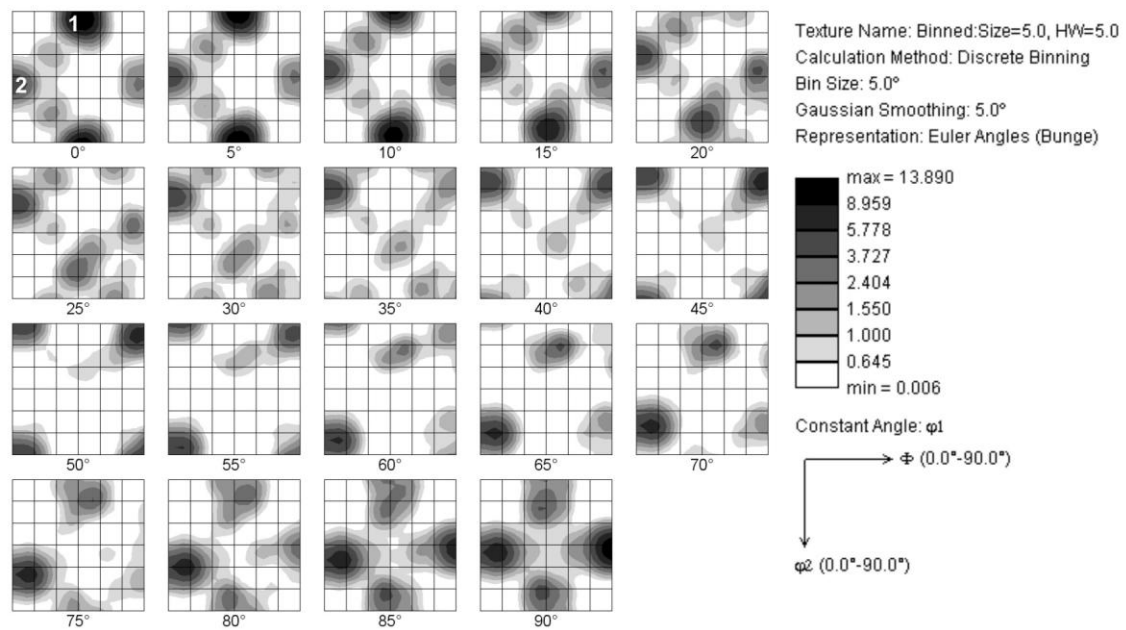


Fig. 4.6: Constant ϕ_1 ODF sections showing texture in ferrite phase. The texture components are indicated by numbers: 1: $\{011\}\langle 100\rangle$ and 2: $\{001\}\langle 110\rangle$ in section $\phi_1 = 0^\circ$ in the figure.

The austenite texture is characterized by a very strong $\{001\}\langle 100\rangle$ Cube texture component along with $\{011\}\langle 211\rangle$ Brass (B) and $\{123\}\langle 634\rangle$ S texture components in the material along rolling direction as shown in Fig. 4.5. The intensity of the cube component is almost four times stronger than the other two texture components. On the other hand, the ferritic phase texture is characterized by very strong $\{011\}\langle 100\rangle$ Goss (G) and $\{001\}\langle 110\rangle$ rotated cube texture components as shown in Fig. 4.6.

It is well established that the phase transformation mechanism is strictly crystallographic, hence the texture components of the ferrite should have a crystallographic orientation relationship with the austenite phase. In fact, the ferrite phase orientation is related to the austenite phase orientation by the Kurdjumov-Sachs (K-S) orientation relationship. The transformation textures of various austenite texture components are shown in the Table 4.1 [98]. The major ferrite texture components observed in the present study are found to follow K-S orientation relationship with parent austenite phase orientations. According to the K-S orientation relationship, the major $\{011\}\langle 100\rangle$ G orientation of ferrite is related to the $\{001\}\langle 100\rangle$ cube orientation of austenite and the $\{001\}\langle 110\rangle$ orientations of ferrite is related to the $\{110\}\langle 112\rangle$ orientations of the austenite [98].

Table 4.1: The transformation textures of various austenite texture components [98].

FCC orientation	BCC orientations
{100}<001>	{100}<110>
	{110}<001>
	{110}<110>
{110}<112>	{332}<113>
	{111}<112>
	{001}<110>
{112}<111>	{113}<110>
	{112}<110>
	{201}<102>
	{110}<110>
{123}<634>	{113}<110>
	{332}<113>
	{110}<110>

4.1.3 Transmission electron microscopy

The TEM examinations on samples were made in annealed and aged condition. In the annealed condition annealing twins and stacking fault regions were observed in the austenitic grains. Some stacking fault regions in the austenitic grain are shown in Fig. 4.7.

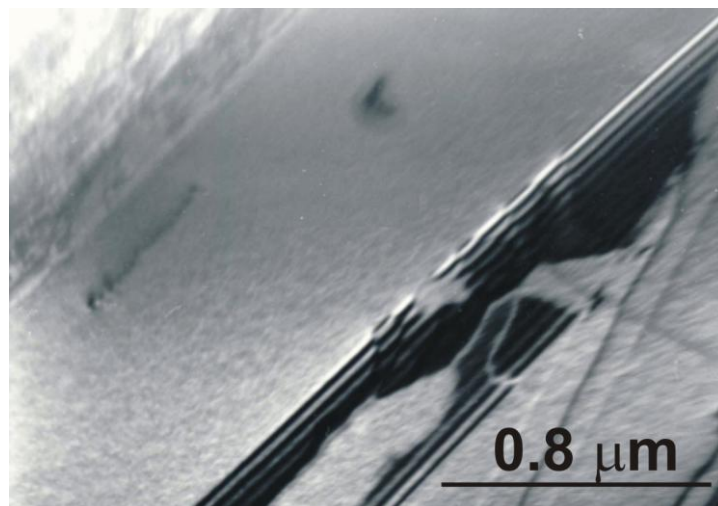
**Fig. 4.7:** Fault regions observed in the austenitic grain.

Figure 4.8 shows needle like precipitates observed in the ferritic grain of the DSS studied embrittled at 475°C for 100 hours. These needles are observed throughout the grain body. The average length of these needles was approximately 100 nm.

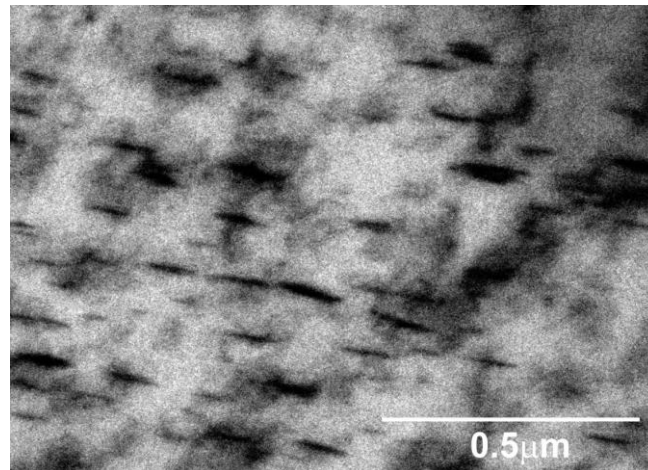


Fig. 4.8: Needle like precipitates observed in the ferritic phase after aging treatment at 475°C for 100 hours.

Figure 4.9a shows an array of precipitates in the same grain observed in another diffraction condition. The magnified image of this area is shown in Fig. 4.9b. A detailed analysis of the nature and characteristics of this precipitation reaction was not aimed at within the scope of the present investigation. However, upon subsequent TEM examinations of impact and LCF tested samples at higher values of strain amplitude ($\Delta\varepsilon/2 = 8.0 \times 10^{-3}$), it was observed that these precipitates significantly affect the impact toughness and cyclic hardening/softening behaviour in the ferritic phase of aged DSS. For this purpose a detailed discussion on the precipitation behaviour in the ferritic phase as a result of aging treatment at 475°C is presented in Section 5.1.

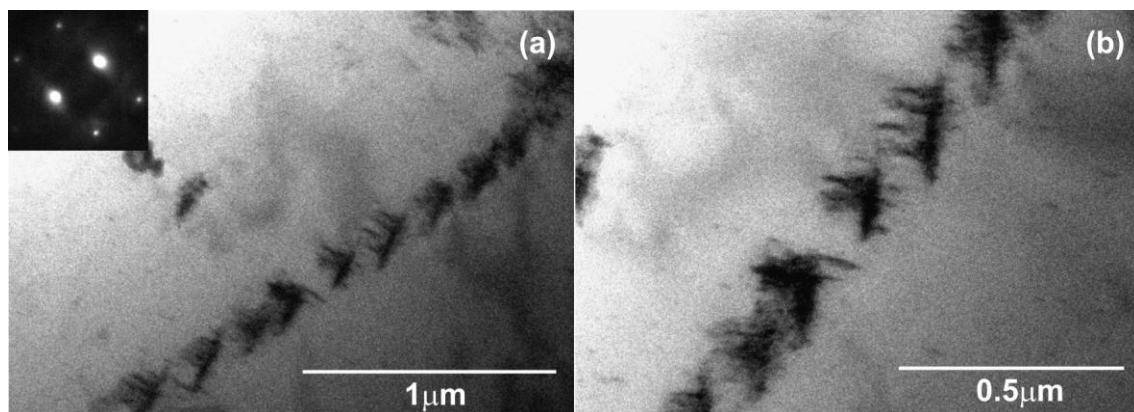


Fig. 4.9: (a) Same grain as in Fig. 4.8 observed in $g = (0\bar{1}\bar{1})$ diffraction condition; (b) high magnification micrograph of the precipitates.

When the same grain was viewed in the $[351]$ beam direction diffused scattering was observed in the diffraction pattern, as shown in Fig. 4.10. This kind of diffused scattering is indicative of short range ordering [99].

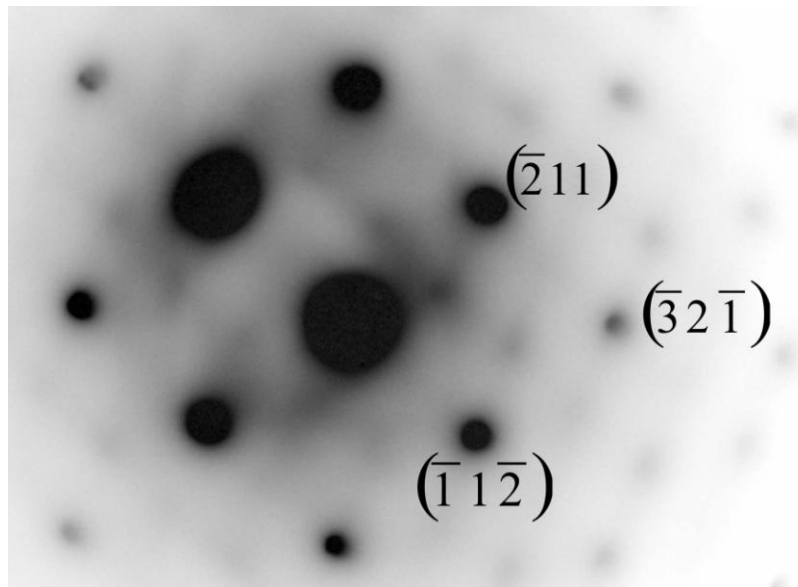


Fig. 4.10: Diffused scattering observed in the same grain shown in Fig. 4.8, zone axis = $[351]$.

4.2 Effect of aging treatment on tensile and impact behaviour

The aging treatment at 475°C affects the tensile and impact behaviour of DSS. This section has two subsections. The effect of 475°C embrittlement on tensile behaviour is described in subsection 4.2.1 and the impact behaviour is shown and discussed in subsection 4.2.2.

4.2.1 Tensile behaviour

The engineering stress-strain curves of the DSS studied in the annealed and aged condition are shown in Fig. 4.11. The measured values of yield strength, tensile strength, tensile ductility in the annealed and aged condition are given in Table 4.2. The yield strength and tensile strength of the steel increase by 28.5% and 27.5% respectively. The increase in tensile strength parameters as a result of embrittlement is commonly observed. However, the tensile

ductility decreased slightly as a result of the aging treatment. This means the loss of ductility is very marginal.

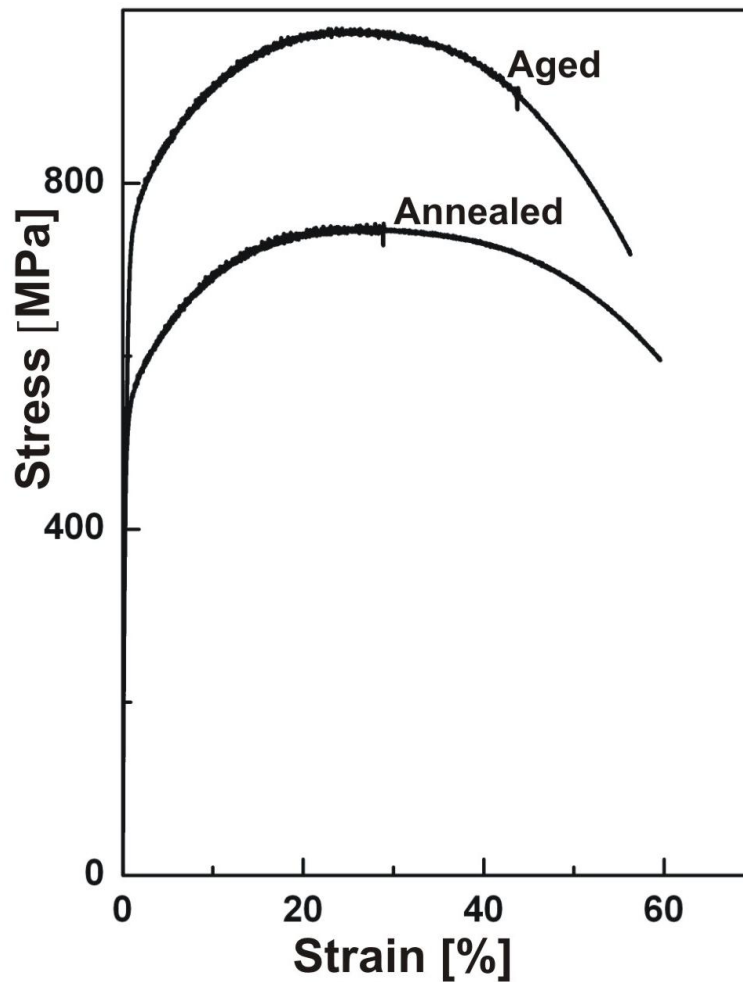


Fig. 4.11: Engineering stress-strain curve in the annealed and aged condition.

Table 4.2: Tensile test results in the annealed and aged condition.

	$\sigma_{ys(0.2\%)}$, MPa	σ_{uts} , MPa	ε_f (%)
Annealed	525	767	60
Aged	675	978	56

The fractographs of tensile tested samples in the annealed and aged condition are shown in Fig 4.12. Dimples were observed in the annealed condition. In the aged conditions dimples as well as many regions of secondary cracks were observed.

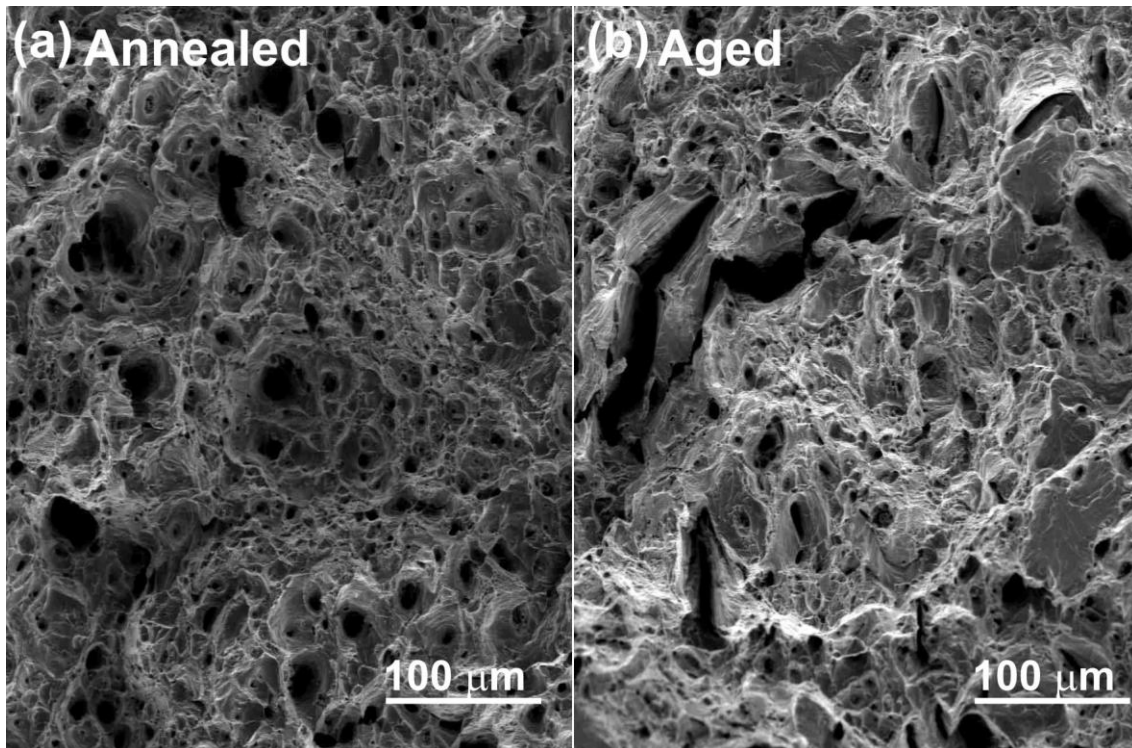


Fig. 4.12: Fractographs of tensile tested samples in the annealed and aged condition.

The engineering stress-strain curves obtained at room temperature and 475°C are shown in Fig. 4.13. The measured values of yield strength, tensile strength and tensile ductility are listed in Table 4.3.

Table 4.3: Tensile test results at room temperature and 475°C.

	$\sigma_{ys(0.2\%)}$, MPa	σ_{uts} , MPa	ϵ_t (%)
RT	519	767	43
475°C	325	643	23

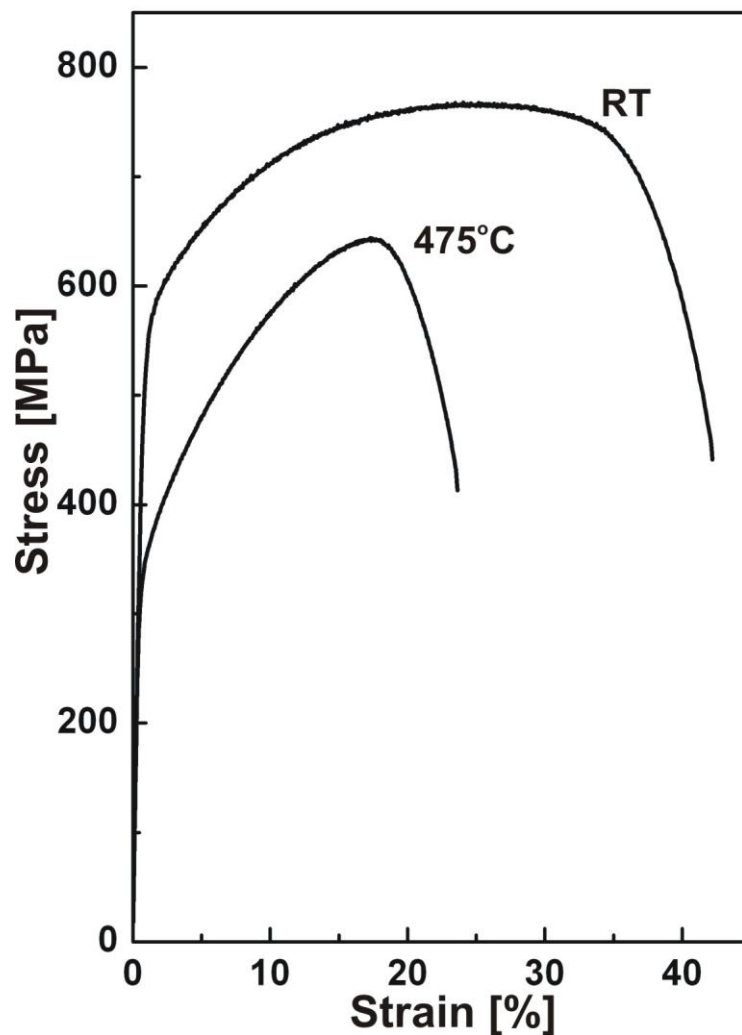


Fig. 4.13: Engineering stress-strain curve at RT and 475°C.

The structural incompatibility between the ferritic and austenitic phase modify the tensile behaviour [100]. With respect to tensile strength ferrite is usually stronger than austenite for the same interstitial content. However, the solubility of carbon or nitrogen in austenite is much higher compared to ferrite [101]. In DSS nitrogen gets preferentially partitioned in such a way that austenite becomes stronger than ferrite [102]. It was reported that in super DSS grades the amount of nitrogen dissolved in austenite is as high as 0.45 wt.% when the average nitrogen content is 0.27 wt.% and despite higher strength due to preferential nitrogen partitioning more plastic deformation occurred in austenite compared to ferrite as compressive residual stress build up in the ferritic phase during cooling. Strength is also grain-size dependent. The grain-size in a DSS is usually smaller than that of ferrite and

austenite of corresponding chemical composition. This is explained by mutual hindering of growth of the ferrite and austenite grains. If the effect of grain size and partitioning of interstitials is compensated, then the strength of DSS is controlled by the stronger ferritic phase. Toughness of DSS is very high due to the presence of austenite in the matrix. Austenite retards the cleavage fracture of ferrite. However, toughness is reported to be very sensitive to the precipitation of secondary phases.

Zielinski *et al.* [103] studied the evolution of dislocation structure in a solution annealed DSS by in situ TEM straining experiments and reported that the evolution of dislocation structure during straining is dependent on the orientation relationship between the two phases. In the case of special orientation relationships, the slip markings in the ferrite, produced by the dislocations emitted from the boundary, indicate the compatibility of easy slip systems in the two phases, which favours a strong localization of strain. In the case of random orientation relationships, the incompatibility of the easy slip systems in austenite and ferrite results in cross slip of the dislocations emitted from the boundary into the ferrite grains leading to multiplication and the formation of dislocation loops and debris. They attributed the high flow stress of DSS to the particular slip transfer mechanism related to the random orientation relationships between the austenite and ferrite. Bugat *et al.* [104] performed in situ tensile tests on a DSS aged at 400°C for 700 hours to characterize strain fields and monitor the sites of damage nucleation. Damage was found to preferentially initiate in areas, where the common slip system of the bicrystal has a low Schmid factor. Hilders *et al.* [105] studied the effect of 475°C embrittlement on fractal behaviour and tensile properties of DSS. In agreement with the present observation they also observed dimple-type fracture mode for small aging times and transgranular as well as dimple rupture for 24, 40, and 120 hours of aging. Furthermore, they observed a decrease in fractal dimension and the true fracture strain with increase in time of aging. Girones *et al.* [106] studied the dynamic strain aging effects on super DSS at temperatures ranging from 275° to 475°C. They reported that the activation energy for serrated flow, which is used as a parameter to identify the mechanism of dynamic strain aging, is too high for interstitial solutes and too low for substitutional ones to migrate to mobile dislocations to pin them through bulk diffusion both in austenite and ferrite.

4.2.2 Impact behaviour

Kinetics of 475°C embrittlement has been determined through indirect observations such as changes in certain mechanical properties like hardness [107] or saturation of certain microscopic features [30]. Kinetics of precipitation plays a very important role for some of the critical engineering components particularly in nuclear power plants. So majority of investigations on kinetics of 475°C embrittlement in DSS are reported from laboratories working on materials used in nuclear power plants [88-89, 108]. These investigations are mostly reported on CF3, CF8 and CF8M cast grades of DSS.

Figure 4.14 shows the variation of room temperature impact energy as a function of time of aging. The change in impact energy for the presently investigated grade of DSS is found to be fitting into a sigmoidal shape when plotted on a semi-log scale with time of aging at 475°C. The value of 8 Joule was obtained for 100, 200 and 300 hours of aging. So the embrittlement reaches saturation in 100 hours.

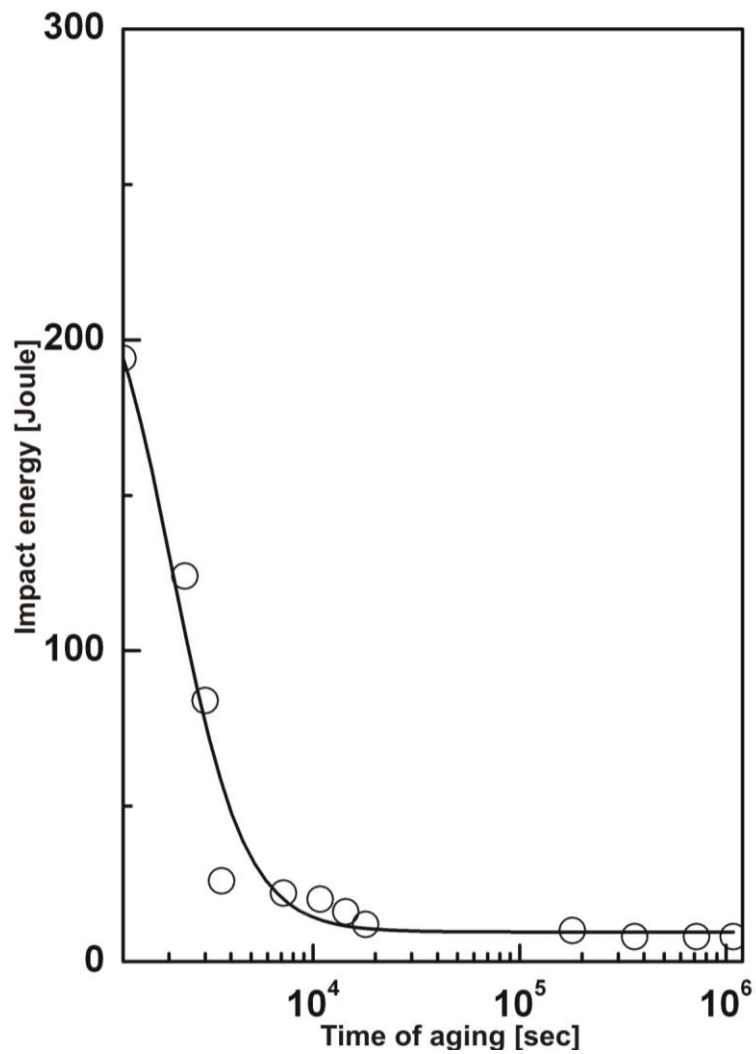


Fig. 4.14: Variation of impact energy with time of aging at 475°C.

Figure 4.15 shows the fracture surfaces of impact-tested samples in the annealed and aged conditions. The brittle appearance of the fracture surface in the aged condition is indicative of the drastic drop in impact energy absorption values.

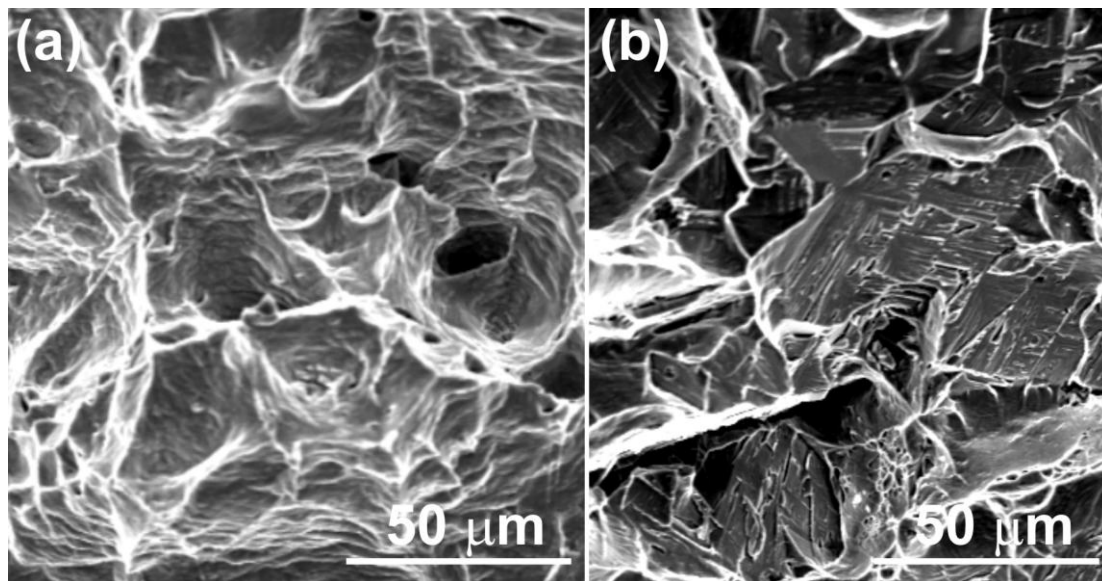


Fig. 4.15: Fractographs of impact tested samples (a) in the annealed and (b) aged condition.

Figure 4.16 shows TEM micrographs of foils taken from impact-tested samples in the annealed and aged condition. In the annealed condition deformation twins were observed in majority of the ferritic grains. The twinning in ferrite at high strain rate deformation is a common feature due to the absence of close packed planes. However, in the impact-tested sample in the aged condition twins were not observed. The precipitates that were observed in the ferritic phase for the aged DSS (Fig. 4.9) were also observed after impact testing. This means these precipitates were responsible for blocking the twinning in ferritic phase leading to a drastic drop in impact toughness.

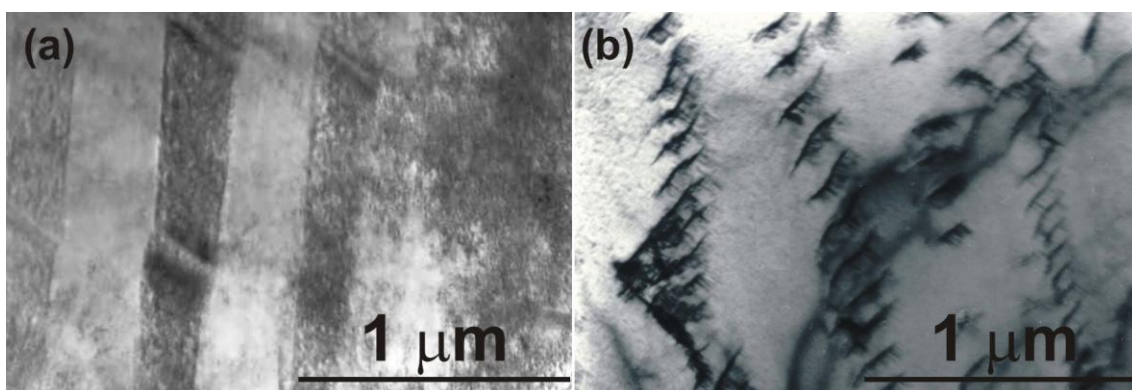


Fig. 4.16: TEM bright field (BF) image of impact tested samples (a) in the annealed and (b) aged condition.

Miller *et al.* [107] compared the rate of decomposition of the ferrite in iron-45 wt.% chromium, iron-45 wt.% chromium-5 wt.% nickel alloys and two CF3 grades of DSS during long-term aging at 400°C. The addition of nickel to the binary iron-chromium alloy was found to accelerate the kinetics of decomposition and significantly increased the hardness of the alloy. Although the hardness data from the ternary alloys are similar to those of the ferritic phase in the DSS, significant differences in the scale and composition amplitudes of α and α' phases were observed. The extent of phase separation was investigated by determining the difference in the composition amplitudes of α and α' phases as a function of aging time at 400°C. It is evident that the kinetics of precipitation plays an important role in the deterioration of mechanical properties. As shown by Miller *et al.* [107] the composition plays a key role in determining the kinetics of precipitation. When in one hand there is a constant effort to improve the mechanical properties by alloying DSS further with copper, nitrogen etc, effect of these alloying elements on α' precipitation is a subject of extensive further research.

The investigations reported on deterioration in impact energy were studied by looking into the fracture surface of DSS after 475°C embrittlement. Devillers-Guerville *et al.* [109] showed that the micromechanism of impact fracture at room temperature of a cast grade of DSS containing about 20 wt.% ferrite and embrittled at 400°C are: (i) nucleation of cleavage cracks grouped in millimetric clusters in the ferritic phase; (ii) growth of the cavities by the plastic deformation of the austenitic phase; and (iii) coalescence of the cavities to form a macroscopic crack. They observed no strain rate effect on the embrittled material when tested at room temperature. Druce *et al.* [110] studied the effect of notch depth, notch acuity and side grooving on the impact fracture behaviour of a cast DSS containing 25 wt.% ferrite in the temperature range of -200°C to +300°C. Increasing specimen constraint was found to have a marked influence on fracture mode, the temperature for the onset of low-to-high fracture energy transition, and the fracture energy per unit ligament area associated with fracture at elevated temperature. On the basis of these test data an optimum specimen geometry was developed for monitoring the effect of 475°C embrittlement on toughness and determining embrittlement kinetics.

4.3 Effect of aging treatment on the low cycle fatigue behaviour

This section is divided into four subsections. The influence of 475°C on the cyclic hardening/softening behaviour is described in subsection 4.3.1. The cyclic stress-strain behaviour in the annealed and aged conditions is discussed in subsection 4.3.2. The effect of aging treatment at 475°C on cyclic life is described in subsection 4.3.3. Electron microscopic examinations of LCF tested samples are discussed in subsection 4.3.4.

4.3.1 Cyclic hardening/softening behaviour

The cyclic hardening/softening behaviour was observed to be different with respect to the imposed values of total strain amplitude as well as the heat treatment conditions. The plastic strain amplitude ($\Delta\varepsilon_{pl}/2$) and the stress amplitude σ_s corresponding to saturation or mid life for tests conducted at different values of total strain amplitude $\Delta\varepsilon/2$ are listed in Table 4.4.

Table 4.4: ($\Delta\varepsilon_{pl}/2$)_s and σ_s values calculated from the cyclic deformation tests.

Material condition	$\Delta\varepsilon/2$	($\Delta\varepsilon_{pl}/2$) _s (saturation or half life)	σ_s , MPa
Annealed	4.0×10^{-3}	1.3×10^{-3}	507
	6.0×10^{-3}	3.2×10^{-3}	544
	8.0×10^{-3}	4.8×10^{-3}	569
	1.0×10^{-2}	6.6×10^{-3}	610
Aged	4.0×10^{-3}	1.2×10^{-3}	542
	6.0×10^{-3}	2.4×10^{-3}	675
	8.0×10^{-3}	3.7×10^{-3}	778
	1.0×10^{-2}	5.2×10^{-3}	811

The cyclic deformation curves at different values of total strain amplitude for the DSS studied in the annealed and aged condition are shown in Fig. 4.17.

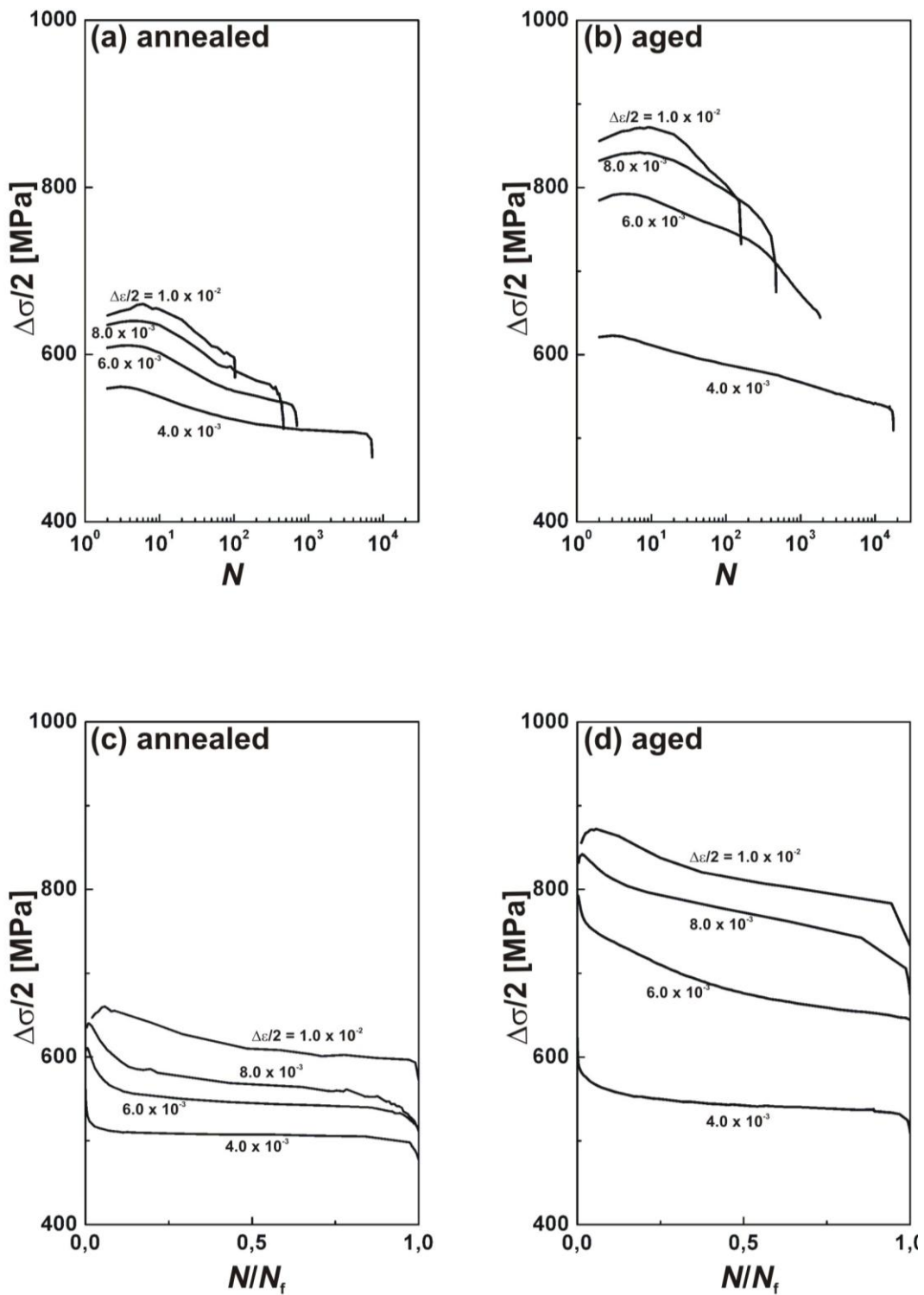


Fig. 4.17: Cyclic deformation curves of constant total strain amplitude controlled tests for the annealed and the aged condition as a representation of the stress amplitude vs number of cycles in a logarithmic scale (Fig. 4.17a and Fig. 4.17b) and the stress amplitude vs the life fraction N/N_f (Fig. 4.17c and Fig. 4.17d).

The following observations can be made from a comparison between the cyclic hardening/softening behaviour of DSS in the annealed condition at different values of total strain amplitude:

- For all values of total strain amplitude, initial hardening was observed for the first few cycles.
- The cyclic hardening was followed by immediate gradual softening for all values of total strain amplitudes except $\Delta\varepsilon/2 = 1.0 \times 10^{-2}$ where a rapid softening was observed.
- At $\Delta\varepsilon/2 = 4.0 \times 10^{-3}$ pronounced cyclic saturation was observed prior to the final inhomogeneous deformation. The period of cyclic saturation decreases with increase in strain amplitude. For the values of strain amplitude $\Delta\varepsilon/2 = 8.0 \times 10^{-3}$ and 1.0×10^{-2} cyclic saturation was not observed like lower values of $\Delta\varepsilon/2$.

The following observations can be made from a comparison between the cyclic hardening/softening behaviour of DSS in the aged condition at different values of total strain amplitude:

- For all values of strain amplitude initial hardening was observed for the first few cycles.
- The cyclic hardening was followed by immediate cyclic softening for all values of total strain amplitude. At lower values of $\Delta\varepsilon/2$ the softening was observed to be gradual. However, rapid cyclic softening was observed with increase in the values of total strain amplitude.
- Cyclic saturation was not observed for any value of total strain amplitude employed.

A comparison of cyclic hardening/softening behaviour of the DSS studied in annealed and aged condition leads to the following observations:

- No change was observed in the initial cyclic hardening behaviour for all values of the employed total strain amplitude in annealed and aged condition.
- At $\Delta\varepsilon/2 = 4.0 \times 10^{-3}$ cyclic saturation was not observed in the aged condition whereas the annealed material shows a pronounced plateau. The absence of cyclic saturation in the case of aged DSS is an indication of continued microstructural activities.

- For $\Delta\varepsilon/2$ values of 4.0×10^{-3} and 6.0×10^{-3} higher fatigue resistances is observed in the aged condition.
- At $\Delta\varepsilon/2$ values of 8.0×10^{-3} and 1.0×10^{-2} the fatigue resistance of the material drops significantly in the aged condition compared to the solely annealed condition.

For a clear portray of the effect of strain amplitude and aging treatment on cyclic hardening/softening behaviour, the stress amplitude normalized by the yield strength values for annealed and aged conditions was plotted versus the number of cycles in Fig. 4.18.

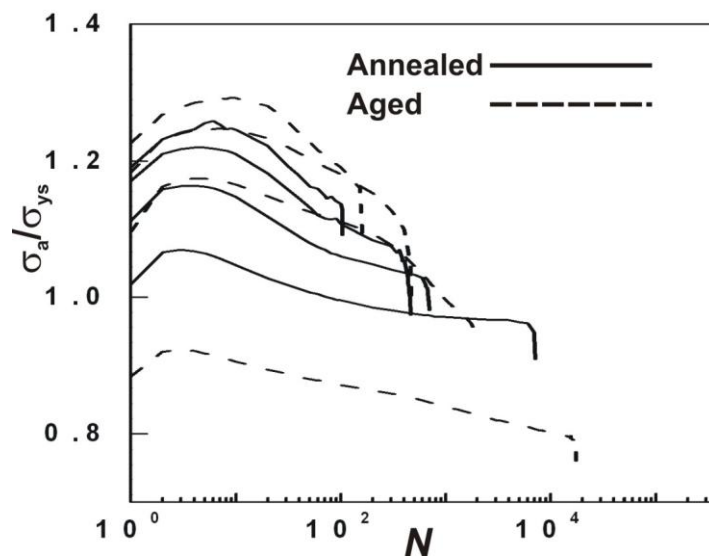


Fig. 4.18: Cyclic deformation curves of constant amplitude tests for annealed and aged condition; stress amplitude values normalized by σ_{ys} .

4.3.2 Cyclic stress-strain curve

The first $\frac{1}{4}$ cycles (initial loading) for each value of the total strain amplitude employed in the annealed and in the aged condition are plotted in Fig 4.19. It is observed that in both the heat treatment conditions there is coincidence of the first $\frac{1}{4}$ cycle for all four values of total strain amplitudes tested. This indicates the reliability of the test data. The stabilized loops for each values of employed total strain amplitude for annealed and aged condition are shown in Fig. 4.20a and 4.20b, respectively.

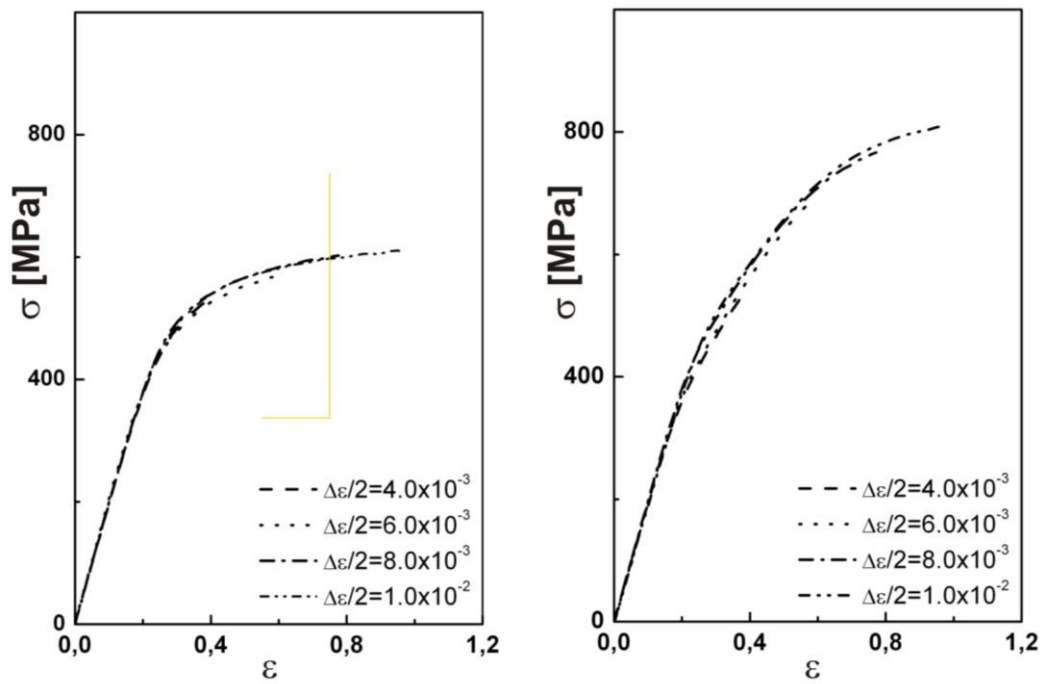


Fig. 4.19: First $\frac{1}{4}$ cycle (initial loading) for each value of the total strain amplitudes employed in the annealed and aged condition.

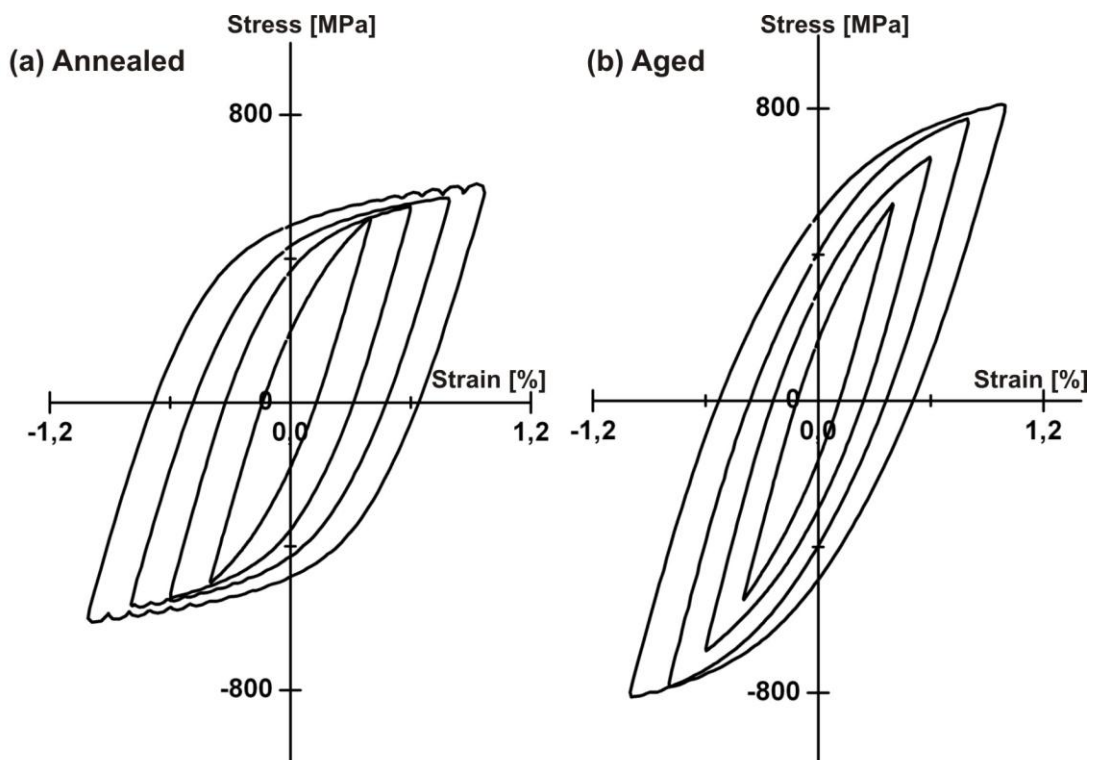


Fig. 4.20: Stabilized loops for each employed strain amplitude for annealed and aged condition.

The saturation stress amplitudes (σ_s) and the plastic strain amplitudes $(\Delta\varepsilon_{pl}/2)_s$ corresponding to the stabilized hysteresis loops (either mid-life or saturation) for each employed values of total strain amplitude were plotted to generate the cyclic stress-strain curves (CSSC), Fig. 4.21.

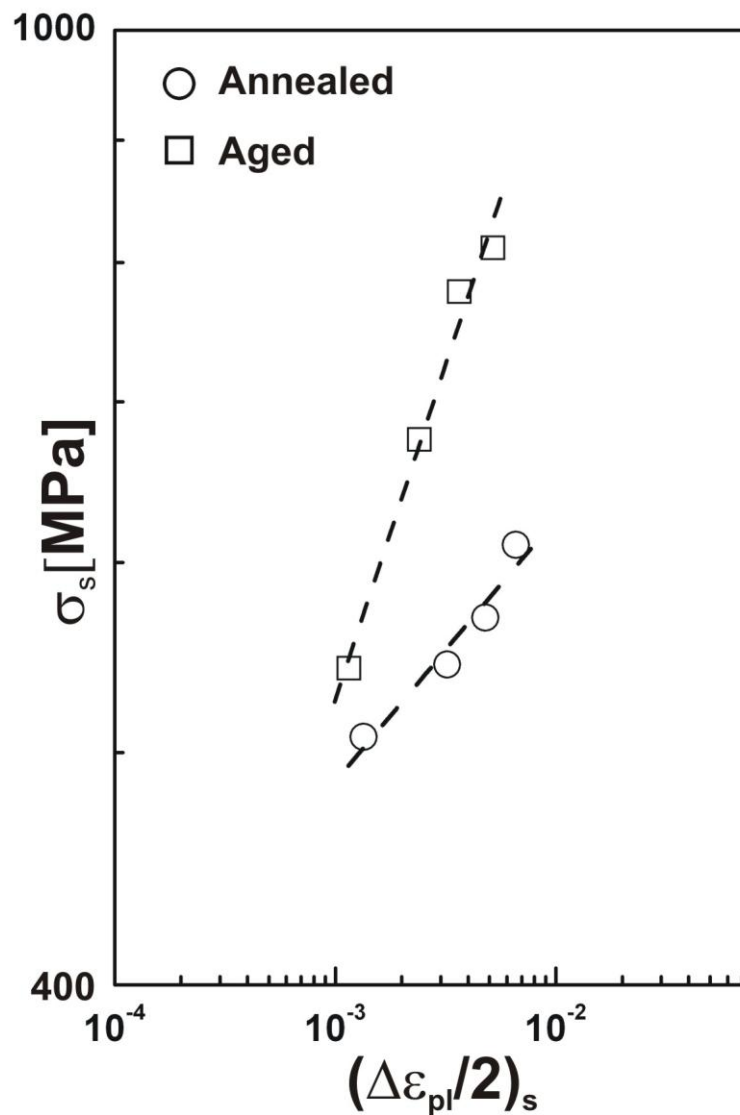


Fig. 4.21: Cyclic stress-strain curve of the DSS studied in annealed and in aged condition.

As can be clearly seen the CSSC in the range of plastic strain amplitudes 1.3×10^{-3} to 5.2×10^{-3} shows sensitivity to the aging treatment. The relative increase in stress amplitude with plastic strain amplitude is more pronounced at higher values of plastic strain amplitudes.

This is an expected behaviour due to the increase in the strength of the ferritic phase as a result of embrittlement.

The total strain amplitude for a completely reversed strain controlled test has an elastic and plastic segment as shown in Eq. 4.1.

$$\frac{\Delta\varepsilon}{2} = \frac{\Delta\varepsilon_e}{2} + \frac{\Delta\varepsilon_{pl}}{2} \quad (4.1)$$

In the range of strain amplitude used the $\Delta\sigma/2$ and $\Delta\varepsilon_{pl}/2$ follow the power law relationship shown in Eq. 4.2.

$$\frac{\Delta\sigma}{2} = K' \left(\frac{\Delta\varepsilon_{pl}}{2} \right)^{n'} \quad (4.2)$$

where K' is the cyclic strength coefficient and n' is the cyclic strain hardening exponent. In the above equation n' determines the hardening rate. It is reported though it is a material characteristic it does not vary significantly between casts of the same material. In contrast K' is related to the yield strength, which on the basis of the tensile data is known to vary significantly from cast to cast [81]. The calculated values of K' and n' are mentioned in Table 4.5.

Table 4.5: Calculated values of K' and n' .

	K'	n'
Annealed	1036	0.11
Aged	3610	0.28

The different values of n' obtained for annealed and aged conditions reflect that the rate of hardening is higher in the aged conditions. The K' values are also higher in the aged condition. This is a consequence of the increase in σ_{ys} value as a result of aging treatment. However, it is hard to interpret the cyclic hardening/softening response from the calculated values of K' and n' .

4.3.3 Cyclic life

The Coffin-Manson equation is written in the form given in Eq. 4.3 [81].

$$\frac{\Delta\varepsilon_{pl}}{2} = \varepsilon'_f (2N_f)^c \quad (4.3)$$

The fatigue life of the specimens in the annealed condition is related to the plastic strain amplitude in the range of $\Delta\varepsilon_{pl}/2$ values 1.3×10^{-3} to 6.6×10^{-3} . The fatigue life of the specimen in the aged condition of this study is related to the plastic strain amplitude in the range of $\Delta\varepsilon_{pl}/2$ values for 1.2×10^{-3} to 5.2×10^{-3} . The linearized log-log plot is shown in Fig. 4.22. A uniform slope was obtained for the range of plastic strain amplitude investigated in annealed and aged condition. The ε'_f and c values calculated from the Coffin-Manson plot are listed in Table 4.6.

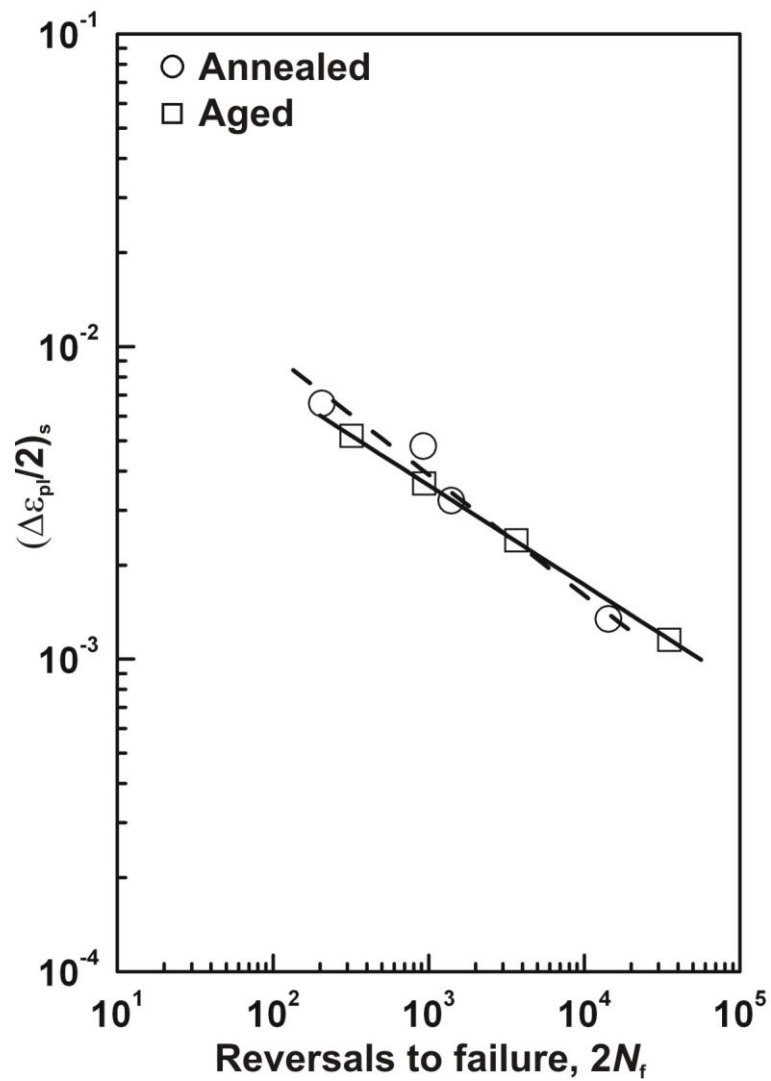


Fig. 4.22: Plastic strain amplitude versus reversals to failure.

Table 4.6: Calculated values of the Coffin-Manson parameters.

	ε'_f	c
Annealed	0.056	-0.38
Aged	0.033	-0.32

The following observations can be made from a comparison between these values in the annealed and aged condition.

- In the range of strain amplitude employed, fatigue life of DSS is longer in the aged condition at lower strain amplitudes, decreases and becomes similar at intermediate strain amplitude and becomes shorter at the highest strain amplitude used.
- Different slopes are obtained for annealed and aged condition in the Coffin-Manson plot. The slope is steeper in the annealed condition compared to the aged condition, which indicates that the fatigue life is better in the aged condition at lower values of plastic strain amplitudes and better in the annealed condition at a higher value of plastic strain amplitude.

4.3.4 Electron microscopic examination

Considering a rapid cyclic softening in the aged condition with increase in plastic strain amplitude and the fatigue life curves, TEM examination was carried out on LCF tested samples tested at $\Delta\varepsilon/2 = 8.0 \times 10^{-3}$ in the annealed and aged condition. The saturation values for the corresponding plastic strain amplitudes are 4.8×10^{-3} in the annealed condition and 3.7×10^{-3} in the aged condition. The specimens were cut transverse to the stress axis.

The features observed in the ferritic phase in the annealed condition are bundles of dislocations (Fig 4.23a), dislocation pile-ups (Fig 4.23c) and dislocation cell structures (Fig 4.23e). These structures were heterogeneously distributed.

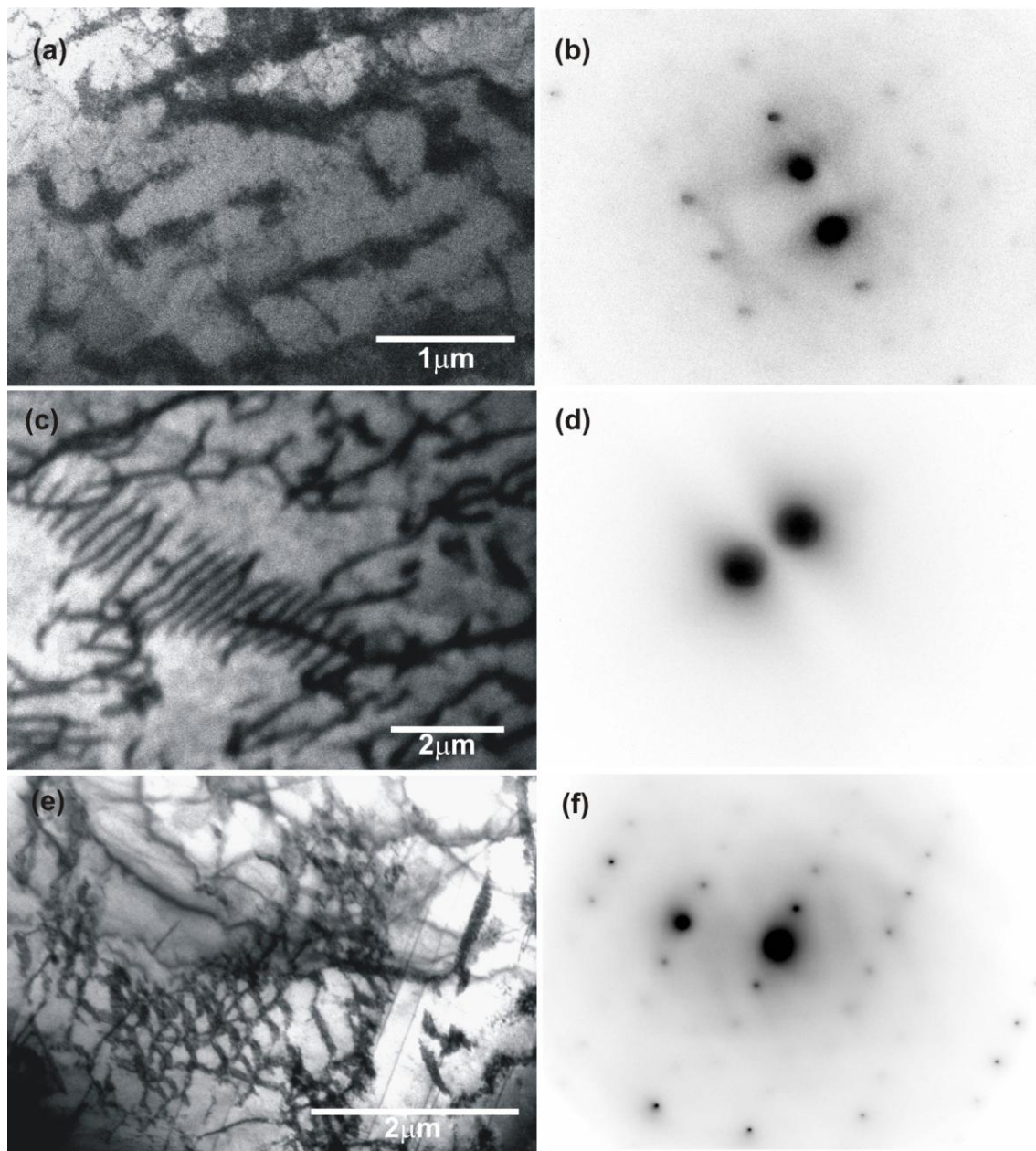


Fig. 4.23: (a)-(b) Bundles of dislocation; (c)-(d) dislocation pile-up; (e)-(f) cell structure. The dislocation arrangements were observed in the ferritic grain in the annealed condition after LCF test at $\Delta\varepsilon_{pl}/2 = 4.8 \times 10^{-3}$. The images are made in two-beam condition and the corresponding SADP are shown adjacent to the image.

Llanes *et al.* [111] observed a dominant structure evolution in the ferritic grain of AISI 329 grade of DSS at $\Delta\varepsilon_{pl}/2 > 1.0 \times 10^{-3}$ with the development of veins into wall structure. Kruml *et al.* [42] observed two characteristic types of dislocation structure in the ferritic phase of DIN X2CrNiMoN22-5 grade of DSS at $\Delta\varepsilon_{pl}/2 = 4.5 \times 10^{-3}$. Vein and wall structures

were found and a few short walls perpendicular to the direction of primary walls. These findings were interpreted as to be the onset of biaxial structure formation. Alvarez-Armas *et al.* [40] observed bundles of dislocation in the ferritic phase at $\Delta\varepsilon/2 = 4.0 \times 10^{-3}$ in the bulk of the sample. But interestingly they observed different features like homogeneous unidirectional walls aligned in the trace of $\{110\}$ plane in a specimen sliced near the surface. This wall structure was spread over both ferritic and austenitic grains and was found to have compliance with K-S orientation relationship. This observation is an indication that a direct relationship cannot be established between the slip markings on the surface, which are the plane traces, and the dislocation substructure in the bulk of the specimen. Cell structures were also observed in the ferritic grain at this strain amplitude, indicating onset of wavy slip in the ferritic phase. Mateo *et al.* [112] observed cells, wall structures and loop patches corresponding to half life at $\Delta\varepsilon_{pl}/2 = 6.0 \times 10^{-3}$. The structures observed in the ferritic phase of DSS at the similar values of strain amplitudes are listed in Table 4.7.

Table 4.7: Dislocation sub-structure observed in the ferritic phase of DSS by other researchers.

Name of researchers	DSS grade	Strain amplitude	Dislocation substructure
Alvarez-Armas <i>et al.</i> [40]	Low nitrogen DIN W Nr.1.4460	$\Delta\varepsilon/2 = 4.0 \times 10^{-3}$	Bundles of dislocations
Mateo <i>et al.</i> [112]	SAF 2507	$\Delta\varepsilon_{pl}/2 = 6.0 \times 10^{-3}$	Cell structure, developed wall structure, dense loop patches and poorly defined channels
Kruml <i>et al.</i> [42]	DIN X2CrNiMoN22-5	$\Delta\varepsilon_{pl}/2 = 4.5 \times 10^{-3}$	Veins, wall structure and a few perpendicular walls indicating the onset of formation of biaxial labyrinth structure

The substructural evolution in the austenitic phase is well documented [42,113-114]. The planar arrays of dislocations are usually observed at low strain amplitude. Two major factors, which influence the dislocation behaviour are (a) stress and (b) nitrogen content [38-41]. At higher values of strain amplitudes the secondary slip system is activated and cross slip can initiate and as a result a cell structure is observed. Apart from higher stress, nitrogen is also known to modify the substructural evolution in austenite. With increase in nitrogen

content the SFE value decreases. That means nitrogen promotes planar slip increasing the fatigue strength and inhibiting strain localization.

The LCF tested sample ($\Delta\varepsilon/2 = 8.0 \times 10^{-3}$) in the aged condition was studied in TEM. In the present investigation, at $\Delta\varepsilon/2 = 8.0 \times 10^{-3}$ the behaviour of substructural evolution was modified as a result of aging treatment. In the annealed condition only planar dislocation arrays were observed in the austenitic phase as shown in Fig. 4.24a. However, in the aged condition the onset of cell formation was observed at the same strain amplitude. This can be attributed to the reason mentioned already in the beginning of the paragraph, i.e. the stress amplitude values at $\Delta\varepsilon/2 = 8.0 \times 10^{-3}$ is higher for the aged condition as compared to the annealed condition. Figure 4.24c shows this beginning of cell formation in austenite in the aged condition.

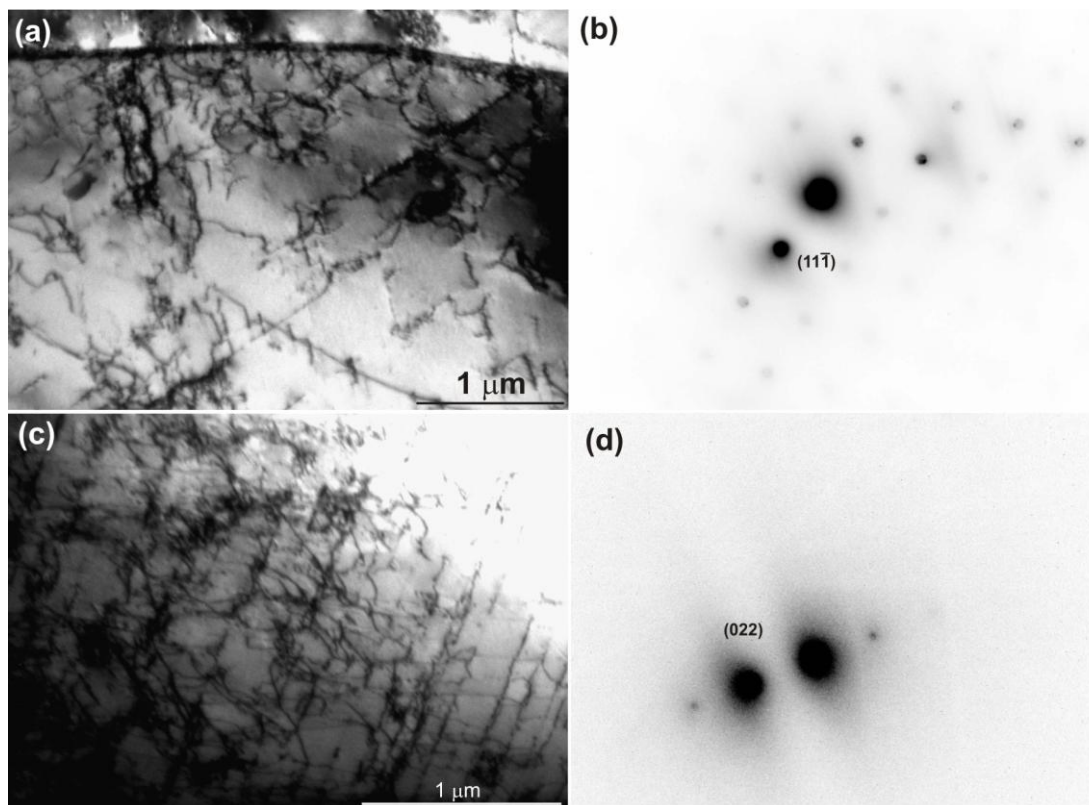


Fig. 4.24: (a)-(b) Planer arrangement of dislocations in the austenitic grain of the annealed condition formed at $\Delta\varepsilon_p/2 = 4.8 \times 10^{-3}$ (zone axis = [022]); (c)-(d) The start of cell formation in the austenitic grain in the aged condition, $\Delta\varepsilon_p/2 = 3.7 \times 10^{-3}$ (zone axis = [100]).

Two prominent features are observed in the bright field image in a ferritic grain in the aged condition shown in Fig. 4.25: (i) the arrow marked regions showing some unusual contrast; (ii) the coffee bean contrast at the central region of the micrograph indicate that the size of the precipitate is very small. The regions of interest are the arrow-marked regions, which appear to be highly strained zones and were found in all the ferritic grains in the aged condition. These zones are most likely the zones of softening and found at many places in the ferritic grains in the aged condition.

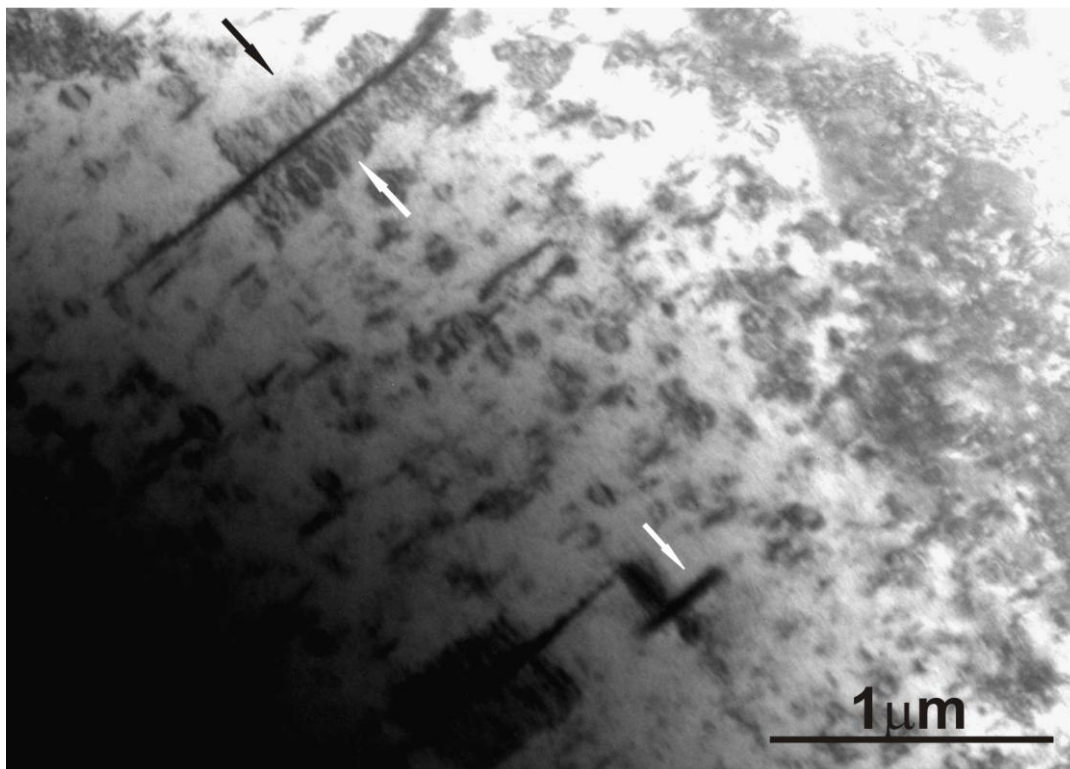


Fig. 4.25: TEM bright field image of the ferritic phase in the aged condition. The arrowed regions are the highly strained zones, the precipitates show coffee bean contrast at the center; $\Delta\epsilon_p/2 = 3.7 \times 10^{-3}$.

Comparing Fig. 4.8 and 4.9, which shows the state of ferritic phase prior to fatigue loading, with Fig. 4.25 showing the state of ferritic phase after fatigue loading, the following changes can be observed:

- The needle-like precipitates seen in Fig. 4.8 throughout the whole grain completely disappear after fatigue loading as can be seen in Fig. 4.25. This can be a result of rapid

cyclic softening in the aged condition. Apart from this appearance of coffee bean contrast, in some areas is an indication of reduction of size of these precipitates.

- The precipitates forming an array in Fig. 4.9 appear to coalesce after fatigue loading as shown in Fig.4.25 and with a higher magnification in Fig. 4.26. Coalescence of carbide precipitates as a cause of cyclic softening has been reported for tempered martensitic steel [115-116]. The mechanism is enhanced at elevated temperature and with mechanical loading [116]. The coalescence of the array of precipitates observed in Fig. 4.9 along with disappearance of the needle-shaped precipitate may be an additional reason for cyclic softening. The increase in rate of softening with increase in strain amplitude in the aged condition and enhancement of the mechanism of coalescence of precipitates with mechanical loading [116] are in agreement.

It is also important to note that the usual strain localization features such as slip bands were not observed in the ferritic phase in the aged condition.

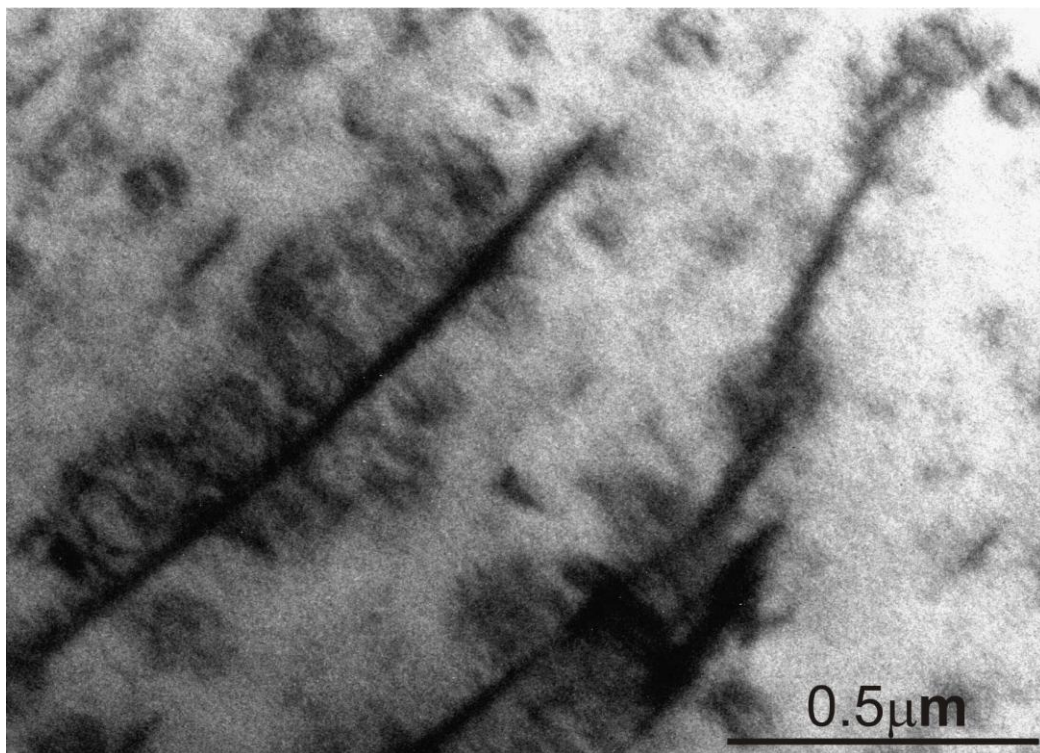


Fig. 4.26: A high magnification photograph of the highly strained zones shown in Fig. 4.26; $\Delta\epsilon_p/2 = 3.7 \times 10^{-3}$.

The cyclic softening of the ferritic phase aged at 475°C was initially investigated in pure ferritic alloys. Park *et al.* [117] attributed the observed low cycle fatigue softening for their Fe-1Cr-1Mo alloy to the localized demodulation of the spinodal microstructure due to irreversible dislocation motion. The same mechanism has also been observed in fcc alloys those undergo spinodal decomposition [118-119]. Anglada *et al.* [120] have reported a similar softening behaviour during cyclic deformation of an aged Fe-28Cr-4Ni-Nb alloy and attributed this to the demodulation of spinodal microstructure. They considered the slip symmetry of BCC alloys and a more pronounced asymmetry at higher values of plastic strain amplitude as being responsible for such kind of demodulation. In explaining the involvement of the ferritic phase of the aged material in plastic deformation at higher values of plastic strain amplitude, Llanes *et al.* [111] postulated that the ferritic phase carries out plastic deformation through gradual demodulation of the spinodal microstructure by dislocation glide irreversibility and deformation twinning. However, this behaviour was observed to occur heterogeneously and was attributed to grain orientation and cyclic behaviour of neighbouring grains.

The fracture surface of the LCF tested samples at $\Delta\varepsilon/2 = 8.0 \times 10^{-3}$ in the annealed and the aged condition is shown in Fig. 4.27. For this strain amplitude important observations are: (i) no striations observed both in the annealed and the aged condition, and (ii) the fracture surface in the aged condition shows some smeared off regions. The absence of striations indicates that the final failure has occurred due to coalescence of microstructurally short (stage I) cracks in both annealed and aged conditions. The smeared off features in the aged conditions appear to be crystallographic in nature and they might correspond to the severely strained regions as discussed earlier.

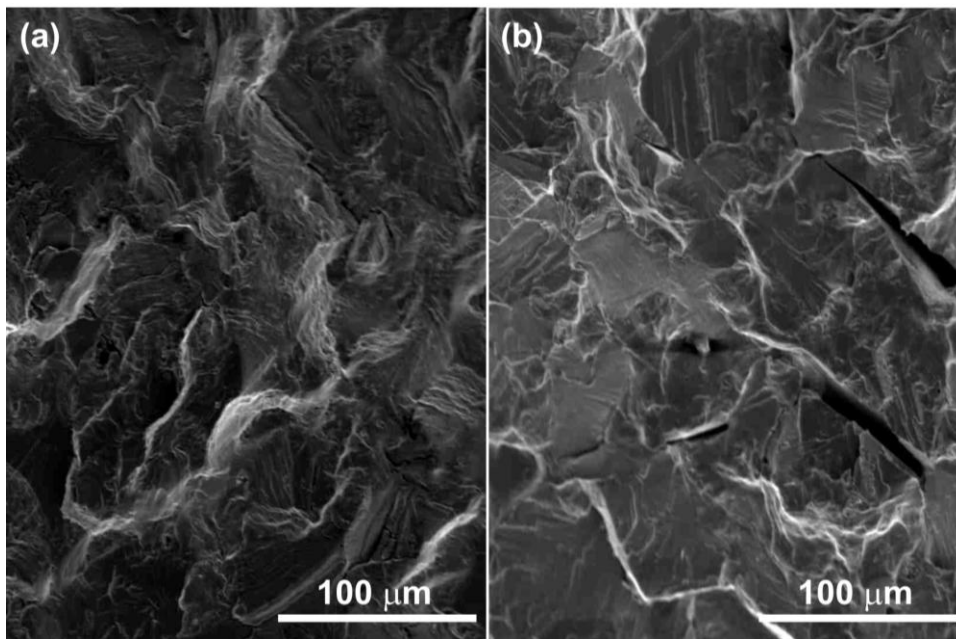


Fig. 4.27: Fractographs of LCF tested samples: (a) annealed; (b) aged; conditions, $\Delta\epsilon/2 = 8 \times 10^{-2}$.

4.4 Fatigue crack initiation in DSS embrittled at 475°C

The evolution of surface roughness, subsequent nucleation and growth of short cracks in DSS by cyclic loading is strongly influenced by the microstructural parameters, i.e. grain size, grain orientation, grain and phase boundary geometry, i.e. grain boundary character distribution (GBCD), and precipitation condition. The crack initiation and growth in particular grain in DSS depend on the orientation, inherent strength and toughness properties of neighbouring grains, and it is very important to know and understand how these factors determine fatigue damage evolution.

In DSS aged at 475°C, the difference between the mechanical properties of austenite and ferrite becomes more pronounced. In the case of cyclic loading of DSS in annealed condition, slip bands represent the main crack initiation site either in austenite or ferrite depending on the applied strain amplitude [3]. However, the slip incompatibilities created at the inter-phase boundaries after the aging treatment at 475°C may lead to a non-uniform distribution of surface damage. In a recent investigation, in situ tensile tests have been performed on a thermally aged DSS and EBSD technique has been used to correlate local phase morphology with crystallographic properties [103].

The present investigation focuses on the aspect of crystallographic parameters that influence the surface damage process during stress controlled fatigue tests in DSS aged at 475°C. The push-pull fully reversed stress-controlled fatigue tests were conducted at two values of stress amplitude: $\Delta\sigma/2 = 400$ MPa and 500 MPa till final failure of the specimen. One test was performed for few cycles at high stress amplitude, ($\Delta\sigma/2 = 650$ MPa) in order to observe and compare the surface evolution with low stress amplitude tests. The fatigue tests were interrupted after every 1000 cycles to monitor the damage evolution on the electrolytically polished surface under SEM. EBSD scans were performed typically with a step size of $1 \mu\text{m}$ on $500 \times 500 \mu\text{m}$ areas on the specimen before fatigue testing. Some scans were also performed at the crack initiation sites during interruption of tests.

The evolution of damage was related to the crystallographic parameters. The slip bands on the free surface correspond to the lines of intersection of the slip planes with the surface. With the help of OIM software the plane traces corresponding to a particular plane in the grain is superimposed on the image. Figure 4.28 shows the SEM image with superimposed traces of $\{110\}$ family of planes on the ferritic phase.

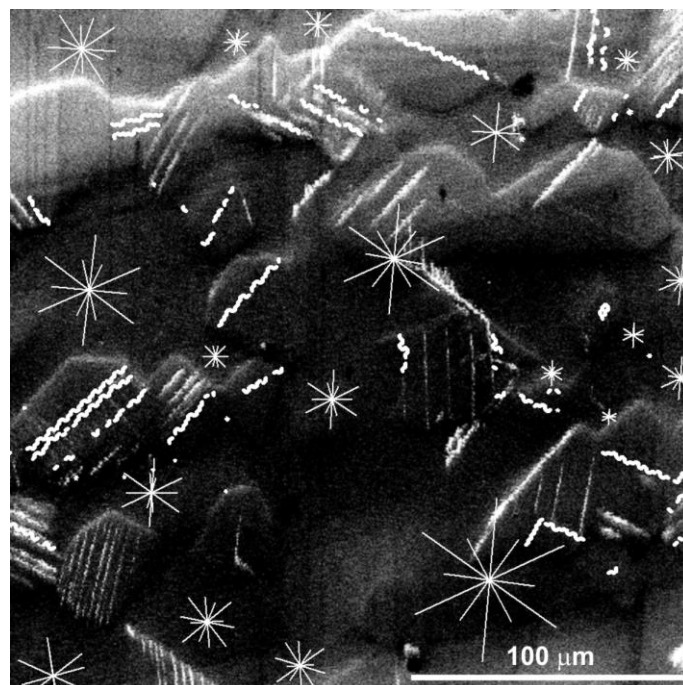


Fig. 4.28: Plane traces $\{110\}$ of planes mapped on SEM image by OIM.

The influence of grain boundaries and phase boundaries on the evolution of surface damage in DSS is well established from a number of earlier studies. In the purview of grain boundary engineering by thermomechanical treatments, grain boundary character distribution (GBCD) obtained by EBSD is a very popular parameter. Coincident Site Lattice (CSL) boundaries are boundaries with a special character. These boundaries are classified in terms of Σ values. CSL boundaries are special because they have a given fraction of atoms in the grain boundary plane, which are coincident to both lattices separated by the grain boundary. The Σ value denotes the fraction of atoms in coincidence, e.g. a $\Sigma 5$ boundary has 1 in 5 atoms at coincident sites. In the present study less than 10° misorientation are defined as low angle boundaries (LAB), 10° to 30° misorientation are defined as medium angle boundaries and more than 30° misorientation are defined as high angle boundaries (HAB). The misorientation plot revealed in all the scans that $\alpha\gamma$ phase boundaries are HABs. Figure 4.29 shows the OIM generated plot showing $\alpha\gamma$ phase boundaries, $\gamma\gamma$ grain boundaries and $\Sigma 3$ CSL boundaries.

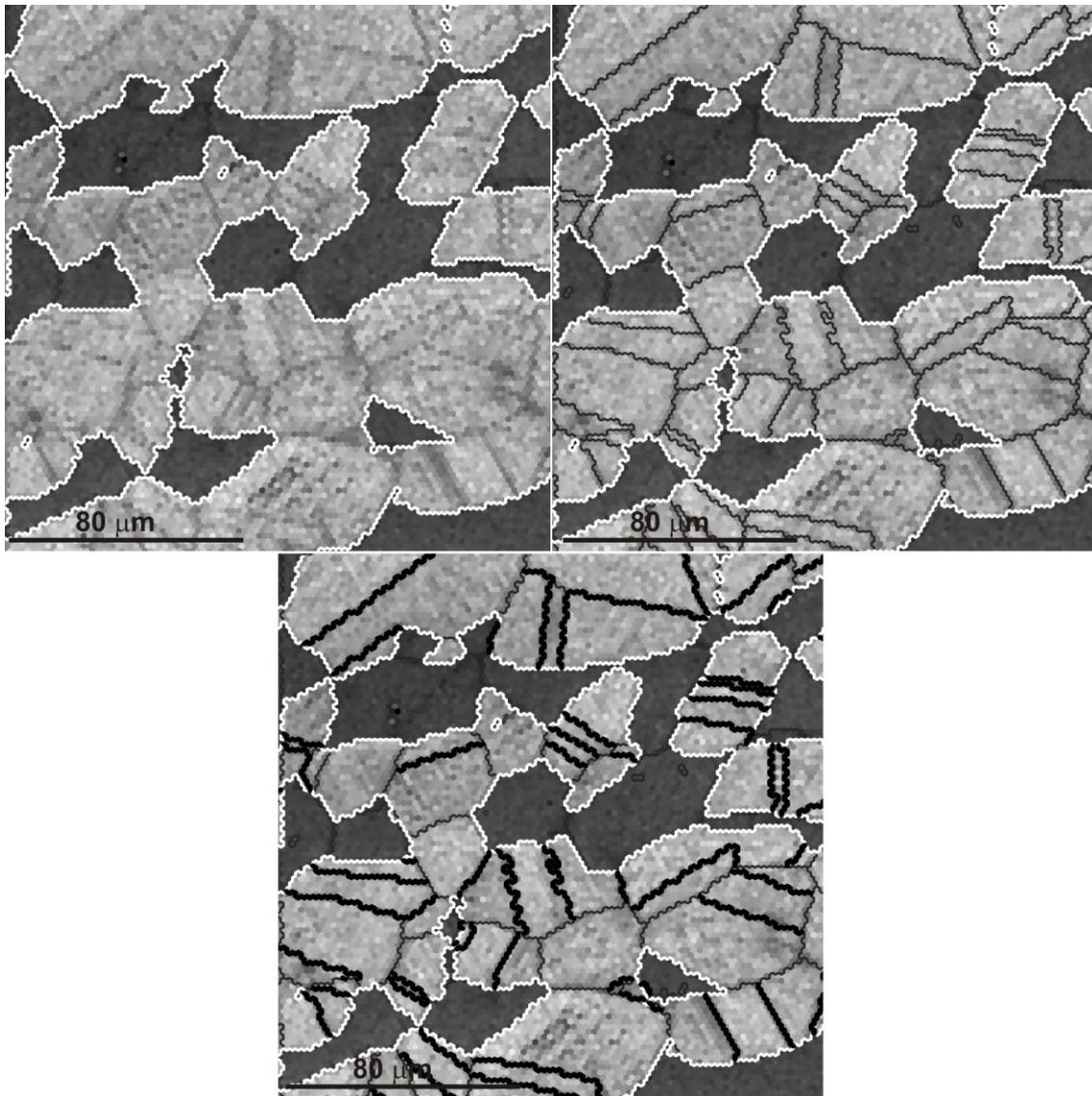


Fig. 4.29: OIM generated plot of (a) $\alpha\gamma$ phase boundaries; (b) $\alpha\gamma$ phase boundaries and $\gamma\gamma$ grain boundaries; (c) $\alpha\gamma$ phase boundaries, $\gamma\gamma$ grain boundaries and $\Sigma 3$ CSL boundaries.

At $\Delta\sigma/2 = 400$ MPa, in the first interruption at $N = 1000$ cycles slip markings were observed in the austenitic grains. These slip markings corresponds to $\{111\}$ family of planes. The slip markings were more prominent in one set of $\{111\}$ planes and just observable in another set. There was no change observed in the ferritic phase in this interruption. After every 1000 cycles the same grain was studied and with gradual increase in the number of cycles the slip markings in the austenite were more coarsened and accentuated. At $N = 3000$ cycles some cracks were detected in the austenitic grains. Figure 4.30 shows three such cracks recorded after $N = 3000$ cycles. Crack number c1 and c3 were found to be in the slip

marking corresponding to a $\{111\}$ plane trace of austenite and crack number c2 was found to be on the $\Sigma 3$ CSL boundary. After $N = 6000$ cycles the activation of $\{110\}$ slip system can be observed in the adjacent ferritic grain (δ_1).

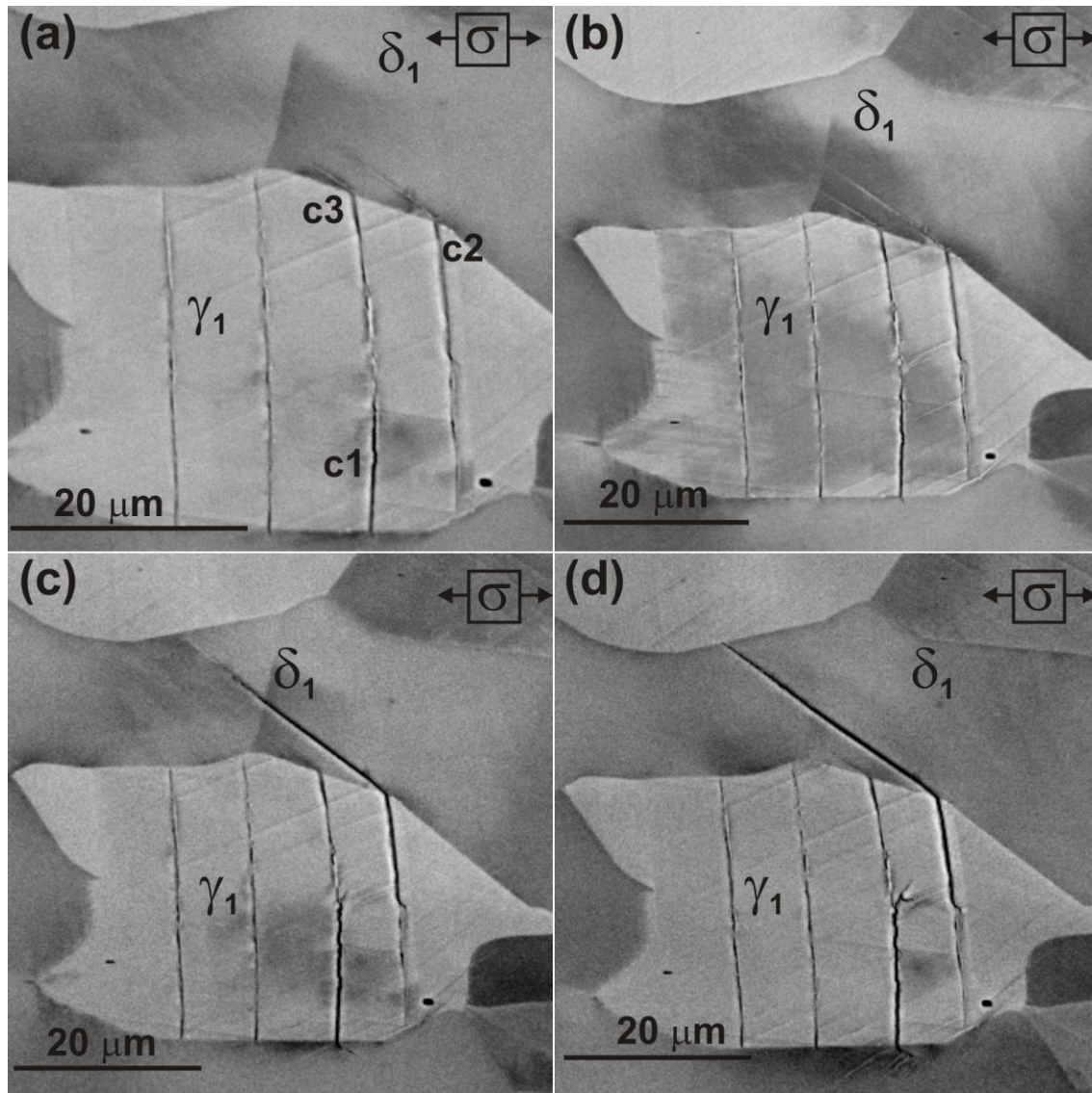


Fig. 4.30: Three cracks identified in the austenitic grains and observed after: (a) $N = 3000$ cycles; (b) $N = 6000$ cycles; (c) $N = 9000$ cycles; and (d) $N = 12000$ cycles at $\Delta\sigma/2 = 400$ MPa.

Figure 4.31 shows the growth of the same cracks. The image was recorded after $N = 27000$ cycles.

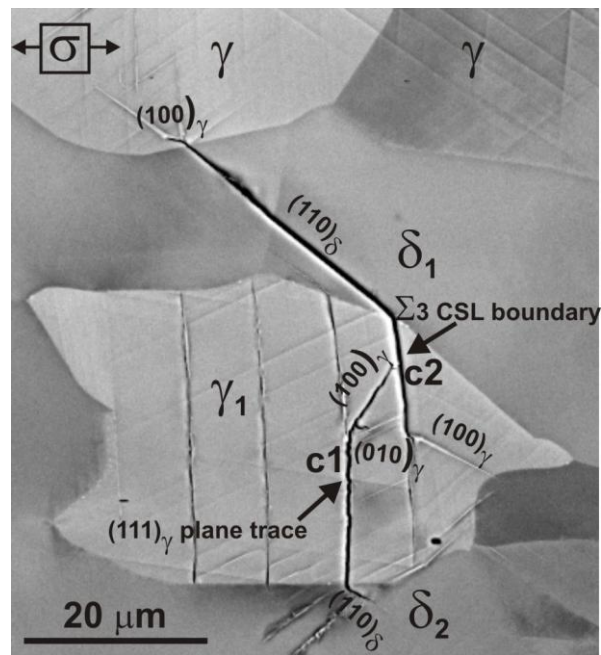


Fig. 4.31: The growth of crack c2 observed after $N = 27000$ cycles at $\Delta\sigma/2 = 400$ MPa.

The crystallographic information on the grains are given in Table 4.8.

Table 4.8: Crystallographic data of grains shown in Fig. 4.31.

Grain number	Average orientation of grain [Euler angles: ϕ_1, ϕ, ϕ_2 (Bunge)]	Misorientation	Slip system	Schmid factor
δ_1	[145.2 52.5 224.3]	$\delta_1\gamma_1$ GB = 56°	$\{110\}\langle 1\bar{1}1\rangle$	0.45
γ_1	[358.5 23.0 321.5]	-	$\{111\}\langle 1\bar{1}0\rangle$ $\{100\}\langle 001\rangle$	0.425 0.418
δ_2	[146.2 50.6 222.1]	$\delta_2\gamma_1$ GB = 56.4°	$\{110\}\langle 1\bar{1}1\rangle$	0.45

As can be seen from Figs. 4.30 and 4.31 crack number c1 and c2 are on the slip marking corresponding to the $\{111\}$ plane trace and crack number c2 is on a $\Sigma 3$ CSL boundary. The growth of crack c3 appears to have stopped, even after $N = 27000$ cycles, whereas crack c1 and c2 have grown at both ends. From the growth pattern of crack number c1 and c3 the following observations can be made:

- The c1 crack grows in double slip mode in a $\{100\}$ plane while growing inside the austenitic grain as can be seen in Fig. 4.31

- The c2 crack grows along the $\Sigma 3$ CSL boundary while growing inside the austenitic grain
- Both the cracks encounter the $\alpha\gamma$ phase boundary and activate the $\{110\}$ slip plane in the adjacent ferritic grains.
- The ferritic grains δ_1 and δ_2 have very similar Schmid factors and misorientations with grain γ_1 . However, the growth of c1 and c3 cracks into the ferritic grains is different as can be seen in Fig. 4.31. This means apart from misorientation and Schmid factor, there are some other factors, which also determine the strength of the phase boundary. Stolarz and Foct [121] have also observed the influence of topological parameters on the growth of short cracks in two-phase alloys, particularly when the crack encounters an interphase interface. When the slip transfer mechanism between phases is modified because of embrittlement then the growth of a short crack into the neighbouring phase will be more of mechanics than mechanism. This can be understood from point of view of the stress intensification. In the present investigation a crack of 20-30 μm , which spans the austenitic grain activates the slip system in the ferritic grain with increase in number of cycles. The stress intensification is a function of crack geometry as known from the long crack theory. Therefore, a topological difference between phases will influence the stress intensification at the phase boundary.
- It can be seen from Fig. 4.30d that the c2 crack again encounters a $\alpha\gamma$ phase boundary. From Fig. 4.31 it is evident that the crack has very little growth between $N = 12000$ cycles to $N = 27000$ cycles. It is also observed that the crack reenters the adjacent austenite grain along the $\{100\}$ slip marking and not on a $\{111\}$ slip marking.

At $\Delta\sigma/2 = 400$ MPa most of the cracks were observed to initiate on the $\{111\}$ plane traces of austenite. Two such austenitic grains are shown in Fig. 4.32.

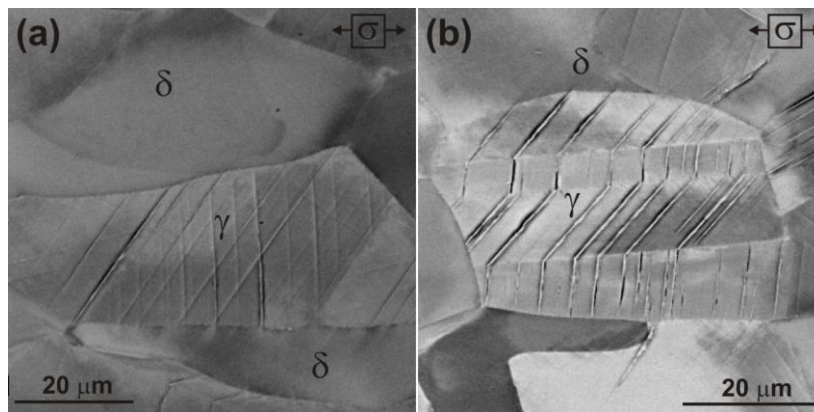


Fig. 4.32: The $\{111\}$ plane traces are the sites for crack initiation at $\Delta\sigma/2 = 400$ MPa.

The austenitic grains, which were detected to have pronounced slip markings corresponding to the $\{111\}$ plane traces, had high Schmid factor values. The typical crack growth in alternating slip planes were also observed in a few grains. One such example is shown in Fig. 4.33.

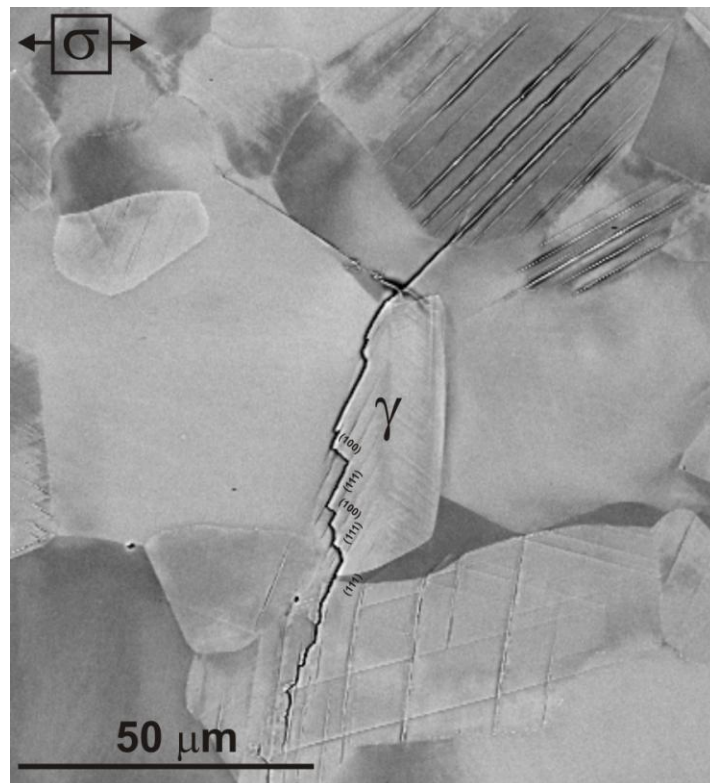


Fig. 4.33: Crack growth in alternating slip planes.

At $\Delta\sigma/2 = 500$ MPa one difference was observed as compared to $\Delta\sigma/2 = 400$ MPa. Along with the slip markings corresponding to $\{111\}$ plane traces, a higher number of cracks were initiated at $\Sigma 3$ CSL boundaries. One such crack is shown in Fig. 4.34.

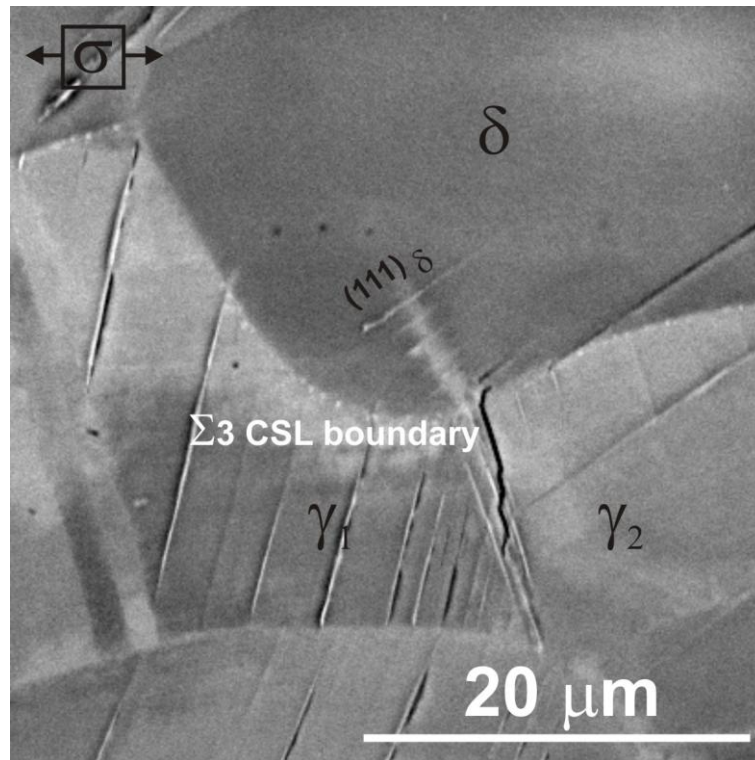


Fig. 4.34: Crack initiation at $\Sigma 3$ CSL boundary.

The crystallographic data of the grains shown in Fig 4.34 are mentioned in Table 4.9.

Table 4.9: Crystallographic data of grains shown in Fig. 4.34.

Grain number	Average orientation of grain [Euler angles: ϕ_1, ϕ, ϕ_2 (Bunge)]	Misorientation	Slip system	Schmid factor
γ_1	[244.0 23.2 73.7]	$\delta_1\gamma_1 = 56.4^\circ$	$\{111\}\langle 1\bar{1}0\rangle$	0.30
δ_1	[134.1 37.2 213.2]	-	$\{110\}\langle 1\bar{1}1\rangle$	0.40
γ_2	[161.0 45.0 200.2]	$\delta_1\gamma_2 = 20.6^\circ$	$\{111\}\langle 1\bar{1}0\rangle$	0.103

Activation of $\{110\}$ slip system can also be observed in the ferritic grain. However, without the impingement of a short crack initiated in the austenitic grain, at $\alpha\gamma$ phase boundary an activation of a slip system in the ferritic phase at this stress amplitude was very

rare. The observation of slip markings in the γ_1 grain and absence of slip markings in the γ_2 grain may be a direct consequence of low Schmid factor of γ_2 grain corresponding to the $\{111\}\langle 1\bar{1}0\rangle$ slip system.

Figure 4.35a shows the growth of another crack initiated at $\Sigma 3$ CSL boundary at 1. The SEM image from which EBSD scan was made and the $\Sigma 3$ CSL boundary plot obtained from OIM are shown in Fig. 4.35b.

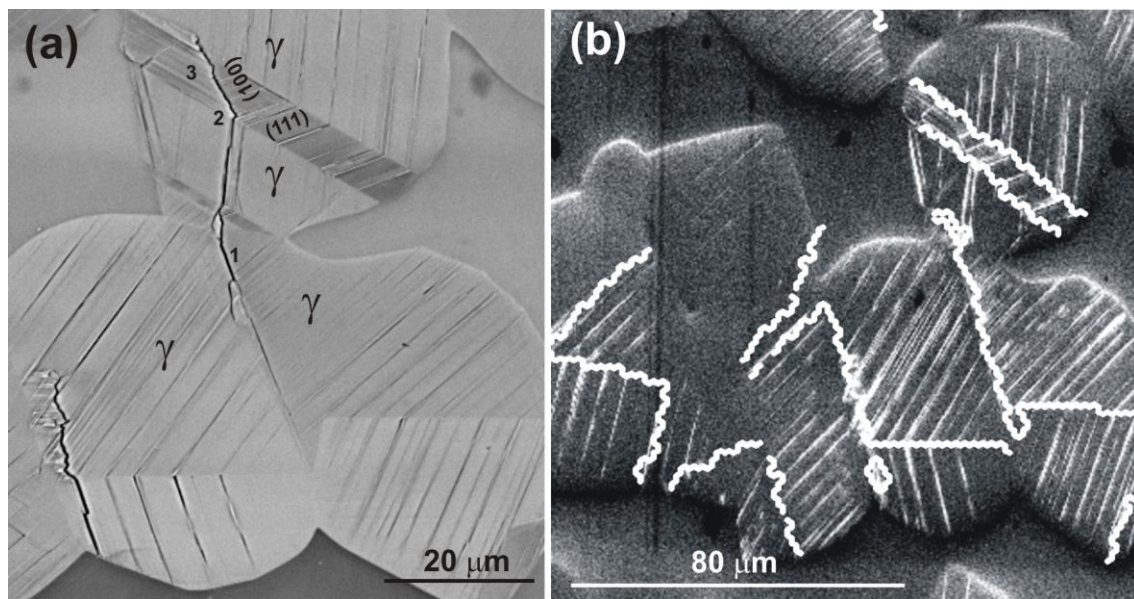


Fig. 4.35: Crack initiation at $\Sigma 3$ CSL boundary.

This crack grows into the next austenitic grain and encounters another $\Sigma 3$ CSL boundary at 2. Inside the twinned region the crack grows for a small length in the slip markings corresponding to $\{111\}$ plane trace. However at 3 the crack path deviates and grows in double slip mode.

At $\Delta\sigma/2 = 650$ MPa the specimen surface was examined after $N = 300$ cycles. A pronounced surface relief was observed in the austenitic grain as shown in Fig. 4.36. Such surface relief in austenite is found only at high stresses and with the activation of secondary slip [114].

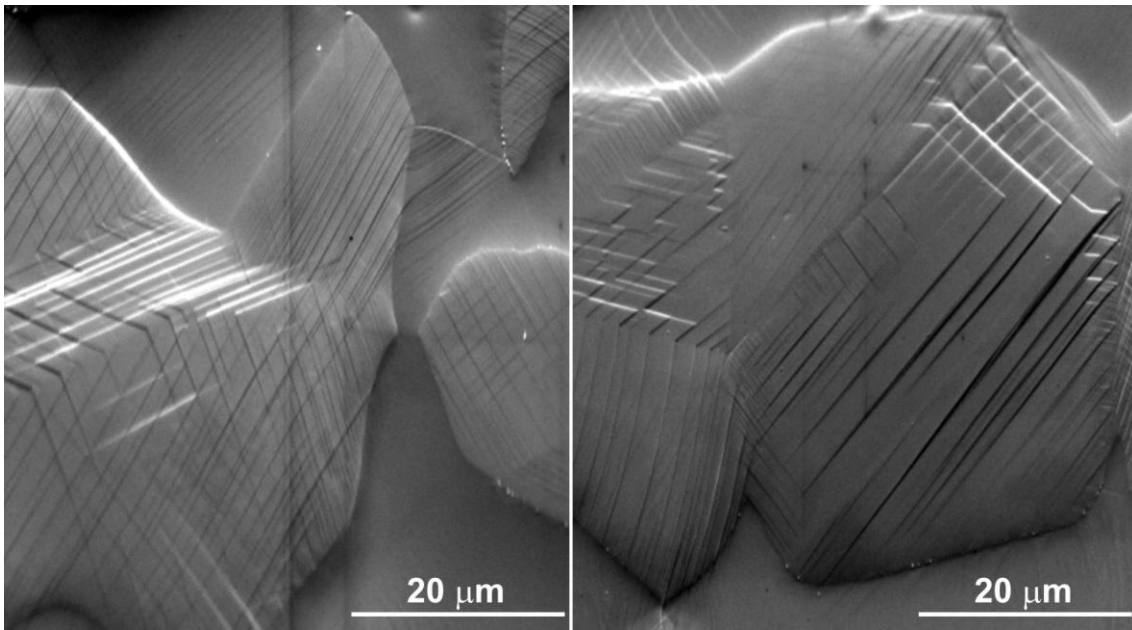


Fig. 4.36: Surface relief observed in the austenitic phase: $\Delta\sigma/2 = 650$ MPa, $N = 300$ cycles.

In the ferritic phase cleavage cracks were observed as shown in Fig. 4.37. The cracks corresponds to $\{100\}$ planes.

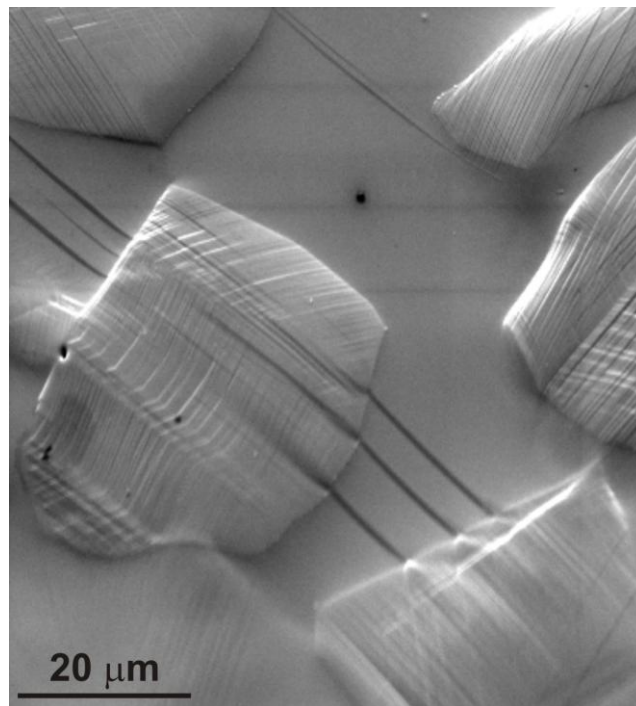


Fig. 4.37: Cleavage cracks observed in the ferritic phase $\Delta\sigma/2 = 650$ MPa, $N = 300$ cycles.

TEM examination of the sample fatigued at $\Delta\sigma/2 = 650$ MPa for $N = 300$ cycles revealed no strain localization feature in the ferritic phase. This is in agreement with the results obtained from the strain-controlled fatigue test. However, in the austenitic grains start of cell formation was observed as shown in Fig. 4.38.

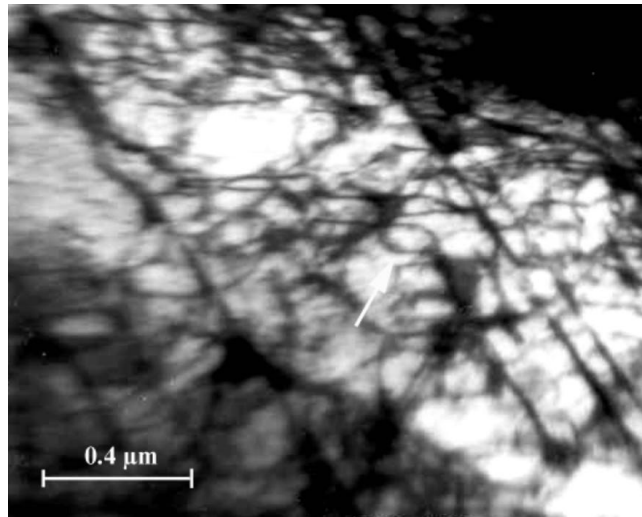


Fig. 4.38: Beginning of cell formation in austenitic grains.

Chapter 5 Discussion

In this chapter some of the significant results obtained in the present investigation are compared and discussed with the results obtained by other researchers who investigated similar aspects of the fatigue behaviour of DSS. The chapter is divided into three sections. The precipitation behaviour due to 475°C aging treatment of DSS is discussed in section 5.1. The effect of 475°C embrittlement on low-cycle fatigue behaviour of DSS is discussed in section 5.2. The fatigue crack initiation behaviour of DSS embrittled at 475°C is discussed in section 5.3.

5.1 475°C embrittlement of DSS

The problem of the high temperature application of ferritic stainless steel as a result of 475°C embrittlement was well known [26-29,90-94]. Since this problem was inherent to ferritic microstructure research emphasis on the embrittlement problem in this temperature range was mostly confined to solely binary iron-chromium alloys and in some cases commercial grades of ferritic stainless steels [26-29]. DSS on the other hand contains both ferrite and austenite in varying proportions in the microstructure depending on the alloy composition and the ferritic phase is metastable δ -ferrite as compared to α -ferrite in ferritic stainless steels. As only the ferritic phase is embrittled during 475°C embrittlement, the degradation in material properties directly depends on the state of the ferritic phase. The effect of the state of ferritic phase (stable or metastable) at room temperature on 475°C embrittlement is not very well known. But the alloy composition that determines the ferrite volume fraction, distribution of ferritic phase in the matrix, their grain size and grain shape is found to affect the nature of precipitation and the degree of embrittlement [88-89].

The different possibilities for the segregation or precipitation in the ferritic phase resulting from the aging treatment at 475°C reported so far are:

- Formation of α' either through spinodal decomposition (infinitesimal composition fluctuation in a solid solution) or through the mechanism of nucleation and growth.

- Formation of an intermetallic G-phase.
- Precipitation of carbides and nitrides at grain boundaries.

Weng *et al.* [30] carried out detailed investigations on the nano-scaled structure of the 2205 wrought DSS grade with the help of field-emission gun (FEG) transmission electron microscopy. The extent of phase separation that takes place due to 475°C embrittlement is determined through a nanometer-scaled chemical analysis from a FEG-TEM containing an EDS as shown in Fig. 5.1. The fine scale isotropic spinodal decomposition of ferritic phase reveal segregation of chromium to the α' phase. Molybdenum and manganese are partitioned to the α' phase, while nickel is partitioned to the α phase.

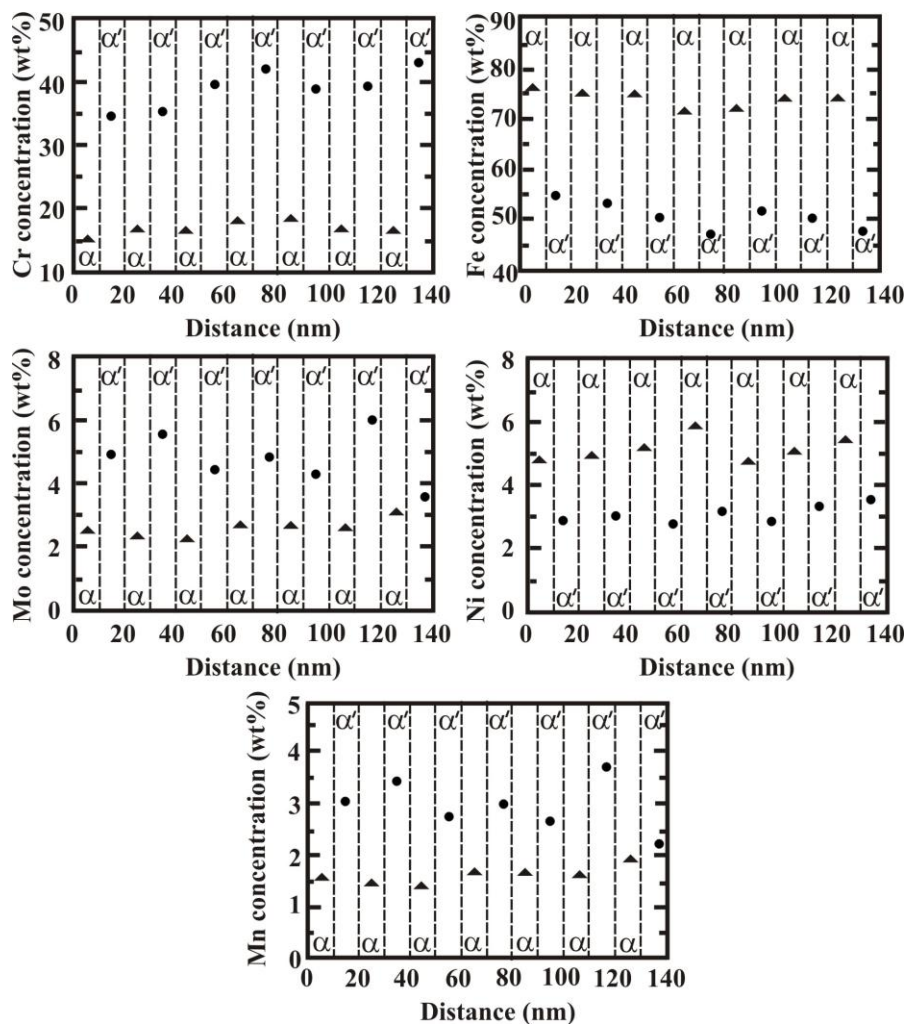


Fig. 5.1: Concentration profile of α and α' phases obtained from the data of nano-scaled EDX analysis [30].

The contrast reported being observed in TEM for the spinodal decomposition in iron-chromium alloy system is mottling [29-30]. The mottling contrast observed in [30] is shown in Fig. 5.2. In the presently investigated DSS, mottling was not observed in the aged condition.

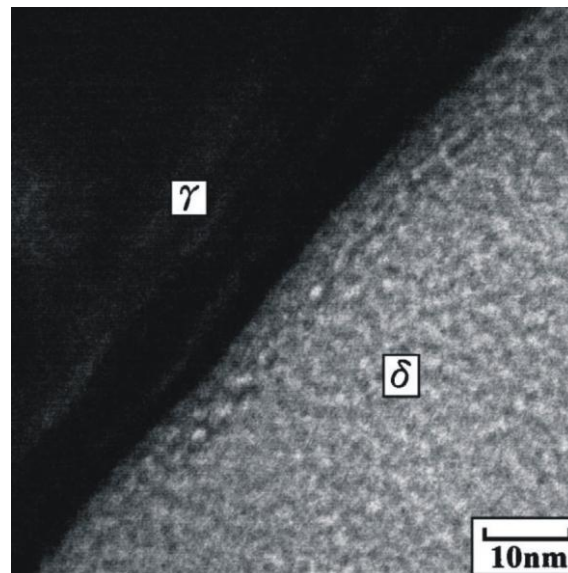


Fig. 5.2: FEG-TEM showing ferrite and adjacent austenite in the specimen aged at 475°C for 2 hours [30].

Regarding the α' precipitation, Cahn [95] discussed in detail the thermodynamic distinction within the miscibility gap for spinodal decomposition versus nucleation and growth of α' taking surface tension and elastic energy into account. According to him there should be no change in molar volume with composition in an infinite isotropic solid free from imperfections in order to have spinodal decomposition. So the sustainability of spinodal decomposition is very stringent for a multi-component ferritic phase as in the case of DSS, where many alloying elements other than chromium are partitioned to the ferritic phase.

Grobner [26] reported that in the temperature range of 371-482°C iron-chromium alloy with 18 at.% chromium embrittled in times as short as 2 hours, whereas with 14 at.% chromium, embrittlement was observed after longer exposure time. This is a clear indication of the sensitivity of this embrittlement to alloy composition. Interstitial elements were found to accelerate the embrittlement caused by precipitation of α' on dislocations, whereas

substitutional alloying elements such as molybdenum and titanium did not substantially affect kinetics of embrittlement. Chandra and Schwartz [27] estimated the solubility of chromium in iron to be 12 at.% at 475°C and alloys with 12-30 at.% chromium decompose through nucleation and growth of α' . From these results it is expected that the present grade of DSS should have α' precipitation through nucleation and growth mechanism, as the content of chromium is 22 wt.%.

Studying DSS via Mössbauer spectroscopy is difficult as austenite is paramagnetic and obscures the detection of paramagnetic α' phase. However, Solomon *et al.* [29] successfully investigated the effects of alloying elements on 475°C embrittlement with the help of Mössbauer spectroscopy and transmission electron microscopy in a DSS and seven single-phase ferritic alloys. They showed that nickel promotes the formation of α' whereas manganese, silicon and molybdenum did not influence the formation of α' . Miller *et al.* [122] and Brown and Smith [123] also have reported similar results.

Mateo *et al.* [124] studied the G-phase precipitation in detail in an AISI 329 grade of DSS and observed an incubation time from the completion of spinodal decomposition to the nucleation of G-phase. After 200 hours aging treatment at 475°C, they observed very fine spots in TEM bright field image. The uniformly distributed G phase particles in the grain body were observed only after 15000 hours of aging at 475°C. This indicates that the possibility of G-phase precipitation in the ferritic phase requires long duration aging treatment at 475°C. Moreover, studies on the mechanisms of precipitation have resulted in modifications of the alloy compositions to completely eliminate the precipitation of secondary carbides and G-phase [124]. From these investigations formation of G-phase is a remote possibility in case of the presently investigated grade of DSS. The carbide and nitride precipitates are mostly observed at grain boundaries [88-89].

Considering all the possibilities and the facts that

- there was no mottling observed in the ferritic grain,
 - the needle like precipitates were observed through out the grain body, and
 - the specimen were observed after 100 hours of aging (saturation),
- the precipitates considered to be likely the needles of α' .

5.2 Low cycle fatigue behaviour of DSS

The factors, which are known to influence the fatigue behaviour of DSS, are:

- alloy composition [39-41],
- volume fraction of ferrite [44-45,88-89],
- processing route (cast and wrought) [88-89] and
- texture [125].

Some of the above mentioned factors are also known to have pronounced effects on the change in cyclic stress-strain behaviour and fatigue life of DSS due to an aging treatment at 475°C. So a discussion on the change in low cycle fatigue behaviour of DSS due to aging treatment at 475°C must be done in conjunction with the above-mentioned factors. For example, Llanes *et al.* [111] observed a ferrite-like deformation mechanism and a fatigue softening at $\Delta\varepsilon_{pl}/2 = 1.2 \times 10^{-3}$ for the AISI 329 grade of DSS in the aged condition (0.074 wt.% nitrogen, 38% γ and 62% α , wrought), while Vogt *et al.* [44] for their alloy B6A920 grade of DSS (0.4 wt.% nitrogen, 70% γ and 30% α , wrought) observed no change in fatigue resistance even at $\Delta\varepsilon_{pl}/2 = 5.3 \times 10^{-3}$ after aging treatment at 475°C. This difference may be attributed to several factors such as nitrogen content and ferrite volume fraction.

DSS are undergoing continuous evolution to newer grades primarily based on adjusting the chemical composition. The most important modification is the increase in nitrogen content. Nitrogen affects the cyclic stress-strain behaviour and fatigue life of DSS [39-41] since it stabilizes and strengthens the austenite by solid solution strengthening. A stronger austenitic phase results in a need for a higher plastic strain contribution of the ferritic phase. The response of the ferritic phase to this modified strain partitioning is different in the annealed and aged condition. Moreover, nitrogen was also found to establish short-range order of chromium in δ -ferrite [126]. Some of the grades of DSS used for studies on fatigue behaviour are mentioned in Table 5.1 listing the nitrogen content.

Table 5.1: Different commercial grades of DSS used for studying the fatigue behaviour.

Grades	Nitrogen content, wt.%	Reference
AISI 329	0.0072	[111]
SAF 2205	0.15	[30]
DIN W Nr. 1.4462	0.17	[37]
SAF 2507	0.24	[112, 125, 127]
A905	0.35	
BöA920	0.4	[44]

Nitrogen addition is thought to be beneficial for the fatigue life of the material. However, Akdut [39] observed that contrary to single-phase austenitic stainless steels only increasing the nitrogen content in DSS did not increase fatigue life, but nitrogen in combination with the morphological scale and anisotropy apparently altered the cyclic stress strain curve. This means the beneficial effect of nitrogen on fatigue behaviour can be realized only with certain morphology. The conventional concept of microstructural barrier in single-phase materials sometime does not explain the low cycle fatigue behaviour adequately. Stolarz and Foct [121] described that the physical properties and the degree of plastic deformation in the neighbouring grain or particle determine the resistance of a barrier. Girones *et al.* [125] studied the influence of texture on the surface damage mechanisms developed in cyclically loaded aged DSS. The rolling or recrystallisation texture is known to determine the local crystallographic orientation and this in turn influences the evolution and growth of surface damage. Alvarez-Armas *et al.* [127] observed that the most important feature of the dislocation structure developed just beneath the surface of the fatigued specimen corresponds to the intense shear bands oriented in the direction of the shear plane crossing grains and phases when the K-S relationship is satisfied [127]. This observation further strengthens the studies made by Girones *et al.* [125] on the indirect influence of texture on fatigue damage.

5.2.1 Cyclic hardening/softening behaviour

Goh and Yip [128] conducted plastic strain controlled fatigue test ($\Delta\varepsilon_{pl}/2 = 2 \times 10^{-4}$ to 8×10^{-2}) with SAF 2507 grade of DSS and observed a common trend of cyclic hardening/softening for all the imposed values of $\Delta\varepsilon_{pl}/2$. The initial rapid cyclic hardening in case of the material investigated in [128] was followed by cyclic softening and final cyclic saturation. In

agreement with the present investigation they observed notable amount of cyclic softening only when σ/σ_{ys} ratio was above 0.8.

Alvarez-Armas *et al.* [127] conducted total strain controlled fatigue tests ($\Delta\varepsilon/2 = 3.5 \times 10^{-3}$, 4.0×10^{-3} , 5.0×10^{-3} , 8.5×10^{-3} and 9.5×10^{-3}) of SAF 2507 grade of super DSS containing 0.236 wt.% nitrogen. The evolution of stress amplitude with number of cycles for the tests conducted in [127] is shown in Fig. 5.3. The cyclic hardening softening response is categorized into three well-defined plastic strain regions. At plastic strain ranges between 7.5×10^{-4} and 2.5×10^{-3} long softening is followed by a long saturation stage, while between 4.0×10^{-3} and 6.0×10^{-3} , a small initial cyclic hardening followed by a continuous softening stage characterize these strains. Lastly, between 8.5×10^{-3} and 1.25×10^{-2} , an important initial cyclic hardening followed by a pronounced softening stage, which turned into a nearly saturation stage near the end of the fatigue life, defined this interval of strains. In the present investigation on annealed material also similar discernible stages were observed. However, such a clear demarcation in terms of plastic strain amplitude requires much more experiments.

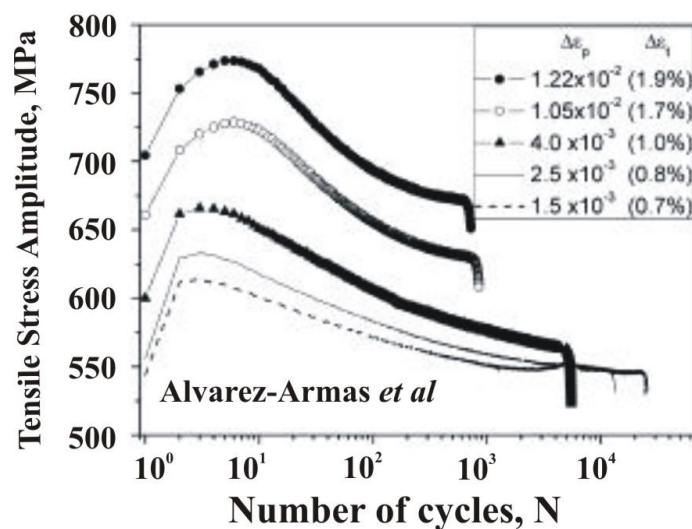


Fig. 5.3: Evolution of the stress amplitude with the number of cycles of SAF 2507 DSS for different plastic strain ranges [127].

Vogt *et al.* [44] conducted strain controlled fatigue tests on two grades of DSS designated UR52N+ and B6A920 having nitrogen contents 0.24 and 0.4 wt.%, respectively,

with $\Delta\varepsilon/2$ values of 4.0×10^{-3} and 1.0×10^{-2} in the annealed and aged condition (aged at 475°C for 200 hours). The cyclic hardening/softening curves for the tests conducted in [44] are shown in Fig. 5.4. At lower and higher values $\Delta\varepsilon/2$ they obtained similar cyclic hardening/softening curves. This is consistent with the results obtained in the present investigation at $\Delta\varepsilon/2 = 4 \times 10^{-3}$. However, at $\Delta\varepsilon/2 = 1.0 \times 10^{-2}$ the alloy investigated in the present study had a relatively rapid softening compared to the alloy investigated in [44]. The alloy with high nitrogen content has higher fatigue resistance. They also observed slightly higher initial stress level for the alloy containing higher nitrogen. However, both have almost same values of saturation stress σ_s , i.e. 535 and 532 MPa for low and high values of nitrogen content, and the saturation stress value at this strain amplitude obtained in the present investigation is 507 MPa. Even though a direct comparison between the alloys tested in [44] and the alloy of the present investigation cannot be made in case of B \ddot{o} A920, which has a ferrite content of only 30%, however, the results can be compared for the alloy containing 0.24 wt.% nitrogen.

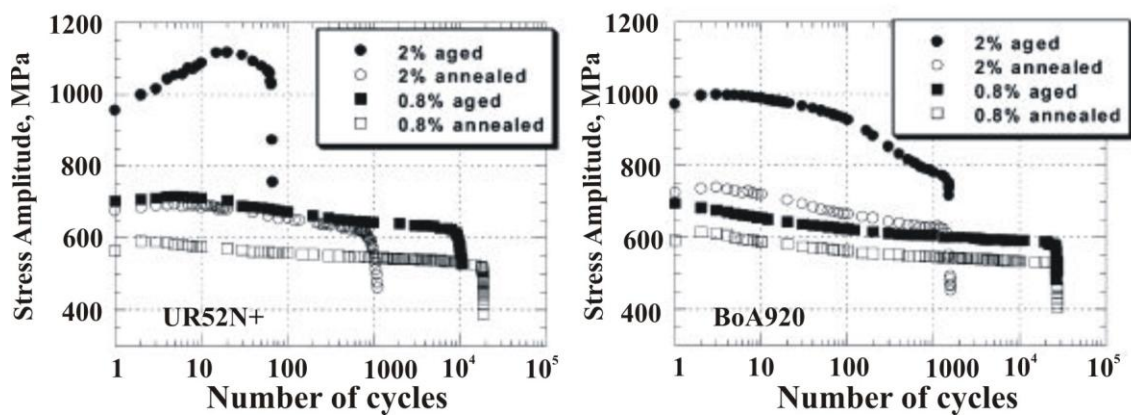


Fig. 5.4: Evolution of the stress amplitude versus the number of cycles for the UR52N+ and for the B \ddot{o} A920 in the annealed and aged conditions [44].

The aging treatment at 475°C did not affect the fatigue resistance, which even seems to be improved at low strain amplitude for the alloy investigated by Vogt *et al.* [44]. The aging treatment resulted in a strong increase of the stress levels for both alloys at low and high strain amplitudes. At $\Delta\varepsilon/2 = 4 \times 10^{-3}$ the curves are only shifted upwards for 100 MPa (UR52N+) and for 70 MPa higher (B \ddot{o} A920), but their qualitative course is similar to that

usually reported for as-quenched DSS (slight hardening followed by a softening and a stabilization of the stress amplitude). However, the fatigue behaviour of the aged material significantly differed from that of the annealed ones for the tests conducted at $\Delta\varepsilon/2 = 1.0 \times 10^{-2}$, i.e. at high plastic strain amplitude. In the case of the UR52N+ steel, the initial hardening is very pronounced. On the contrary, the B6A920 steel did not exhibit such a pronounced hardening and exhibits a stronger softening at high strain during about 70% of the fatigue life. The most surprising and interesting fact is the occurrence (UR52N+) and absence (B6A920) of sensitivity of fatigue resistance to aging.

Llanes *et al.* [111] studied the hardening/softening response of an AISI 329 grade of DSS in the annealed ($\Delta\varepsilon/2$ values 2.0×10^{-3} , 3.0×10^{-3} and 4.0×10^{-3}) and two aged conditions. The evolution of stress amplitude with number of cycles for the tests conducted in [111] is shown in Fig. 5.5. One set of specimen was aged at 475°C for 25 hours ($\Delta\varepsilon/2$ values 3.0×10^{-3} and 6.0×10^{-3}) and another set of specimens were aged 475°C for 200 hours ($\Delta\varepsilon/2$ values 4.5×10^{-3} and 6.0×10^{-3}). Hardening was observed in the first few cycles. At low and intermediate $\Delta\varepsilon_{pl}/2$, such hardening was followed by either slight and rapid (low $\Delta\varepsilon_{pl}/2$) or gradual (intermediate $\Delta\varepsilon_{pl}/2$) softening. At both $\Delta\varepsilon_{pl}/2$ values a steady state of saturation was finally attained. At large $\Delta\varepsilon_{pl}/2$ annealed and aged specimens experienced after hardening a continuous softening, till fracture. This softening behavior was much more pronounced in the aged materials than in the annealed steel. Similar hardening-softening responses were found in aged materials at large values of $\Delta\varepsilon_{pl}/2$ in spinodally decomposed high chromium ferritic stainless steels subjected to LCF [129]. Kwon *et al.* [130] observed significant cyclic softening in the initial stage of the fatigue experiment, especially, at the large strain amplitude for a cast grade of DSS aged at 475°C.

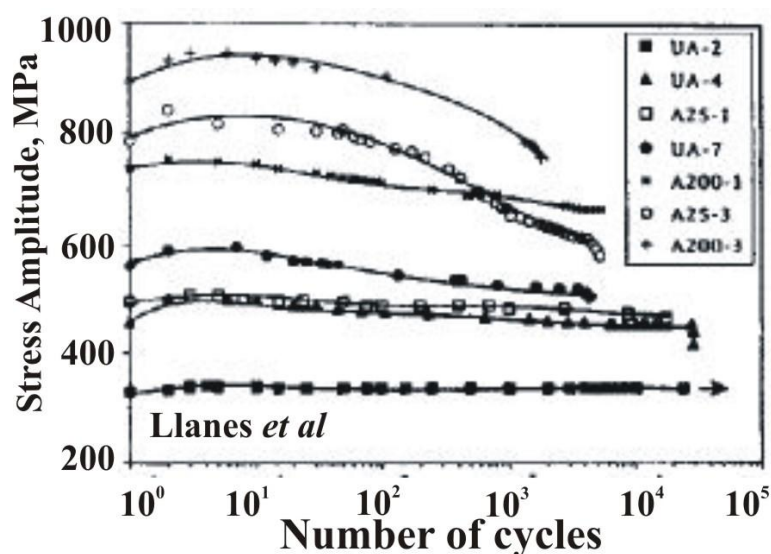


Fig. 5.5: Cyclic hardening-softening response of unaged (UA) and aged (A25, A200) duplex stainless steel under conventional strain control testing conditions. Applied total strain amplitude and the corresponding saturation or half-life stress and plastic strain amplitude values, for each of the presented specimens, are given in Table 5.2 [111].

Table 5.2: Testing conditions and corresponding saturation or half-life stress and strain values for specimens shown in Fig. 5.5. UA: unaged; A25 and A200: aged at 475°C for 25 and 200 hours respectively [111]

Specimens	Applied $\Delta\varepsilon$	Saturation or half-life σ_a (MPa)	Saturation or half-life $\Delta\varepsilon_{pl}$
UA-2	2.0×10^{-3}	336	1.1×10^{-4}
UA-4	3.0×10^{-3}	450	3.0×10^{-4}
A25-1	3.0×10^{-3}	464	2.8×10^{-4}
UA-7	4.0×10^{-3}	525	1.1×10^{-3}
A200-1	4.5×10^{-3}	665	5.0×10^{-4}
A25-3	6.0×10^{-3}	656	1.3×10^{-3}
A200-3	6.5×10^{-3}	790	1.2×10^{-3}

5.2.2 Cyclic stress-strain curve

The CSSC plotted by Magnin and Lardon [131] for DSS consists of two separate stages. The transition point was identified at $\Delta\varepsilon_{pl}/2 = 1.0 \times 10^{-3}$. The curve changes from a high strain-hardening rate in the first regime to a lower strain-hardening rate in the second regime

Llanes *et al.* [111] have described the cyclic stress-strain response of DSS in the annealed and aged conditions in three stages in terms of plastic strain amplitudes ($\Delta\varepsilon_{pl}/2 <$

10^{-4} , $10^{-4} < \Delta\varepsilon_{pl}/2 < 10^{-3}$, $\Delta\varepsilon_{pl}/2 > 10^{-3}$) each amenable to be characterized by well-defined and distinct cyclic deformation mechanisms. The range of plastic strain amplitudes in the present investigation lies in the third stage and the cyclic stress-strain response in the present investigation is in well agreement with this third stage.

Goh and Yip [128] identified two separate regimes with different strain-hardening rates in the CSSC. The first regime, at $\Delta\varepsilon_{pl}/2 < 7 \times 10^{-3}$, had a high cyclic strain-hardening rate, while the second regime, at $\Delta\varepsilon_{pl}/2 > 7 \times 10^{-3}$, had a strain-hardening rate that is less pronounced than the first.

5.2.3 Cyclic life

Magnin and Lardon [131] detected a change of slope of the Coffin-Manson curves of DSS at $\Delta\varepsilon_{pl}/2$ value of 1.0×10^{-3} . However, in the present investigation the $\Delta\varepsilon_{pl}/2$ values realized from the range of employed total strain amplitude are above this critical value and moreover no slope change was observed. Mateo *et al.* [112] conducted experiments in an extended range of plastic strain amplitude ($2.9 \times 10^{-5} < \Delta\varepsilon_{pl}/2 < 6.6 \times 10^{-3}$) and the Coffin-Manson curve in their case is subdivided into three regimes: stage I, $\Delta\varepsilon_{pl}/2 < 1.0 \times 10^{-4}$ with austenite like behaviour; stage II, $1.0 \times 10^{-4} < \Delta\varepsilon_{pl}/2 < 6.0 \times 10^{-4}$ with mixed austenite-ferrite like response; stage III, $\Delta\varepsilon_{pl}/2 > 6.0 \times 10^{-4}$ with pure ferrite like behaviour. In the light of their study the presently investigated DSS grade is falling in the stage III and has a ferrite like behaviour. But the above works were reported for DSS grades containing 0.07 wt.% nitrogen. The multiple factors that can affect the fatigue life can be realized from the studies conducted by Akdut [39], who studied the phase morphology and fatigue life of nitrogen alloyed duplex stainless steels and observed that the fatigue lives of DSS were influenced by numerous parameters such as processing history and chemical composition and, thus by morphological anisotropy, morphological scale and nitrogen content. He showed that increasing morphological anisotropy and decreasing morphological scale have an increasing effect on the fatigue life of DSS. He also postulated the dependence of fatigue life on crystallographic texture. Contrary to single phase austenitic stainless steels, increasing the nitrogen content in DSS did not appear to increase the fatigue life. However, nitrogen in combination with the

morphological scale and anisotropy apparently alters the extent of each of the three regime proposed by Mateo *et al* [112].

Kwon *et al.* [130] also obtained such linearized plots in their investigation on CF8M cast grade of DSS. The Coffin Manson curve is plotted but not discussed by Vogt *et al.* [44]. However, from their plot it appears that the fatigue life is decreased as a result of aging treatment of the alloy with low nitrogen content for the range of strain amplitude investigated. The fatigue life in the aged conditions appears to be approaching the fatigue life in the annealed condition as the strain amplitude was decreased. Whereas, aging treatment at 475°C seems to have no or very little effect on the fatigue life of the alloy with high nitrogen content.

5.3 Fatigue crack initiation behaviour in DSS embrittled at 475°C

The difference in the elastoplastic properties between the two phases in DSS affects the amount of plastic deformation occurring in the austenite and ferrite phases. As a consequence, the plastic strain localization and the fatigue crack initiation behaviour are affected. Taisne *et al.* [132] observed in a recent study on the role of interfaces in fatigue deformation mechanism in DSS bicrystals that not only interphase interface geometry and elasticity impose the dislocation transmission process, but the presence of interface modifies the response of each crystal to the mechanical solicitation. Alvarez-Armas *et al.* [40] observed that the efficiency of the coupling between phases seems to play an important role in the crack formation process. Stolarz and Focit [121] observed in their study on specific features of two-phase alloy response to cyclic deformation that the short crack initiation sites (brittle or ductile phase, interfaces), the cyclic damage mode (single or multiple cracking) and consequently the fatigue life depend both on morphological and topological parameters of the microstructure and on the difference on the mechanical properties of constitutive phases.

Krupp *et al.* [133] have shown that fatigue crack initiation and growth rate of short crack during high-cycle fatigue of an austenitic-ferritic duplex steel is determined by the local microstructural features such as crystallographic orientation, morphology and size of grains

and phase patches, as well as the structure of the grain and phase boundaries. Fig. 4.31 is a clear revelation of the dependence of short crack propagation on microstructural feature such as topology.

Düber *et al.* [134] showed in a recent investigation on the same grade of DSS that crack propagation in the short crack regime can be subdivided into two basic mechanisms: operating either by single-slip (crystallographic propagation) and double-slip (alternating propagation on two slip planes) as shown in Fig. 5.6, giving rise to substantially different propagation rates. Additionally, it was found that a crack, which has grown in double slip, can change back to the single slip mechanism again, when entering a new grain and no adequate second slip plane is available. It is reported that the $\alpha\gamma$ phase boundary offers more resistance to slip transfer as compared to $\alpha\alpha$ and $\gamma\gamma$ grain boundaries.

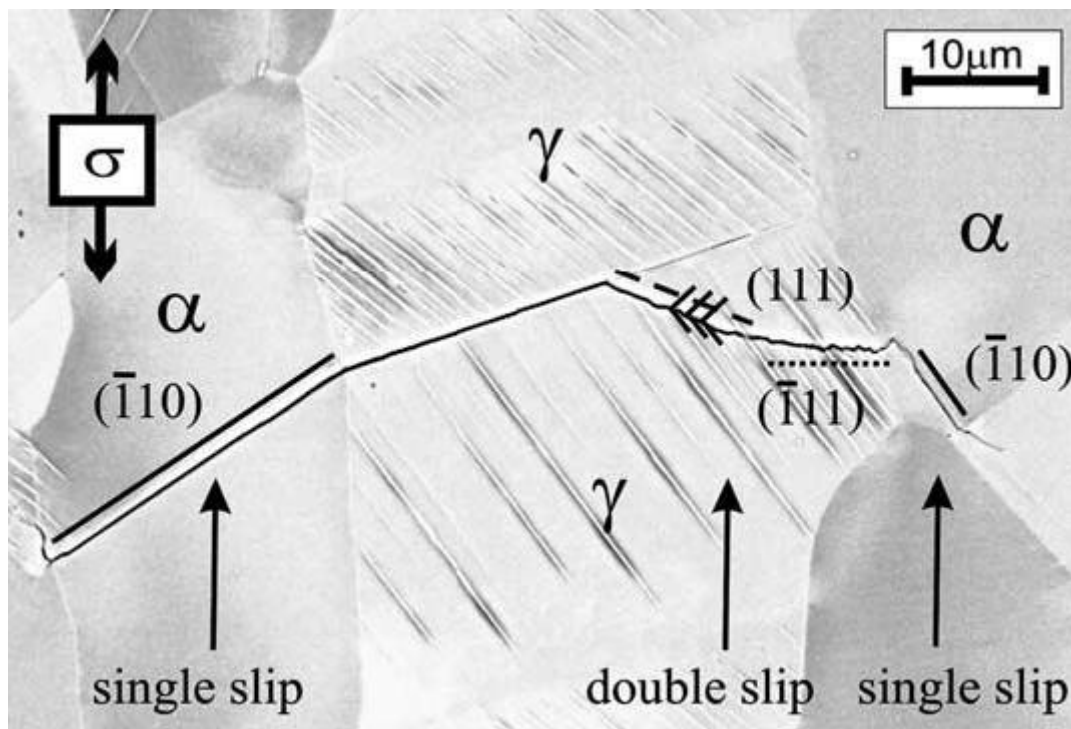


Fig. 5.6: Paths of short cracks at $\Delta\sigma/2 = 370$ MPa, $N = 160.000$ [134].

Lillbacka *et al.* [135] conducted cyclic experiments on two different grades of super DSS, UNS S32750 and UNS S32906. The UNS S32750 grade of DSS was studied in as-delivered (2507AD) and as-aged (475°C/4 hours) (2507HT) condition and UNS S32906 was

studied only in the as-delivered (2906AD) condition. The cyclic stress-strain behavior of DSS is largely dependent on the applied load/strain amplitude. The difference in the elastoplastic properties between the austenite and ferrite phases as well as the load sharing between the phases, are responsible for the dependence. In the 2507AD steel, the slip bands concentrate in the ferrite phase although some small parts of the austenite phase also show slip bands. In the heat-treated steel 2507HT, the slip bands again occur in the ferrite, although compared with the 2507AD steel larger parts of the austenite phase also show slip bands. This indicates that since the ferritic phase in 2507 HT is hard compared to 2507 AD due to the aging treatment at 475°C and more plastic strain is partitioned to the austenitic phase in case of 2507 HT. In the presently investigated grade of DSS the plastic strain was exclusively localised to the austenitic phase due to a harder ferritic phase. The 2906AD steel shows slip bands almost exclusively in the ferrite phase. The appearance of the slip bands in the ferritic phase can be attributed to a stronger austenitic phase in case of the DSS grade investigated in [135] due to higher nitrogen content compared to the presently investigated grade of DSS.

Chapter 6 Conclusions and future aspects

The 475°C aging treatment results in an embrittlement of the ferritic phase [26-29]. When this was detected for the first time in ferritic stainless steels the term embrittlement referred to as change from ductile to brittle failure [92-93]. So this term per se is understood to express a detrimental effect to mechanical properties. This holds true for the mechanical behaviour such as tensile and impact. However, under fatigue loading conditions the term embrittlement need not necessarily be detrimental. This is because a multitude of parameters defining the fatigue loading condition, such as stress/strain amplitude, load ratio, frequency, may interact differently with the microstructure that results from the aging treatment. Furthermore, the so-called embrittled microstructure may be beneficial for some aspects of fatigue features under some combination of cyclic load parameters. The argument will be clear from the ensuing concluding remarks.

The results from the study of the aging treatment at 475°C by electron microscopy and routine mechanical tests leads to the following conclusions:

- The aging treatment at 475°C results in the precipitation of α' in the ferritic phase.
- The impact energy of DSS drops from 260 Joules in the annealed condition to 8 Joules after aging treatment at 475°C for 100 hours. The drop in impact energy value is attributed to the inability of the ferritic phase to form deformation twins in the aged condition. This was confirmed from the TEM examination.

The results from the study of the low cycle fatigue behaviour of a duplex stainless steel in the annealed and aged condition by mechanical testing and electron microscopic examinations lead to the following conclusions:

- The deformation curves in the annealed condition have three discernible stages: (i) cyclic hardening, (ii) cyclic softening, and (iii) cyclic saturation. In the aged condition two discernible stages were observed: (i) cyclic hardening, and (ii) cyclic softening till final failure for all values of strain amplitudes. The life span of each of the above stages was observed to be a function of strain amplitude both in annealed and aged condition, e.g. (i)

a prolonged cyclic saturation was observed at $\Delta\varepsilon/2 = 4.0 \times 10^{-3}$ and the period of cyclic saturation decreased with increase in strain amplitude in the annealed condition, (ii) cyclic softening was gradual at $\Delta\varepsilon/2 = 4.0 \times 10^{-3}$, 6.0×10^{-3} and 8.0×10^{-3} , whereas rapid softening was observed for $\Delta\varepsilon/2 = 1.0 \times 10^{-2}$, and (iii) cyclic softening was rapid with increase in the value of strain amplitude in the aged condition.

- The cyclic stress strain curve is sensitive to the heat treatment condition in the investigated range of plastic strain amplitude. The relative increase in stress amplitude with plastic strain amplitude is more pronounced at higher values of plastic strain amplitudes. This is an expected behaviour due to the increase in strength of the ferritic phase as a result of aging treatment. A change in slope is observed in the cyclic stress-strain curve in the aged condition as compared to the standard heat treated condition.
- In the range of strain amplitude employed, in the aged condition, fatigue life of the DSS studied is longer at lower strain amplitudes, decreases and becomes similar at intermediate strain amplitudes and becomes shorter at the higher strain amplitudes in comparison to the standard heat treated condition. Different slopes are obtained for annealed and aged condition in the Coffin-Manson plot. The slope is steeper in the annealed condition compared to the aged condition, which indicates that the fatigue life is better in the aged condition at lower values of plastic strain amplitudes and better in the annealed condition at a higher value of plastic strain amplitude.
- Dislocation bundles, dislocation pile-ups and cell structures were observed in the ferritic phase of the DSS in the annealed condition at $\Delta\varepsilon/2 = 8.0 \times 10^{-3}$. However, in the aged condition the disappearance of needle-shaped α' precipitates and coalescence of the arrays of precipitates were the main reasons of rapid cyclic softening. A striking difference was the absence of any dislocation spatial arrangement as was observed in the annealed condition. The austenitic phase had planar arrays of dislocation observed in the annealed condition. However, beginning of cell formation was observed in the aged condition due to higher stress levels at $\Delta\varepsilon/2 = 8.0 \times 10^{-3}$.

The results obtained from the study of fatigue crack initiation behaviour in the embrittled condition by interrupted stress-controlled fatigue test, in order to identify the crack initiation

sites and relate these to the crystallographic parameters obtained from EBSD-OIM scans, leads to the following conclusions:

- The crack initiation sites are the slip markings corresponding to $\{111\}$ plane traces in the austenitic grains at $\Delta\sigma/2 = 400$ MPa.
- More cracks were observed to initiate at $\Sigma 3$ CSL boundary in the austenitic grain at $\Delta\sigma/2 = 500$ MPa.
- The major resistance to growth of these cracks comes from the $\alpha\gamma$ phase boundary.

From the concluding remarks on the influence of aging treatment at 475°C on the fatigue behaviour of the DSS studied, it can be seen that at lower values of stress/strain amplitude a better fatigue life is realized in the aged condition. This clearly shows that this aging treatment is beneficial for high cycle fatigue conditions. Conversely, at higher values of stress/strain amplitude the fatigue life deteriorates. At some value of strain amplitude during strain-controlled fatigue test, the fatigue life in the aged condition approached the fatigue life in the annealed condition. The exact value of this point of cross-over depends on factors such as alloy composition and crystallographic parameters. In the presently investigated grade of DSS this value is $\Delta\varepsilon/2 = 8.0 \times 10^{-3}$.

Some gap areas of immediate future research could be:

- A comprehensive study of the influence of alloying elements on thermodynamics and kinetics of aging in the ferritic phase of wrought grades of laboratory melt DSS is a very essential first step. In the initial phase the partitioning of alloying elements to ferrite and austenite is to be determined for different melts. A suitable mechanical property, which is significantly influenced by this aging treatment, such as impact energy, may be used as a monitor to assess the degree of embrittlement.
- From the low cycle fatigue experiments it was established that fatigue life is higher in the aged condition at lower values of strain amplitude. From stress-controlled fatigue experiments it is observed that crack initiation mostly occurs in the surface slip markings of austenitic grains. The reason for the slow growth of these short cracks come from the $\alpha\gamma$ phase boundary and a stronger ferritic phase resulting from aging treatment, This

means fatigue life will be higher by increasing the phase boundary area. Therefore, the effect of the initial grain size on the fatigue life in the aged condition would be a study of research significance.

References

- [1] W.A.J. Albert, Über Treibseile am Harz, *Archive für Mineralogie Geognosie Bergbau und Hüttenkunde* 10 (1838) 215-234.
- [2] A. Wöhler, Versuche über die Festigkeit der Eisenbahnwagenachsen, *Zeitschrift für Bauwesen* 10 (1860), English summary, *Engineering* 4 (1867) 160-161.
- [3] T. Anderson, *Fracture Mechanics: Fundamentals and Applications* (1994), CRC Press, Boca Raton, FL.
- [4] P.C. Paris, F.A. Erdogan, Critical analysis of crack propagation laws, *Journal of Basic Engineering* 85 (1963) 528-534.
- [5] J.A. Ewing, W. Rosenhain, Experiments in micro-metallurgy:-Effects of strain. Preliminary notice, *Philosophical Transactions of the Royal Society, London* A200 (1903) 241-250.
- [6] H. Mughrabi, The cyclic hardening and saturation behaviour of copper single crystals, *Material Science and Engineering* 33 (1978) 207-223.
- [7] L.L. Lisiecki, J.R. Weertman, Orientation effects on the elevated temperature fatigue of copper single crystals, *Acta Metallurgica et Materialia* 38 (1990) 509-519.
- [8] Z.S. Basinski, A.S. Korbel, S.J. Basinski, The temperature dependence of the saturation stress and dislocation substructure in fatigued copper single crystals, *Acta Metallurgica* 28 (1980) 191-207.
- [9] H. Mughrabi, F. Ackermann, K. Herz, Persistent slip bands in fatigued face centered and body centered cubic metals, In *Fatigue Mechanisms*, ASTM STP 675 (1979) 69-105.
- [10] J. Bretschneider, C. Holste, B. Tippelt, Cyclic plasticity of nickel single crystals at elevated temperatures, *Acta Materialia* 45 (1997) 3775-3783.
- [11] L. Llanes, A.D. Rollett, C. Laird, J.L. Bassani, Effect of grain size and annealing texture on the cyclic response and the substructure evolution of polycrystalline copper, *Acta Metallurgica et Materialia* 41 (1993) 2667-2679.
- [12] P. Peralta, L. Llanes, A. Czapka, C. Laird, Effect of texture and grain size as independent factors in the cyclic behavior of polycrystalline copper, *Scripta Metallurgica et Materialia* 32 (1995) 1877-1881.
- [13] C.E. Feltner, C. Laird, Cyclic stress-strain response of F.C.C. metals and alloys—I Phenomenological experiments, *Acta Metallurgica* 15 (1967) 1621-1632.

- [14] C.E. Feltner, C. Laird, Cyclic stress-strain response of F.C.C. metals and alloys—II Dislocation structures and mechanisms, *Acta Metallurgica* 15 (1967) 1633-1653.
- [15] S. Brett, R.D. Doherty, Loss of solute at the fracture surface in fatigued aluminium precipitation-hardened alloys, *Materials Science and Engineering* 32 (1978) 255-265.
- [16] C. Calabrese, C. Laird, Cyclic stress-strain response of two-phase alloys Part I. Microstructures containing particles penetrable by dislocations, *Materials Science and Engineering* 13 (1974) 141-157.
- [17] C. Calabrese, C. Laird, Cyclic stress-strain response of two-phase alloys Part II. Particles not penetrated by dislocations, *Materials Science and Engineering* 13 (1974) 159-174.
- [18] T. Ishihara, Microstructural effects of fatigue crack growth in a two-phase steel, *Journal of Materials Science* 18 (1983) 103-108.
- [19] K. Cho, J. Gurland, The law of mixtures applied to the plastic deformation of two-phase alloys of coarse microstructures, *Metallurgical and Materials Transactions A* 19 (1988) 2027-2040.
- [20] T. Wada, S. Hashimoto, Fatigue crack growth across the interphase boundaries in two-phase bicrystals, *Materials Science Forum* 294-196 (1999) 693-696.
- [21] H. Sakasegawa, T. Hirose, A. Kohyama, Y. Katoh, T. Harada, K. Asakura, Microstructural stability of reduced activation ferritic/martensitic steels under high temperature and stress cycling. *Fusion Engineering and Design* 61-62 (2002) 671-675.
- [22] N. Giel, Application of duplex stainless steel in the chemical process industry, *Proc. 5th World Duplex Stainless Steel Conference 1997*, Maastricht, The Netherlands, KCI Publishing D97-201 (1997) 9-16.
- [23] L. Smith, A guideline to the successful use of duplex stainless steels for flowlines. *Proc. Duplex America Conference*, Houston, USA, KCI Publishing DA_2-102 (2000) 17-29.
- [24] N. Johan, Digesters and pulp storage towers of duplex stainless steels-saving weight and costs, *ACOM, Avesta Sheffield AB* 3 (1994) 1-8.
- [25] T. Alpo, Increased usage of duplex materials in manufacturing of pulping equipment, *Proc. Duplex America Conference*, Houston, USA, KCI Publishing DA2_061 (2000) 401-408.
- [26] P.J. Grobner, The 885°F (475°C) embrittlement of ferritic stainless steel, *Metall Trans* 4 (1973) 251-260.

- [27] D. Chandra, L.H. Schwartz, Mössbauer effect study of the 475°C decomposition of Fe-Cr, *Metall Trans 2* (1971) 511-519.
- [28] M.B. Cortie, H. Pollak, Embrittlement and aging at 475°C in an experimental ferritic Stainless Steel Containing 38 wt.% chromium, *Materials Science and Engineering A* 199 (1995) 153-163.
- [29] H.D. Solomon, L.M. Levinson, Mössbauer effect study of '475°C embrittlement' of duplex and ferritic stainless steels, *Acta Metallurgica* 26 (1978) 429-442.
- [30] K.L. Weng, H.R. Chen, J.R. Yang, The low-temperature aging embrittlement in a 2205 duplex stainless steel, *Materials Science and Engineering A* 379 (2004) 119-132.
- [31] M.M. Schwartz, *Emerging Engineering Materials: Design, Processes, Applications* (1996), CRC Press.
- [32] L. Weber, P.J. Uggowitzer, Partitioning of chromium and molybdenum in super duplex stainless steels with respect to nitrogen and nickel content, *Materials Science and Engineering A* 242 (1998) 222-229.
- [33] *Handbook of Mechanical Alloy Design* (2004) (Ed.: E. Totten, L. Xie, K. Funatani) CRC Press.
- [34] M. Nyström, Plastic deformation of duplex stainless steels, Ph.D. thesis (1995), Chalmers University of Technology, Göteborg, Sweden.
- [35] O. Smuk, Microstructure and properties of modern P/M super duplex stainless steel, Doctoral thesis (2004), Royal Institute of Technology, Stockholm, Sweden.
- [36] H. Sieurin, Fracture toughness properties of duplex stainless steel, Doctoral thesis (2006), Royal Institute of Technology, Stockholm, Sweden.
- [37] O. Düber O. Untersuchungen zum Ausbreitungsverhalten mikrostrukturell kurzer Ermüdungsrisse in zweiphasigen metallischen Werkstoffen am Beispiel eines austenitisch-ferritischen Duplexstahls. Dissertation (2007), Universität Siegen, Germany.
- [38] T.H. Kang, D.M. Li, Y.D. Lee, C.S. Lee, Alloying and aging effects on the fatigue crack growth of duplex stainless steels, *Materials Science and Engineering A* 251 (1998) 192-199.
- [39] N. Akdut, Phase morphology and fatigue lives of nitrogen alloyed duplex stainless steels, *International Journal of Fatigue* 21 (1999) 97-103.

- [40] I. Alvarez-Armas, M.C. Marinelli, J.A. Malarria, S. Degallaix, A.F. Armas, Microstructure associated with crack initiation during low cycle fatigue in a low nitrogen duplex stainless steel, *International Journal of Fatigue* 29 (2007) 758-764.
- [41] T. Takemoto, K. Mukai, K. Hoshini, Effect of nitrogen on low cycle fatigue behaviour of austenitic stainless steel, *Transactions ISIJ* 26 (1986) 337-344.
- [42] T. Kruml, J. Polak, K. Obrtlík, S. Degallaix, Dislocation structures in the bands of localized cyclic plastic strain in austenitic 316L and austenitic-ferritic duplex stainless steels, *Acta Mater* 45 (1997) 5145-5151.
- [43] M. Nyström, B. Karlsson, Fatigue of duplex stainless steel; Influence of discontinuous spinodally decomposed ferrite, *Material Science and Engineering A* 215 (1996) 26-38.
- [44] J.-B. Vogt, K. Massol, J. Foct, Role of the microstructure on fatigue properties of 475°C aged duplex stainless steels, *International Journal of Fatigue* 24 (2002) 627-633.
- [45] Assessment and Management of Ageing of Major Nuclear Power Plant Components Important to Safety; Primary Piping in PWRs, Technical Report of International Atomic Energy Agency, IAEA-TECDOC, 1361 (July 2003).
- [46] S. Suresh, *Fatigue of materials*, 2nd Edition (1998), Cambridge University Press.
- [47] A. Weroniski, T. Hejwowski, *Thermal fatigue of metals* (1991), CRC Press.
- [48] S. Baik, R. Raj, Mechanisms of creep-fatigue interaction, *Metallurgical and Materials Transactions A* 13 (1982) 1215-1221.
- [49] H.-J. Christ, A. Jung, H.J. Maier, R. Teteruk, Thermomechanical Fatigue-Damage Mechanisms and Mechanisms-Based Life Prediction Methods. *SADHANA* 28 (2003) 147-165.
- [50] R.P. Wei, G. Shim, Fracture mechanics and corrosion fatigue. *Corrosion fatigue Mechanics, Metallurgy, Electrochemistry and Engineering* (Ed.: T.W. Crooker, B.N. Leis), ASTM STP 801 (1983) 5-25.
- [51] D.F. Cannon, H. Pradier, Rail rolling contact fatigue research by the European Rail Research Institute, *Wear* 191 (1996) 1-13.
- [52] Fretting fatigue: Advances in the basic understanding and applications (Ed.: Y. Mutoh, D.W. Hoepfner, S.E. Kinyon) ASTM STP 1425 (2003).
- [53] A.N. Gulluoglu, C.S. Hartley, Simulation of dislocation microstructures in two dimensions II: Dynamic and relaxed structures. *Modelling Simul. Mater. Sci. Eng.* 1 (1993) 383-402.

- [54] P. Neumann, Dislocation Dynamics in Fatigue, *Physica Scripta T 19* (1987) 537-543.
- [55] W.F. Smith, J. Hashemi, *Foundations for Materials Science and Engineering* (2004), McGraw Hill Professional.
- [56] R.J. Amodeo, N.M. Ghoniem, Dislocation dynamics I: A proposed methodology for deformation micromechanics, *Physical Review B 41* (1990) 6958-6967.
- [57] R.J. Amodeo, N.M. Ghoniem, Dislocation dynamics II: Application to the formation of persistent slip bands, planar arrays, and dislocation cells, *Physical Review B 41* (1990) 6968-6976.
- [58] U Essmann, H. Mughrabi, Annihilation of dislocations during tensile and cyclic deformation and limits of dislocation densities, *Philosophical Magazine A 40* (1979) 731-756.
- [59] U. Essmann, M. Rapp, Slip in copper crystals following weak neutron bombardment, *Acta Metallurgica 21* (1973) 1305-1317.
- [60] S. Catalao, X. Feugas, Ph. Pilvin, M.-Th. Cabrillat, Dipole heights in cyclically deformed polycrystalline AISI 316L stainless steel, *Materials Science and Engineering A 400-401* (2005) 349-352.
- [61] H. Neuhäuser, O.B. Arkan, H.-H. Potthoff, Dislocation multipoles and estimation of frictional stress in f.c.c. copper alloys, *Materials Science and Engineering 81* (1986) 201-209.
- [62] F. Prinz, A.S. Argon, Dislocation cell formation during plastic deformation of copper single crystals, *Physica Status Solidi (a) 57* (1980) 741-753.
- [63] A.S. Argon, *Physics of Strength and Plasticity* (Ed.: A.S. Argon) (1969), M.I.T. Press, Cambridge, Mass.
- [64] U. Essmann, U. Gösele, H. Mughrabi, A model of extrusions and intrusions in fatigued metals I. Point defect production and the growth of extrusions, *Philosophical Magazine A 44* (1981) 405-426.
- [65] H. Mughrabi, R. Wang, K. Differt, U. Essmann, Fatigue crack initiation by cyclic slip irreversibilities in high cycle fatigue. In *Fatigue Mechanisms*; ASTM STP 811 (1979) 5-45.
- [66] P. Broz, Metal fatigue features, *Acta Polytechnica 46* (2006) 34-41.
- [67] P. Lukas, L. Kunz, Cyclic plasticity and substructure of metals, *Materials Science and Engineering A 322* (2002) 217-227.

- [68] P. Lukas, L. Kunz, Cyclic slip localization and fatigue crack initiation in fcc single crystals, *Materials Science and Engineering A* 314 (2001) 75-80.
- [69] J. Polak, Mechanisms and kinetics of the early fatigue damage in crystalline materials, *Materials Science and Engineering A* 468-470 (2007) 33-39.
- [70] J.M. Finney, C. Laird, Strain localization in cyclic deformation of copper single crystals, *Philosophical Magazine* 31 (1975) 339-366.
- [71] C.D. Liu, M.N. Bassim, Relationship between Stress and Dislocation Structure of fatigued polycrystalline copper, *Phys. stat. sol. (a)* 149 (1995) 323-330.
- [72] S. Brinckmann, On the role of dislocation in fatigue crack initiation, Ph.D. thesis (2005), RIJKS Universiteit Groningen, The Netherlands.
- [73] H.-J. Christ, H. Mughrabi, Microstructure and fatigue. *Low Cycle Fatigue and Elasto-plastic Behaviour of Materials-3* (Ed.: K.-T. Rie), Elsevier Applied Science.
- [74] W.A. Woods, Formation of fatigue cracks, *Philosophical Magazine* 3 (1958) 692-699.
- [75] S. Frechard, F. Martin, C. Clement, J. Cousty, AFM and EBSD combined studies of plastic deformation in a duplex stainless steel, *Materials Science and Engineering A* 418 (2006) 312-319.
- [76] A. Hunsche, P. Neumann, Quantitative measurement of persistent slip band profiles and crack initiation, *Acta Metallurgica* 34 (1986) 207-217.
- [77] B.-T. Ma, C. Laird, Overview of fatigue behaviour in copper single crystals-I. Surface morphology and stage I crack initiation sites for tests at constant strain amplitude. *Acta Metallurgica* 37 (1989) 325-336.
- [78] B.-T. Ma, C. Laird, Overview of fatigue behaviour in copper single crystals-II. Population, size, distribution and growth kinetics of stage I crack for tests at constant strain amplitude, *Acta Metallurgica* 37 (1989) 337-348.
- [79] T. Sumigawa, T. Kitamura, Nucleation of slip bands near twin boundary in high-cycle fatigue, *JSME International Journal* 47 (2004) 98-105.
- [80] J.C. Figueroa, C. Laird, Crack initiation mechanisms in copper polycrystals cycled under constant strain amplitudes and in step tests, *Material Science and Engineering* 60 (1983) 45-58.
- [81] W.H. Kim, C. Laird, Crack nucleation and stage I propagation in high strain fatigue-II. Mechanism, *Acta Metallurgica* 26 (1978) 789-799.

- [82] R.N.F. Mott, A theory of the origin of fatigue cracks, *Acta Metallurgica* 6 (1958) 195–197.
- [83] J.G. Antonopoulos, L.M. Brown, A.T. Winter, Vacancy dipoles in fatigued copper, *Philosophical Magazine* 34 (1976) 549–563.
- [84] C. Laird, The influence of metallurgical structure on the mechanisms of fatigue crack propagation. In *Fatigue Crack Propagation*, ASTM STP 415 (1967) 131-168.
- [85] F. Ellyn, *Fatigue damage, crack growth and life prediction*. 1st edition (1997) Chapman and Hall.
- [86] R. Hales, S.R. Holdsworth, M.P. O'Donnell, I.J. Perrin, R.P. Skelton, A code of practice for the determination of cyclic stress-strain data, *Materials at High Temperatures* 19 (2002) 165-185.
- [87] M. Pohl, A. Ibach, K.-H. Lange, Microstructure and Properties of Super-Duplex Stainless Steels, *Pract. Met.* 28 (1991) 333–349.
- [88] Assessment and management of ageing of major nuclear power plant components important to safety; PWR vessel internals. Technical Report of International Atomic Energy Agency, IAEA-TECDOC, 1119 (July 2003).
- [89] Johnson AB Jr, Sundaram SK, Garner FA. Program plan for acquiring and examining naturally aged materials and components from nuclear reactors. Pacific Northwest National Laboratory, Richland, WA, PNNL-13930 (Dec 2001).
- [90] G. Reidrich, F. Loib, Embrittlement of high chromium steels within temperature range of 570-1100°F, *Arch. Eisenhüttenwes* 15 (1941) 175-182.
- [91] R.M. Fisher, E.J. Dulis, K.G. Carrol, Identification of the Precipitates Accompanying 885°F Embrittlement in Chromium Steels, *Transaction AIME, Journal of Metals* 197 (1953) 690-695.
- [92] R.O. Williams, H.W. Paxton, The nature of ageing of binary iron-chromium alloys around 500°C, *J. Iron Steel Inst.* 185 (1957) 358-374.
- [93] M.J. Blackburn, J. Nutting, Metallography of an iron-21% chromium alloy subjected to. 475°C embrittlement, *J. Iron Steel Inst.* 202 (1964) 610-613.
- [94] E.Z. Vintaikin, A.A. Loshmanov, Nature of the 475° brittleness in iron-chromium alloys, *Phys. Met. Metallography* 22 (1966) 473-476.
- [95] J.W. Cahn, On spinodal decomposition, *Acta metall* 9 (1961) 795-801.
- [96] J.E. Hilliard, Spinodal Decomposition, published in *Phase Transformations*, (Ed.: H. I. Aaronson) (1970), Am. Soc. Metals, Metals Park, Ohio.

- [97] D.E. Nelson, W.A. Baeslack III, J.C. Lippold, Characterization of the weld structure in a duplex stainless steel using colour metallography, *Materials Characterization* 39 (1997) 467-477.
- [98] R.K. Ray, J.J. Jonas, R.E. Hook, Cold rolling and annealing textures in low carbon and extra low carbon steels. *Int. Mater. Reviews* 39 (1994) 129-172.
- [99] J.M. Cowley, R.J. Murray, Diffuse scattering in electron diffraction patterns. II. Short-range order scattering, *Acta Cryst. A* 24 (1968) 329-336.
- [100] J. Johansson, M. Odén, Load sharing between austenite and ferrite in a duplex stainless steel during cyclic loading, *Metallurgical and Materials Transactions A* 31 (2000) 1557-1570.
- [101] F.J. Ager, S. Elmrabet, A. Paúl, Á. Cea-Naharro, M.D. Ynsa, M.A. Respaldiza, J.A. Odriozola, Determination of nitrogen in metallic phases using the $^{14}\text{N}(d, p\gamma)^{15}\text{N}$ nuclear reaction, *Nuclear Instruments and Methods in Physics Research Section B: Beam Interactions with Materials and Atoms* 188 (2002) 96-101.
- [102] Robert N. Gunn. *Duplex Stainless Steels: Microstructure, Properties and Applications* (1997), Woodhead publishing.
- [103] W. Zielinski, W. Swiatnicki, M. Bartsch, U. Messerschmidt, Non-uniform distribution of plastic strain in duplex steel during TEM in situ deformation, *Material Chemistry and Physics* 81 (2003) 476-479.
- [104] S. Bugat, J. Besson, A.-F. Gourgues, F. N'Guyen, A. Pineau, Microstructure and damage initiation in duplex stainless steels, *Materials Science and Engineering A* 317 (2001) 32-36.
- [105] O.A. Hilders, M. Ramos, N.D. Peña, L. Sáenz, Effect of 475°C embrittlement on fractal behavior and tensile properties of a duplex stainless steel, *Journal of Materials Engineering and Performance* 8 (1999) 87-90.
- [106] A. Gironès, L. Llanes, M. Anglada, A. Mateo, Dynamic strain ageing effects on superduplex stainless steels at intermediate temperatures, *Materials Science and Engineering A* 367 (2004) 322-328.
- [107] M.K. Miller, K.F. Russell, Comparison of the rate of decomposition in Fe-45%Cr, Fe-45%Cr-5%Ni and duplex stainless steels, *Applied Surface Science* 94 (1996) 398-402.
- [108] T.J. Marrow, N. Bury, The brittle fracture of 475°C embrittled cast duplex stainless steel, *Fatigue and Fracture of Engineering Materials and Structures* 20 (1997) 565–571.

- [109] L. Devillers-Guerville, J. Besson, A. Pineau, Notch fracture toughness of a cast duplex stainless steel: Modelling of experimental scatter and size effect. *Nuclear Engineering and Design* 168 (1997) 211-225.
- [110] S.G. Druce, G. Gage, E. Popkiss, Effects of notch geometry on the impact fracture behaviour of a cast duplex stainless steel, *International Journal of Pressure Vessels and Piping* 33 (1988) 59-81.
- [111] L. Llanes, A. Mateo, L. Iturgoyen, M. Anglada, Aging effects on the cyclic deformation mechanisms of a duplex stainless steel, *Acta Mater* 44 (1996), 3967-3978.
- [112] A. Mateo, A. Gironès, J. Keichel, L. Llanes, N. Akdut, M. Anglada, Cyclic deformation behaviour of superduplex stainless steels, *Materials Science and Engineering A* 314 (2001) 176-185.
- [113] J. Stolarz, Influence of microstructure on low cycle fatigue in some single phase and biphasic stainless steels, *Proceedings of the fifth international conference on low cycle fatigue, LCF 5, Berlin, Germany (2003)* (Ed.: P.D. Portella, H. Sehitoglu, K. Hatanaka) 3-14.
- [114] I. Karaman, H. Sehitoglu, Y.I. Chumlyakov, H.J. Maier, The deformation of low-stacking-fault-energy austenitic steels, *JOM* 54 (2002), 31-37.
- [115] Z. Zhang, D. Delagnes, G. Bernhart, Ageing effect on cyclic plasticity of a tempered martensitic steel, *International Journal of Fatigue* 29 (2007) 336-346.
- [116] D. Delagnes, P. Lamesle, M.H. Mathon, N. Mebarki, C. Levaillant, Influence of silicon content on the precipitation of secondary carbides and fatigue properties of a 5% Cr tempered martensitic tool steel, *Material Science Engineering A* 394 (2005) 435-444.
- [117] K.-H. Park, J.C. Lasalle, L.H. Schwartz, The low cycle fatigue behaviour of spinodally decomposed Fe-26Cr-1Mo alloys. *Acta Metallurgica* 33 (1985) 205-211.
- [118] H.-R. Sinning, High cycle fatigue of spinodally decomposed alloys. *Acta metall* 30 (1982) 1019-1026.
- [119] R.K. Ham, J.S. Kirkaldy, J.T. Plewes, The fatigue of Cu-Ni-Fe Alloys, *Acta Metall* 15 (1967) 861-869.
- [120] M. Anglada, J. Rodríguez, A. Isalgué, Influence of the plastic strain amplitude on the stability of the spinodal microstructure in the cyclic deformation of a Fe-28Cr-2Mo-4Ni-Ni-Nb alloy, *Scripta Metallurgica* 23 (1989) 1633-1638.
- [121] J. Stolarz, J. Foct, Specific features of two phase alloys response to cyclic deformation, *Materials Science and Engineering A* 319-321 (2001) 501-505.

- [122] M.K. Miller, P.A. Beaven, R.J. Lewis, G.D.W. Smith, Atom probe microanalytical studies of some commercially important steels, *Surface Science* 70 (1978) 470-484.
- [123] J.E. Brown, G.D.W. Smith, Atom probe studies of spinodal processes in duplex stainless steels and single- and dual-phase Fe-Cr-Ni alloys, *Surface Science* 246 (1991) 285-291.
- [124] A. Mateo, L. Llanes, M. Anglada, A. Redjaimia, G. Metauer, Characterization of the intermetallic G-phase in an AISI 329 duplex stainless steel, *Journal of Materials Science* 32 (1997) 4533-4540.
- [125] A. Gironès, P. Villechaise, A. Mateo, M. Anglada, J. Mendez, EBSD studies on the influence of texture on the surface damage mechanisms developed in cyclically loaded aged duplex stainless steels, *Material Science and Engineering A* 387-389 (2004) 516-521.
- [126] T. Bliznuk, M. Mola, E. Polshin, M. Pohl, V. Gavriljuk, Effect of nitrogen on short-range atomic order in the ferritic phase of a duplex steel, *Materials Science and Engineering A* 405 (2005) 11-17.
- [127] I. Alvarez-Armas, M.C. Marinelli, S. Herenu, S. Degallaix, A.F. Armas, On the cyclic softening behaviour of SAF 2507 duplex stainless steel, *Acta materialia* 54 (2006) 5041-5049.
- [128] C.S. Goh, T.H. Yip, Fatigue deformation induced response in a superduplex stainless steel, *Metallurgical and Materials Transactions A* 33A (2002) 3433-3442.
- [129] T.J. Marrow, J.E. King, Fatigue crack propagation mechanisms in a thermally aged duplex stainless steel, *Materials Science and Engineering A* 183 (1994) 91-101.
- [130] J. Kwon, S. Woo, Y. Lee, J. Park, Y. Park, Effects of thermal aging on the low cycle fatigue behavior of austenitic–ferritic duplex cast stainless steel, *Nuclear Engineering and Design* 206 (2001) 35-44
- [131] T. Magnin, J.M. Lardon, Cyclic deformation mechanisms of a two-phase stainless steel in various environmental conditions, *Materials Science and Engineering* 104 (1988) 21-28.
- [132] A. Taisne, B. Decamps, L. Priester, Role of interfaces in duplex stainless steel deformation micromechanisms, *Composite Interfaces* 13 (2006) 89-102.
- [133] U. Krupp, O. Düber, H.-J. Christ, B. Künkler, P. Köster, C.-P. Fritzen, Propagation mechanisms of microstructurally short cracks—Factors governing the transition from short- to long-crack behavior, *Materials Science and Engineering A* 462 (2007) 174-177.

- [134] O. Düber, B. Künkler, U. Krupp, H.-J. Christ, C.-P. Fritzen, Experimental Characterization and two-dimensional simulation of short-crack propagation in an austenitic–ferritic duplex steel, *International Journal of Fatigue* 28 (2006) 983-992.
- [135] R. Lillbacka, G. Chai, M. Ekh, P. Liu, E. Johnson, K. Runesson, Cyclic stress–strain behavior and load sharing in duplex stainless steels: Aspects of modeling and experiments, *Acta Materialia* 55 (2007) 5359-5368.